

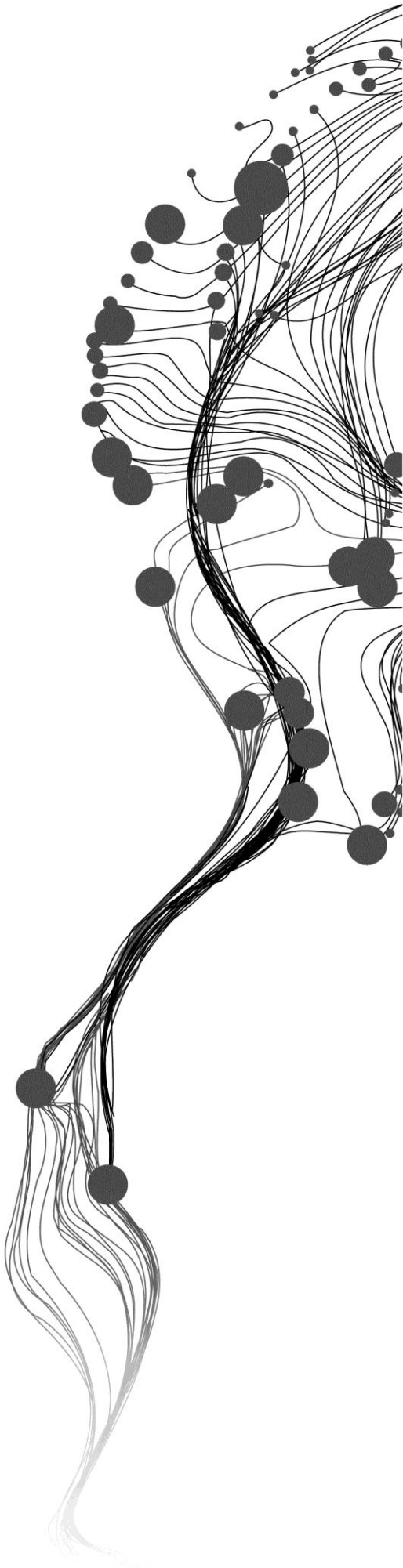
# **Integration of Spatial and Spectral data of very high resolution imagery for building footprint detection using Super Resolution Mapping**

NANTHAMUNI ARACHCHGE WIJERATNA  
February, 2011

SUPERVISORS:

Dr.Ir W. Bijker

Dr. V. A. Tolpekin



# **Integration of Spatial and Spectral data of very high resolution imagery for building footprint detection using Super Resolution Mapping**

**NANTHAMUNI ARACHCHIGE WIJERATNA**  
Enschede, The Netherlands, March, 2011

This thesis submitted to the Faculty of Geo-Information Science and Earth Observation of the University of Twente in partial fulfilment of the requirements for the degree of Master of Science in Geo-information Science and Earth Observation.  
Specialization: Geoinformatics

**SUPERVISORS:**

Dr. Ir. W. Bijker  
Dr. V. A. Tolpekin

**THESIS ASSESSMENT BOARD:**

Prof. Dr. Ir. A. Stein (Chairman)  
Dr. Ir. L.J. Spreeuwens (External Examiner)

#### Disclaimer

This document describes work undertaken as part of a programme of study at the Faculty of Geo-Information Science and Earth Observation of the University of Twente. All views and opinions expressed therein remain the sole responsibility of the author, and do not necessarily represent those of the Faculty.

## ABSTRACT

Building footprint detection from VHR remote sensing images is an important application to supply fundamental data for GIS application and topographical mapping. Automatic detection of shape and size of the building is a challenging task due to the spectral limitation of the VHR MS images and the spatial limitation of the VHR panchromatic image. The integration of spectral and spatial data of VHR MS and panchromatic images is a solution for above limitation. The integration of those data can be done using the image fusion techniques and the MRF based SRM techniques. As the image fusion affects the original reflectance data or the DN value of the image, MRF based SRM is better to preserve the original reflectance value of the images in data integration. Also the MRF based SRM is sensitive to the shape and size of the objects. Therefore this study is carried out to detect the building footprint with the integration of spectral and spatial data of VHR images using MRF based SRM. The study area for the research is Lampuuk village in Indonesia and images are a 4m spatial resolution MS image with four spectral bands and 1m spatial resolution panchromatic images of KOMPSAT -2.

This method is based on the MRF based SRM technique following soft classification. Soft classification is applied to the VHR MS image to get the land cover proportion images. Then the initial SRM is generated using the proportion images produced from the soft classification and the scale factor 4. The initial SRM is optimized with the posterior probability of the pixel. According to the MRF and Gibbs equivalence the energy is optimized instead of optimization of probability. The maximization of posterior probability is equivalent to the minimization of posterior energy. The posterior energy is modelled using contextual information and the likelihood energy is modelled using the class statistics from MS and panchromatic images. Then the optimization was done with Maximum A Posterior (MAP) solution which is reached with simulated annealing (SA) algorithm. The optimization with SA is compared with the Iterated Conditional Modes (ICM). Finally the validation of the method is done in pixel based and object based analysis. This method was compared with the conventional MLC.

The pixel based accuracy assessment of the SRM optimized with SA shows the user accuracy 68%, producer accuracy 65%, overall accuracy 87% and the kappa value 0.584. Those values of the SRM optimized with ICM are 69%, 64%, 87% and 0.581 respectively. The same measures from MLC with fused image are 50.86 %, 68.69%, 62.11% and 0.483 respectively. The object area based accuracy assessment of SRM with SA showed the over identification 0.436, under identification 0.23 and total error 0.493. Those from SA with ICM are 0.419, 0.24 and 0.483 respectively. The same measures from MLC with fused image are 0.550, 0.252 and 0.605 respectively. Then the building object wise validation also done and it showed that the MRF based SRM method detected 276 building footprints out of 292 building footprints in the reference image. According to that MRF based SRM has detected 95% of the buildings in the study area.

According to two types of accuracy measures it can be concluded that both the SA and ICM algorithms produced almost the same accurate SR maps and detected the same percentage of buildings in the study area. Secondly it can be concluded that MRF based SRM provides more accurate results than image fusion for the integration of spectra and spatial data of VHR images in building detection. Third conclusion is that the MS image with panchromatic image provides more accurate SR map for the building footprint detection. The overall conclusion of this study is that MRF based SRM is more accurate than the conventional MLC for the building footprint detection from VHR satellite images.

***Key words:-*** Super Resolution Mapping (SRM), Markov Random Field (MRF), Soft classification, Linear Spectral Unmixing, Maximum Likelihood Classification, Maximum A Posterior solution (MAP), Simulated Annealing (SA) and Iterative Conditional Modes (ICM).

## ACKNOWLEDGEMENTS

I would like to pay my deepest respect and appreciation to all those who contribute in various ways in my studies at ITC, particularly the NFP for providing me the opportunity to study in ITC on a scholarship.

It is my great pleasure to express my sincere gratitude to my supervisors, Dr. Wietske Bijker and Dr. Valentyn Tolpekin, who have guided me in this study providing invaluable constructive criticisms, suggestions and contributions for the success of the research.

I would like also to thank Mr. Juan Pablo who has supported me to solve some technical problems during this research period.

My sincere gratitude goes for all the staff in ITC, for sharing their experience and knowledge throughout my studies at ITC.

Thanks also go to all my GFM colleagues, especially Jhon, Langat, Naum Kim and Masganow and Sri Lankan friends who have been with me from the beginning of ITC study at all the time sharing the pleasure and hardness of the ITC life.

I would like to express my sincere thanks to top management level officers in survey department of Sri Lanka such as Surveyor General Mr. S.M.W. Fernando, Additional Surveyor General Mr. K. Thawalingam and Senior Superintendent of Surveys Mr. K.D. Parakum Shantha for offering me the opportunity to study at ITC.

I would like to express my deepest gratitude to my parents for their encouragement in my education at every aspect. Finally, I am obliged to my beloved wife, Chandani, my son, Saroj, and daughter who have supported and the dedication of their valuable time for my higher education at abroad.

# TABLE OF CONTENTS

---

1.	Introduction.....	1
1.1.	Motivation and problem statement.....	1
1.2.	Research identification .....	3
1.3.	Research objectives .....	3
1.4.	Research questions .....	3
1.5.	Research approach .....	4
1.6.	Structure of the thesis .....	4
2.	Review of building footprint detection techniques.....	5
2.1.	Introduction .....	5
2.2.	Building footprint detection using image classification techniques.....	5
2.3.	Building footprint detection using object oriented Analysis .....	6
2.4.	Building footprint detection using Artificial Neural Network .....	7
2.5.	Building footprint detection from other techniques .....	7
2.6.	Data integration for feature extraction .....	8
2.7.	Summary .....	10
3.	Super resolution mapping techniques .....	11
3.1.	Effect of mixed pixel in object detection from Remote Sensing images .....	11
3.2.	Sub pixel classification .....	11
3.3.	Supper Resolution Mapping .....	14
3.4.	Data integration with MRF based SRM .....	17
3.5.	Energy optimization.....	18
3.6.	Summary .....	19
4.	Study area and data preparation .....	21
4.1.	Study area .....	21
4.2.	Data for the study.....	21
4.3.	Image co-registration .....	23
4.4.	Sub set image preparation .....	23
4.5.	Class definition.....	25
4.6.	Image fusion.....	26
4.7.	Reference map preparationfor tuning and study area for the SRM .....	27
5.	Proposed building detection approach.....	29
5.1.	Soft classification .....	29
5.2.	Initial SRM generation .....	30
5.3.	Energy modelling.....	30
5.4.	Optimization of SRM with Simulated Annealing .....	30
5.5.	Energy optimization with Iterated Conditional Modes .....	30
5.6.	Building detection.....	31
5.7.	Building detection with MLC.....	31
5.8.	Validation and comparison .....	31
5.9.	Summary .....	32
6.	Results.....	33
6.1.	Parameter estimation of the Super Resolution Mapping .....	33
6.2.	Simulated Annealing parameters estimation.....	33
6.3.	Determination of temperature updating rate .....	35
6.4.	Determination of smoothing parameters ( $\lambda$ and $\lambda_p$ ).....	36
6.5.	Estimation of window size .....	37
6.6.	Effect of the SA and annealing parameters on the colour of the roof and the size of the buildings .....	38
6.7.	Optimized SRM .....	39

6.8.	Building footprint detection with MLC.....	40
6.9.	Validation and comparision.....	40
7.	Discussion.....	45
7.1.	Strength of the proposed building detection approach.....	45
7.2.	Weakness of the approach.....	45
7.3.	Opportunities for improvement.....	46
7.4.	Threats to the proposed building detection approach.....	46
8.	Conclusions and Recommendations.....	47
8.1.	Conclusions.....	47
8.2.	Recommendations.....	48

## LIST OF FIGURES

---

Figure 3.1: Output of hard classification and soft classification: (a) hard classification output one thematic map, (b) thematic maps per land cover class from soft classification (Source Lucas et al., 2002). .....	12
Figure 3.2: Linear mixing (a) and nonlinear mixing (b) at the Earth surface (Source: Keshava, 2003) .....	13
Figure 3.3: Overview Super Resolution Mapping process and harden version of soft classification image (Source: URL-2) .....	14
Figure 3.4: Fifth order neighbourhood system .....	16
Figure 3.5: Cliques for four neighbourhood (a); eight neighbourhood (b) .....	16
Figure 3.6: Schematic diagram of SA optimization .....	19
Figure 4.1: Study area – Lampuuk in Aceh, Indonesia (Source: URL-3 and Google Earth on 07/02/2011) .....	22
Figure 4.2: Sub set images of the study area (MS image at right and panchromatic image at left) .....	24
Figure 4.3: MS (right) and panchromatic (left) tuning images .....	24
Figure 4.4: (a) fused images from wavelet resolution merge with PCA, (b) fused image from resolution merge with PCA, (c) fused image from modified HIS resolution merge, (d) fused image from Ehlers fusion and (e) fused image with High Pass Filter (HPF) .....	27
Figure 4.5: (a) Tuning Reference image, (b) Reference image for study area .....	27
Figure 5.1: The proposed building footprint detection approach .....	29
Figure 6.1: Mean kappa of SRM versus initial temperature ( $T_0$ ) with standard deviation in error bars .....	34
Figure 6.2: Mean energy versus initial temperature ( $T_0$ ) with standard deviation in error bars .....	34
Figure 6.3: Mean kappa versus Temperature updating rate ( $T_{upd}$ ) with standard deviation in error bars ....	35
Figure 6.4: The mean kappa of the optimized SRM versus panchromatic smoothing parameters ( $\lambda_p$ ) for different smoothing parameters ( $\lambda$ ) .....	36
Figure 6.5: The standard deviation of the optimized SRM versus panchromatic smoothing parameters ( $\lambda_p$ ) for different smoothing parameters ( $\lambda$ ) .....	36
Figure 6.6: Mean kappa versus window size (w.s) .....	37
Figure 6.7: Building footprint map from MRF based SRM optimized with SA (a) and ICM (b) .....	39
Figure 6.8: Building footprint map from (a) MLC with fused image (b) MLC with MS image .....	40
Figure 6.9: Shape and size of detected buildings from SRM (left) and MLC with fused image (right) .....	43
Figure 6.10: Overlay of reference map on SRM building footprint map .....	43
Figure 6.11: Overlay of reference map on building footprint map from MLC .....	43

## LIST OF TABLES

---

Table 4.1: Spectral and spatial resolution of the selected images (Source: Leea et al., 2008).....	21
Table 4.2: Coordinates of the area covered by the selected images .....	23
Table 4.3: coordinates and the dimensions of the study area.....	24
Table 4.4: coordinates and the dimensions of the tuning image.....	24
Table 4.5: Transformed divergence of the chosen land cover classes in MS image .....	25
Table 4.6: Transform divergence of the chosen land cover classes in panchromatic image.....	25
Table 6.1: Statistics of kappa values with initial temperature ( $T_0$ ) for window size 3 .....	33
Table 6.2: Statistics of energy values versus initial temperature ( $T_0$ ).....	34
Table 6.3: Statistics of kappa values versus temperature updating rate .....	35
Table 6.4: Statistics of kappa values for different window sizes .....	37
Table 6.5: Parameters of the energy model and SA .....	38
Table 6.6: Number of building detected according to the roof colour and size .....	38
Table 6.7: The confusion matrix of building footprint map from SRM optimized with SA .....	40
Table 6.8: The confusion matrix of building footprint map from SRM optimized with ICM .....	41
Table 6.9: The confusion matrix of building footprint map from HPF fused image .....	41
Table 6.10: The confusion matrix of building footprint map from MS image.....	41
Table 6.11: Kappa coefficient of each building footprint map .....	41
Table 6.12: Percentage of building detection in SR maps.....	42
Table 6.13: Results of object based accuracy assessment for each building footprint map .....	42

# 1. INTRODUCTION

## 1.1. Motivation and problem statement

With the development of very high resolution (VHR) images, the detail extraction of objects on the Earth surface becomes a topic of active research in the field of Remote Sensing. One of the interesting studies from VHR images is the building footprint detection. It is a very useful application in the automation of cartographic mapping and updating the existing vector data of a geographical information system (San & Turker, 2005). Among the necessary data for a geographical information system, the building footprint is one of the fundamental data (K. Zhang et al., 2006). According to Zhang et al. (2006) the building footprint information is useful for the estimation of energy demands, life quality, urban population and property taxes. The integration of building footprint data with height of the buildings helps to generate the three dimensional building models for the visualization. An interesting application of building footprint data is the investigation of financial corruption and transparency of building contraction projects launched by the funding organizations after natural disasters like tsunami and earthquake which demolished the buildings (Du et al., 2009). For the various purposes, the government and private organizations in any country needs up to date building information efficiently. For that Remote Sensing has advantages over other data sources. The recent satellite imaging sensors such as IKONOS, GeosEye-1 and Quick Bird provide a valuable data source for the building footprints detection. In the past, the building extraction from images was done manually. It is time consuming, labour intensive, costly and it is difficult to reproduce. The automatic building detection reduces these limitations.

The building detection from Remote Sensing images depends on the spatial resolution. According to the spatial resolution, there are four types of images. Those are low resolution (more than 1km), medium resolution (between 100m and 1km), high resolution (between 10m and 100m) and very high resolution (less than 10m) images (URL-1). It is difficult to identify the buildings from low and medium resolution images due to the poor spatial resolution. In the case of high and very high resolution images, very high resolution images are better than high resolution images as it enables to detect the smaller and irregular building footprints. The building footprint detection can also be done using aerial images. But the aerial images have some limitations due to less spatial coverage and availability compared to the VHR space images. The acquisition of aerial images is time consuming. VHR images may also not be available everywhere due to the cloud problem and limited recording time per orbit and if it is not in the archive already then they do have acquisition time as well, depending on orbit, weather and operating station. However the acquisition time for the VHR images is usually smaller than the airborne images. At present VHR optical sensors provide the images with spatial resolution in the aerial image resolution domain. Therefore the use of VHR space images has more advantages.

Several methods have been developed for building detection using VHR space images with different techniques. The maximum Likelihood Classifier (MLC) with normalized digital surface model (nDSM) can be used to detect the buildings (San and Turker, 2005). This method works only for regularly developed urban areas. Another building detection technique is the integration of structural, contextual and spectral information with differential morphological profile (DMP) but this method has shown low accuracy in building extraction due to the significant misclassification (Jin & Davis, 2005). The building detection has been done using the classification techniques based on segmentation and shape which was based on Hough transformation (Scott et al., 2003) but the result was not satisfactory due to the misclassification of roofs and roads. One of the latest building extraction approaches is based on the object oriented image

analysis (Du et al., 2009; Durieux et al., 2008; Rutzinger et al., 2008). However the identification of connected buildings is not satisfactory due to the spatial and spectral limitation of VHR multispectral (MS) and panchromatic images. The VHR images have two different properties namely high spatial resolution of the panchromatic image and relatively high spectral resolution from the MS image. The combination of these two properties facilitates a better interpretation of the objects from remote sensing images. Therefore those properties can be integrated to overcome the spatial and spectral limitation of VHR MS and panchromatic images in building identification and it helps to improve the accuracy of the building detection.

The MLC which assigns a class label per pixel has been used for the MS image classification in the building detection. MLC does not classify individual land cover classes present in the mixed pixel that has been resulted due to the reflectance from different objects within the instantaneous field of view (IFOV) of the sensor and also from the surrounding objects of IFOV on the Earth surface (Cracknell, 1998). Therefore these mixed pixels pose a problem in conventional land cover classification as the conventional classification technique assigns one class label to the pixel. In the building detection process mixed pixels pose a problem in MS image classification with MLC and also it affects the building detection accuracy. The integration of the spatial and spectral resolutions of VHR MS and panchromatic images is a solution for mixed pixel problem. The integration of spatial and the spectral data can be performed using an image fusion or using the super resolution mapping (SRM) method based on Markov Random Field (MRF) proposed by Tolpekin et al., (2010).

The image fusion technique can be used for the integration of spatial and spectral data of VHR MS and panchromatic images. The image fusion combines the observed spatial and spectral data of images to generate the fused image with more detail information than the input sources (Jixian Zhang, 2010). The fused image is used for the classification in the building detection process from VHR images. Therefore the classification is not on the original spectral data of the MS image. The SRM is a land cover classification technique that generates a finer resolution thematic map from a coarse resolution input image. This is a step beyond the sub pixel classification. The sub pixel classification resolves the mixed pixels in the image to proportions of land cover classes. Then SRM arranges the location of the individual land cover class proportions in an optimized way to form the land cover classes in the image. The location of the land cover proportion in mixed pixels is carried out with the help of posterior probability which is the product of prior and likelihood probabilities. The prior probability is modelled using MRF with the spatial context of the Remote Sensing images and likelihood probability is calculated using both MS image and panchromatic image. Therefore SRM based on MRF offers a solution for locating the proportions of land cover classes in the mixed pixels in coarse resolution image and it will solve the spatial limitation of multispectral image for the detection of building footprint. In the SRM, the integration of spatial and spectral data is carried out after the soft classification technique. The soft classification is over the original spectral data. Then integration of spectral and spatial data based on MRF and SRM does not affect the land cover classification. Therefore SRM is better than the image fusion for spectral and spatial data integration in building footprint detection.

SRM locates the sub pixels within the coarse pixels in an optimized way to maintain the spatial context between the sub pixels. The spatial context is the correlation between spatially adjacent sub pixels in the neighbourhood (Solberg et al., 1996). The location of sub pixels is done by maximizing the posterior probability of the sub pixel in pixel labelling. The posterior probability is the product of prior and likelihood probability. The prior probability is modelled from the contextual information of the pixels in the image using MRF. There are different sizes of objects such as trees, buildings in a Remote Sensing image. Larger object size has more context than the smaller object as larger objects consist of more pixels than the smaller objects. The accuracy of the SRM is related to the size of the objects. Larger objects results into more accurate SRM as larger objects provide higher prior probability (Kassaye, 2006). The

quality of the SRM also relates to the resolution of the image. The low resolution images provide poor context to the pixels of an object in neighbourhood as the objects represents with less number of pixels in low resolution images. High resolution images provide the richer context for the pixel in neighbourhood to model the prior probability. Therefore higher resolution images results into more accurate SRM. The large objects are heterogeneous and are not reliable for high quality SRM as the spatial context of pixel is different.

The combination of panchromatic image with MS image in SRM has advantages as the panchromatic image provides finer spatial resolution for the pixels to have higher probability to belong to a land cover class. An object in panchromatic image has more observed spatial detail for the likelihood probability calculation while MS image provides more spectral information for the calculation of likelihood probability in pixel labelling. The combination of more spatial detail from panchromatic image and more spectral information from MS image results the pixel to have higher likelihood probability for the correct labelling. This would be useful for the identification of the shape of the individual building in clustered built up area. Therefore the integration of panchromatic and MS images in SRM leads to obtain a more accurate SR map than the SR map only from MS image.

The existing methods for the building footprint detection from VHR images have some limitation due to the limited spatial resolution of VHR MS image and the mixed pixels. It limits the identification of individual buildings. But soft classification followed by SRM based on MRF method (Tolpekin et al., 2010) is a solution for the mixed pixel problem and it integrates the spatial and spectral data of MS and panchromatic images for the calculation of likelihood probability in pixel labelling. Therefore SRM based on MRF will be a solution for those limitations in building detection. These factors motivate the study of building footprint detection using super resolution mapping approach by integrating the spectral and spatial data of very high resolution space borne imagery. Therefore this research will be carried out to develop a method for the building footprint detection using MRF based SRM by integrating the spectral and spatial data of VHR MS and panchromatic images.

## **1.2. Research identification**

According to the above discussion the building footprint detection from VHR space imagery is a very important tool for different applications of geodata. Therefore the building detection techniques still remain as a significant field for research. One of the reasons for less accurate result in building detection is due to the presence of mixed pixel. This mixed pixel can be classified by soft classification as land cover proportion. The location of the land cover proportion within pixel can be arranged by the SRM. The soft classification followed by SRM can be applied to improve the accuracy of building detection from VHR images. Therefore this study will focus on the development of building footprint detection technique using the super resolution mapping by integrating the spectral and spatial resolution of VHR MS and panchromatic images.

## **1.3. Research objectives**

The objective of this study is to develop a method based on MRF and SRM for building footprint detection by integration of VHR MS and panchromatic images.

## **1.4. Research questions**

The study will answer the following research questions in order to attain the research objective.

1. Which energy optimization method is more suitable to obtain the most accurate result from MRF based SRM: Simulated Annealing (SA) or Iterated Conditional Modes (ICM) in building footprint detection?
2. How do the simulated annealing parameters affect the accuracy of MRF based SRM result in building footprint detection?
3. Which accuracy measure is more suitable for the accuracy assessment of building footprint detection from VHR MS and panchromatic images: object based or pixel based accuracy measure?
4. Is SRM based building footprint detection technique with MS and panchromatic image more accurate than the MLC based building footprint detection technique from fused image?

### **1.5. Research approach**

The research approach in this study is based on the integration of spatial and spectral data in panchromatic and multispectral images using MRF and SRM. The building detection is carried out with the optimization of SRM followed by soft classification of the VHR MS image. The soft classification is used to produce the land cover proportion maps for each land cover classes including the building footprints. Then the SRM and MRF are applied for the optimization of spatial dependency in the classified image with the integration of spatial and spectral data in VHR MS and panchromatic images. The validation is done in both pixel based and object based accuracy assessments. Finally the result from the MRF based SRM is compared with the result from MLC classification.

### **1.6. Structure of the thesis**

The thesis contains eight chapters. The first chapter consists of motivation and problem statement, objective, research questions, research approach and the structure of the thesis. The second chapter will be focused on the literature review of the building footprint detection from VHR images. The SRM based on MRF technique will be discussed in the third chapter. The fourth chapter will be described with the study area and data preparation. Fifth chapter will be described the methodology applied for the research. Then the results obtained from this study will be discussed in the sixth chapter and chapter seven is on the discussion of the result. The chapter eight will elaborate on the conclusions drawn from this research and recommendation for further study on the building footprint detection.

## 2. REVIEW OF BUILDING FOOTPRINT DETECTION TECHNIQUES

### 2.1. Introduction

At present the object extraction and the updating of existing GIS data base are more important in various application domains such as town planning, property taxation, designing communication network, and planning and management of services in a country or a region. The traditional mapping methods for the objects on the Earth surface are tedious, time consuming and costly. The availability of the very high resolution satellite images is a solution for limitation of traditional object extraction methods. The recently launched high resolution sensors such as IKONOS, Quick Bird, KOMPSAT, and Geoeye provide the finer resolution images with fine details. Those images facilitate the extraction of the objects like buildings (Durieux et al., 2008), trees crowns (Tolpekin et al., 2010) and roads (Haris et al., 1998; Hay & Castilla, 2008). The high resolution satellite images are rich with finer details that could be extracted for updating of GIS data bases and developing the new GIS. One of the important objects that could be extracted from high resolution images for GIS is the building footprints. The building extraction from satellite images has been done in different approaches and it is still an active research topic in the field of remote sensing. The prevailing building extraction methods from Remote Sensing images are based on different techniques such as image classification, object oriented image Analysis method and Artificial Neural Network method. These methods are described in detail in the following sections.

### 2.2. Building footprint detection using image classification techniques.

Most building detection methods are based on image classification technique. A widely used image classification method for the building detection is maximum likelihood classification though there are different image classification methods such as parallelepiped, minimum distance to mean classification, box classification. The maximum likelihood classification (MLC) is popular for the image classification in various applications as it is statistical and supervised classification technique (San & Turker, 2010). Therefore it is also used for the MS image classification in the building detection approaches. The building footprint extraction is to carry out with MLC classification and separates from other features such as road and vegetation incorporating the other techniques such as normalized Digital Surface Model and Normalized Difference Vegetation Index (San & Turker, 2005). The maximum likelihood classification is a supervised statistical approach for the recognition of patterns in the remotely sensed images. The MLC is based on the assumption that the likelihood probability follows the normal distribution. It considers the class mean vector and the covariance matrix of the land cover classes in the pixel classification process. MLC algorithm calculates the probability of a pixel that belongs to set of user defined classes. Then the pixel is assigned to the class for which the likelihood probability (conditional probability) is highest.

#### 2.2.1. Applications of MLC in building detection and extraction

The MLC has been applied for image classification in the building detection approaches from high resolution satellite images (Elshehaby & Taha, 2009; Hajime et al., 2001; San & Turker, 2005). San and Turker., (2005) developed a method for the building extraction using MLC. First the pan-sharpened MS image was classified with MLC and separation of building from other ground features was done using normalized Digital Surface Model (nDSM) which is the difference between Digital Surface Model (DSM) and the Digital Elevation Model (DEM). After the separation of building from other ground features Normalized Difference Vegetation Index (NDVI) was used to differentiate the building from trees. Then the building was extracted as a vector layer after applying the canny edge detector. Elshehaby and Taha,

(2009) applied the MLC to compare three building extraction methods. They applied the MLC to classify the multispectral image only. Second approach is the classification of MS image with MLC and extraction of building was carried out with the help of height information from LiDAR data. For the third approach they applied the MLC for image classification and improved the result using the knowledge of the elevation data and the spectral information with the knowledge engineer in ERDAS IMAGINE. According to this study the third approach was satisfactory for the building detection from high resolution satellite images. Another application of MLC for the building detection was the identification of damaged building from satellite images after the earthquake of Kobe, Japan in 1995 (Hajime et al., 2001). Hajime et al., (2001) used the image characteristics such as hue, saturation, brightness, edge intensity and intensity variance to separate the damaged and intact buildings from post-earthquake images after the image classification with MLC. The result of this study was satisfied with the actual building damaged area.

### **2.3. Building footprint detection using object oriented Analysis**

The Remote Sensing images consist of set of pixels which represent the objects on the Earth surface. Normally objects are different in shape and the size and they do not exactly fit with the pixels. Therefore the conventional image classification techniques such as MLC have the limitation to preserve the shape of the objects in the classification process and also the pixel based classification produces less accurate results because of the heterogeneous spectral property of the pixels within the objects. As a solution for these limitations in traditional image classification, a new image classification approach referred to as Object Oriented Analysis (OOA) has been developed in recent years. The OOA is an automated image partition methods which segment a Remote Sensing image into meaningful image objects and assesses their characteristics using the spatial, spectral and temporal dimensions to produce an output which is new geographic information suitable for GIS (Hay & Castilla, 2008). The OOA technique uses the idea that homogeneous objects can be derived with the help of the shape, smoothness, compactness and colour. The OOA technique consists of two sub techniques which are image segmentation and the classification.

The image segmentation is the main step of the object based feature extraction method. The image segmentation is the process of dividing an image into non-overlapping objects or regions based on the spectral homogeneity of the pixels in Remote Sensing image. There are two type of segmentation methods widely used in object oriented automatic feature extraction from Remote Sensing images. Those are edge based segmentation and region based segmentation(Haris et al., 1998). The edge based segmentation is done by thresholding of image gray values and applying the differentiation filters to segment the image in to objects. It produces the image of edge and non-edge regions. This segmentation is reliable for the linear feature extraction. The region based segmentation is carried out using region growing algorithms in which the regions are detected either by growing a seed pixel with homogeneous neighbouring pixels or splitting the whole image in to regions and then merging the homogeneous area to form the regions or objects. This type of segmentation is better for the identification of area objects like buildings, water bodies and land use. Then the segmented objects are labelled with a classification algorithm. This classification is not like conventional image classification as it is based on the objects or the regions resulted from the segmentation. The object oriented classification also differs in the use of image properties from the conventional classification. It uses the spectral, textural, contextual, spatial and semantic information while conventional classification uses only the spectral information.

#### **2.3.1. Application of OOA for building footprint detection**

One of the latest approaches for the detection of building from high resolution satellite images is object oriented image analysis. It has been applied for the verification of transparency in housing reconstruction projects in Banda Aceh, Indonesia after the tsunami 2004(Du et al., 2009). Du et al., (2009) applied the segmentation algorithm in eCognition to segment the KOMPSAT-2 image then applied the object oriented classification based on decision tree to detect the building footprint. This study has proven that

the OOA can be applied successfully for the building footprint detection from high resolution multispectral satellite image. Another application of OOA for building identification was the monitoring of the urban sprawl using high resolution Spot 5 images of Reunion Island in the Indian Ocean (Durieux et al., 2008). The bottom-up region growing algorithm was applied for the segmentation of the image in this approach. The separation of building from other objects was done with the help of contextual and scale information. The disadvantage of this method is that it detects only the brightest part of the buildings.

The class guided building extraction approach was introduced with segmentation using the high resolution multi spectral and panchromatic IKONOS images of Camp Lejeune, North Carolina (Scott et al., 2003). In this method the multispectral image was classified using the ECHO classifier to identify the approximate shape and location of the buildings. Then the exact buildings were detected with the segmentation of panchromatic image and the shape of the buildings was generated with the Hough transformation. This approach showed the satisfactory result but misclassification of buildings and road affects the accuracy of the building detection. There are few applications of OOA for the identification of buildings from high resolution images in the literature.

#### **2.4. Building footprint detection using Artificial Neural Network**

Another technique used in building detection from high resolution satellite images is the Artificial Neural Network (ANN). The Artificial Neural Network is mathematical model which is designed to perform a desired function. There are different types of ANN such as back-propagation networks, multilayer Feed-forward networks, local minima and counter-propagation networks. The neural network is capable of pattern recognition and object extraction from the remote sensing images (Hamid & Lari, 2007). The execution of ANN consists of two phases such as learning phase and the application phase. The learning phase is the very important phase in which the ANN is trained with a test data set. After the ANN is properly trained to identify the building footprint from the satellite image it can be used to detect the building footprints from the interested area of satellite image. In this approach training is the crucial step for the detection of buildings.

Several studies have been done for the building detection using Artificial Neural Network. Hamid and Lari, (2007) applied the three layer perception neural network with supervised learning for the building extraction using the very high resolution (1m) IKONOS image of Kashan area in Iran. Around 80% of the buildings in the study area were identified with this method. After a disaster it is very important to assess the number of building damaged within short period. The ANN application for the detection of damaged buildings due to the Bam earthquake was done with combination of co-occurrence matrix using the high resolution Quick Bird image (Ahadzadeh et al., 2008). The texture of the buildings in the QuickBird images was calculated using co-occurrence matrix and the damaged buildings were identified with ANN using the change of texture after the earthquake. The majority of damaged buildings could be identified with this method according to Ahadzadeh et al., (2008).

#### **2.5. Building footprint detection from other techniques**

For the building detection from the high resolution remote sensing images other approaches have been developed using different techniques such as contextual analysis, snake methods and morphological filtering. One of such methods is the automated building detection approach with a combination of Support Vector Machines (SVM) and Hough transform. It was used for the extraction of rectangular and circular shaped buildings from high resolution Remote sensing images of Batikent district in Turkey (San & Turker, 2010). San and Turker, (2010) applied the binary Support Vector Machines (SVM) classification to identify the building patches with normalized Difference Vegetation Index and the normalized Digital

Surface Model. Then the vector building layer was generated using Hough transform after applying the Canny edge detection algorithm on the building patches. The disadvantage of this approach is that it could detect only the rectangular and circular buildings.

Mayunga et al., (2005) have developed a semi-automated building extraction method with active contour models also known as “snakes” and a radial casting algorithm using high resolution Quick Bird images of Dar Es Salaam city, Tanzania and Oromocto Township in New Brunswick. The active contour model is an energy minimization function which uses to identify the building footprints in Remote sensing image. The involvements of the human operator are for the measurements of approximate centre of the building and for the rejection or acceptance of the generated snake contours. The minimization of energy in the neighbourhood for the accepted contours is iteratively carried out with the 3 by 3 search window. The building outline is generated when the outline fits with the snake contour. This method came up with highly reliable results and increased the speed of the building extraction compared to the manual photogrammetric object extraction method and is also applicable for structured and unstructured urban areas. This method has been improved to extract irregular shape buildings also by using the circular casting algorithm instead of a radial casting algorithm(Lau, 2006).

In 2007 an automated building extraction method was developed from a Digital Elevation Model to extract rectangular buildings with a marked point process(Ortner et al., 2007). A marked point process is a random variable which adds the marks to each point. The approach was developed with the combination of a Bayesian model with energy minimization. The method is applicable for the urban areas and the disadvantage is that the method is slow even for small areas. A modified machine vision approach has been applied for the building detection with a digital elevation model generated using Synthetic Aperture Radar (SAR) interferometric data(Gamba et al., 2000). This method is recommended for large commercial buildings but it is not satisfactory for small building footprint detection.

Kim and Muller, (1994) proposed an automated building detection method using graph constructed from lines and line relation with high resolution images. The depth first graph traversal algorithm was applied to generate the buildings by finding the closed loops in the graph. This method works successfully with the complicated buildings in aerial images and the large buildings in high resolution satellite images. The wavelet analysis which can detect the intensity variation at edges and corners of objects in an image with Canny edge detection has been used for the building detection with high resolution panchromatic IKONOS image(Selvarajan & Tat, 2001). The advantage of this method is that it is very fast and simple.

## **2.6. Data integration for feature extraction**

The acquisition of Remote sensing images is carried out in different spatial and spectral resolution with different sensors such as IKONOS, QuickBird, KOMPSAT and Geoeye. These images have to be combined for various applications such as feature extraction, identification, pattern recognition, classification, and change detection. The combination of different type of images can be done with data integration techniques which are also known as image fusion or data merging (Thurmond et al., 2006). The data integration is the process of combining two or more different images or data type such as remote sensing data and vector data to produce a new spatial information using a certain algorithm (Genderen & Pohl, 1994). According to Genderen & Pohl, (1998) the image fusion can be categorized in to three different levels such as pixel or data level, feature level and decision level. The pixel level image fusion is the integration of unprocessed data of different sources into single image that is more informative than the input images. The combination of different features like lines, corners and edges extracted from two or more images to form a one or more feature maps is the feature level image fusion. The decision level data fusion is the merging of the results obtained from several algorithms to produce a fused decision map (Jixian Zhang, 2010). According to Jixian Zhang, (2010) the pixel level image fusion techniques are

applied to the panchromatic and multispectral optical images while the feature level and decision level fusion techniques are applicable to the data from different sources such as LiDAR, field data, geographical information, optical data and synthetic Aperture Radar (SAR). This study is based on the pixel level data integration to extract the building features.

### 2.6.1. Pixel level image fusion

The pixel level data integration methods are very important tools for the application of optical images as they provide the capability to improve the spatial resolution, structural and textural detail and to preserve the spectral property of the coarser resolution multispectral images by merging with a finer resolution panchromatic images. The pixel level image integration techniques are categorized into three as follows (Jixian Zhang, 2010; Yang et al., 2010).

- Component substitution image fusion techniques
- Modulation based image fusion techniques
- Multi resolution analysis based image fusion techniques

The component substitution image fusion is executed in three steps which are forward transformation, replacement of the component similar to panchromatic band with high resolution band and generation of fused image using inverse transformation (Yang et al., 2010). The widely applied component substitution fusion algorithms are Intensity Hue Saturation (IHS), the Principle Component Analysis (PCA) and Gram–Schmidt (GS) spectral sharpening (Yang et al., 2010). In the modulation based image fusion the spatial details are modulated to the MS image with the multiplication of MS image by ratio between the panchromatic image and the lower resolution version of the panchromatic image. The currently used modulation based fusion algorithms are smoothing filter based intensity modulation, synthetic variable ratio fusion, high pass spatial filter, and Brovey transform image fusion. The multi resolution analysis based image fusion techniques decomposes the input images to different levels and converts the details in MS image to finer resolution. This process is carried out in three steps such as wavelet multi resolution decomposition, replacement of approximate coefficients of panchromatic band with MS band and the inverse multi resolution transform. For the object detection from high resolution images the modulation based and multi resolution analysis fusion techniques are reliable as these techniques preserve the spectral properties of the MS image (Yang et al., 2010). From these images fusion techniques the following objectives can be achieved in the object detection and extraction processes from the satellite images.

- To obtain the sharpen images from finer resolution panchromatic image and coarser resolution multispectral image
- To improve the accuracy of the geometric correction
- To obtain the stereoscopic vision for photogrammetry
- To enhance the specific features that are not clear in raw data
- To obtain the complement data set for the image classification
- To identify the changes from multi-temporal images
- To substitute the missing data in an image due to clouds and shadows
- To replace the incomplete data of an image

### 2.6.2. MRF and SRM based data integration

The data integration can also be done using the Markov Random Field based super resolution mapping technique (Tolpekin et al., 2010). The remote sensing images are modelled with the Markov random field in the image classification to produce high accurate thematic map. The data is integrated with the help of MRF models of MS and panchromatic images. This data integration method helps to enhance the boundaries of the objects which consist of the mixed pixels. The advantage of this data integration technique over other fusion techniques is that it helps to solve the mixed pixel problem in image

classification and also it does not affect the original reflectance value as general image fusion methods. The detail description about this method will be discussed in Chapter 3.

### **2.6.3. Application of data integration in building detection**

Building detection was carried out using an unsupervised classification followed by texture filtering with integration of high resolution TM and SPOT images by Zhang, (1999). In this approach the ISODATA clustering method was used for the classification of pan-sharpened multispectral image of TM and SPOT images of the city of Shanghai, China. Then the filter based on direction dependence of co-occurrence matrix was applied to improve the accuracy of the building identification. The result of the proposed method is better than the conventional multispectral classification method. The merging of spectral properties and height information was applied to detect the building from high resolution IKONOS images (GuGuo & Yasuoka, 2003). In this approach the active contour or the snake based building detection method was integrated with the height information. This approach helps to reduce the limitation of building boundary detection in snake based model alone from the high resolution satellite images.

The fusion of optical image and LIDAR data was used for the automatic building detection and modelling with region based segmentation and knowledge based classification (Chen et al., 2004). This approach was tested with a Quick Bird image and LIDAR data of Hsinch area in north Taiwan. The accuracy of building detection was satisfactory but it was limited to the flat roof buildings. Another LIDAR data integration for building detection is the combination of pan-sharpened multispectral IKONOS image and airborne laser scanning data (Sohn & Dowman, 2007). This approach was carried out with the Binary Space Partitioning tree algorithm. This method can also be used for the change detection in urban areas. The LIDAR data was integrated with an aerial image to identify the buildings applying polyhedral models (Huber et al., 2003). This method was not applicable for the buildings with irregular roofs. The structure, contextual and spectral information have been used for the building detection from high resolution IKONOS images of Columbia city in Missouri (Jin & Davis, 2005). In this method the differential morphological profile (DMP) was produced with mathematical opening and closing operators then DMP was used to identify the buildings and size and shape of the adjacent buildings were detected using the shadow. The small bright buildings were detected with the spectral property. This integration of contextual and spectral properties shows reliable accuracy in building detection.

The spectral and spatial data integration using MRF and SRM has not applied for the detection of the building footprints from the high resolution satellite images in the history. The novelty of this study is the application of MRF and SRM based data integration for the building footprint detection from the high resolution satellite images and this will solve some of the difficulties in other methods.

## **2.7. Summary**

In this chapter the theoretical background of the techniques applied for the building detection approaches was discussed. The techniques such as Maximum Likelihood image classification, Artificial Neural Network, Object Oriented image analysis and the data integration were discussed in brief. Then the some studies for which those techniques were applied for the building detection from high resolution satellite images and combination of satellite images with other data sources was reviewed. Then the integration of spectral and spatial data of both MS and panchromatic images method by MRF based SRM was discussed. As the shape and size of the building footprint detection is still a challenging task and the MRF based SRM method is sensitive to the shape and size of the objects this research is aim to developed a method to detect the building footprint using MRF based SRM.

## 3. SUPER RESOLUTION MAPPING TECHNIQUES

### 3.1. Effect of mixed pixel in object detection from Remote Sensing images

The detection of objects is one of the vital applications of the remotely sensed images. The objects are man-made and natural features on the Earth surface. Those objects are observable with the Remote Sensors which use the radiation reflected from those objects. The brightness of the objects in a remotely sensed image depends on the amount of radiation that the sensor received from the object and the visibility of the objects depends on the spatial and spectral resolution of the sensor. The spatial resolution of the sensor depends on the Instantaneous Field of View (IFOV). If the IFOV is smaller than the size of the object then the objects can be detected from the image. If the IFOV is larger than the size of the interest object then the object is difficult to identify. So the objects detection from satellite images directly related to the spatial and spectral resolution of the sensor. Normally the classification is the main process in most of the objects identification approaches. In automated classification the labelling of pixel is done according to the Digital Number (DN value) of the pixel that related to the reflectance of the objects. The pixels inside the objects are more likely to have the pure reflectance but the pixels on boundary of the objects have influenced with the reflectance of the adjacent objects. This will result into mixed pixels. Normally most of the object detection algorithms are based on the hard classification techniques. As hard classification assigns the class label per pixel, the mixels pose problem in assigning the class labels in the building detection with hard classification (Foody & Mathur, 2006; Liu et al., 2010).

The groups of pixels represent the objects in the image but the objects are not exactly fitted with the pixels as the resolution of the sensor and the size of the objects are not correlated. Therefore the pixels with heterogeneous objects exist in the remotely sensed images. Those pixels are the mixed pixels. Actually those are the pixels for which the sensor received the reflectance from more than one objects within the Instantaneous Field of View of the sensor and its surrounding objects. In other words the mixed pixels consist of more than one different type of materials. When the spatial resolution of the sensor is low then more than one adjacent object are within the IFOV. Therefore the spectrum received to the sensor is a composite of reflectance from those materials. This type of spectral mixing occurs when the sensor is at high altitude or the IFOV is wide. The abundance of mixed pixel depends on the spatial resolution of the sensor and the size of the objects. Even for the high spatial resolution sensor such as IKONOS, QuickBirds, Geoeye and World view the images are possible with mixed pixel as the size of some objects are smaller than the spatial resolution of the such high resolution sensors and the boundary of the objects do not exactly follow the pixel boundary. It is less possibility to have pure pixels in coarser resolution images even if the IFOV of the sensor fits with the homogeneous material as the sensor receives the scattered radiation from the neighbouring objects (Cracknell, 1998). The present of mixed pixels in an image is one of the major problems affecting the accuracy of the object detection (Kasetkasem et al., 2005; Wang et al., 2007). The limitation of the mixed pixels in hard classification can be minimized with the soft classification algorithm. The accuracy of the soft classification depends on that of the determination of the pure pixels which is referred to as the endmembers.

### 3.2. Sub pixel classification

The object detection from the remote sensing images is generally carried out with image classification techniques. The traditional image classification techniques are hard classifiers which assign a single class label to each pixel. In these classifications the mixed pixels are labelled with the land cover class which covers a large part of the mixed pixels. So the hard classification causes loss of the information present in

the mixed pixels. To overcome this limitation of hard classification the sub pixel classification or the soft classification has been introduced for the remote sensing image analysis. The soft classification algorithms decompose the mixed pixels into the spectra of corresponding land cover class as proportions of the mixed pixel. The soft classification assigns more than one class label to the pixel according to the proportion of the land cover area present in the pixel. Unlike hard classification the sub pixel classification results in a number of proportion images that is equal to the number of land cover classes used for the classification. Figure 3.1 illustrates the output of the soft classification versus the hard classification.

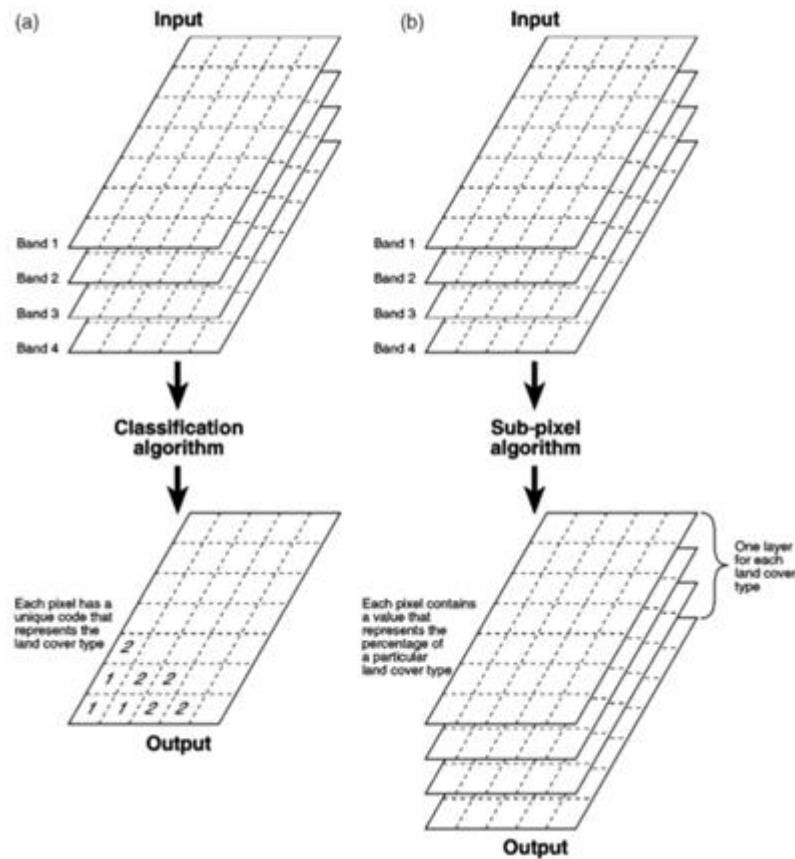


Figure 3.1: Output of hard classification and soft classification: (a) hard classification output one thematic map, (b) thematic maps per land cover class from soft classification (Source Lucas et al., 2002).

Soft classification is more suitable than hard classification in case of mixed pixels. The soft classification is carried out with multispectral images or single band image or panchromatic images. The determination of the class proportions in the mixed pixels can be done with different soft classification algorithms such as spectral mixture modelling, neural network and the fuzzy c means classification. These sub pixel algorithms assign the proportion for each land cover classes present in the mixed pixel and produce the thematic map for each land cover class with proportions as shown in Figure 3.3. The class proportion determination algorithms assigns the proportion values for each classes between 0 and 1. The high class proportion is assigned to the class with large area and low proportion for the small area present within the mixed pixel. Out of those sub pixel classification algorithm this study focuses on spectral mixture modelling.

### 3.2.1. Linear spectral unmixing

The spectral unmixing is the process of decomposing the measured spectrum of a mixed pixel into the individual spectra or the endmembers of each land cover class within the IFOV of the sensor and produce the corresponding proportion maps for each land cover class separately. In other words the spectral

unmixing is the inverse process of sensed reflectance by a sensor. The interaction of the radiation with the ground features could be linear or nonlinear as illustrated in Figure 3.2. Therefore the spectral unmixing models can be categorized into linear or nonlinear spectral unmixing models depending on the radiation reflectance at the object on the earth surface (Keshava, 2003). This study focused on the linear spectral unmixing.

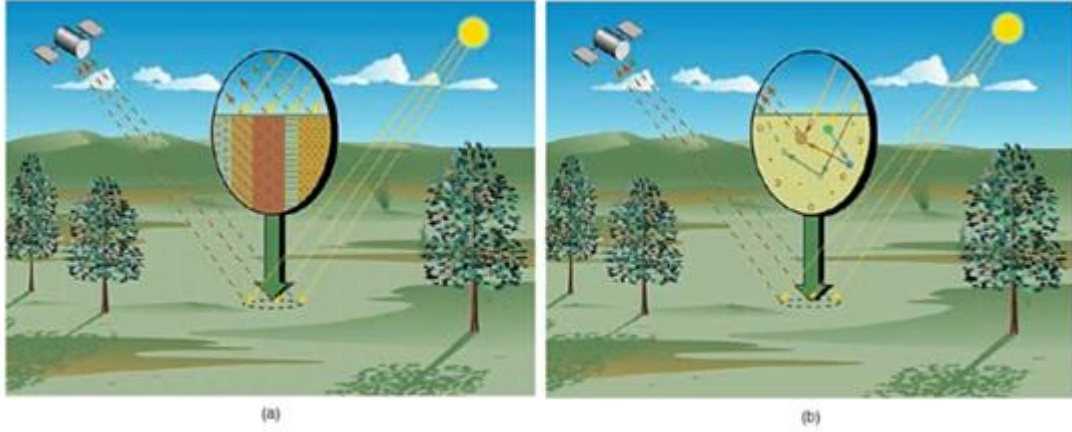


Figure 3.2: Linear mixing (a) and nonlinear mixing (b) at the Earth surface (Source: Keshava, 2003)

The solar radiation incident on the surface element of the objects reflects to the remote sensor after one bounce on the object element. At this situation the amount of reflectance is equal to the sum of fractional reflectance from each material within the IFOV of the sensor. Then the spectrum recorded in the sensor is the linear combination of the spectra of each material within that pixel. Therefore the measured reflectance can be modelled as the linear combination of the reflectance from each material within the pixel. This spectral mixture modelling is referred to as the linear spectral unmixing and it is based on the assumption that the spectral response for a pixel is a linear combination of the reflectance from each land cover classes within the pixel of interest (Atkinson et al., 1997). If  $\mu_{ki}$  is the mean spectral value or the endmember spectrum of  $i^{\text{th}}$  land cover class in  $k$  band, the observed spectrum ( $y$ ) of any pixel in that class can be defined by the following relation.

$$Y = \alpha_i \mu_{ki} + e_i \quad 3.1$$

Where  $\alpha_i$  is the proportion of  $i^{\text{th}}$  land cover class within the mixed pixel and  $e_i$  is the error due to sensor noise, endmember variability and other imperfect modelling errors in the reflectance value of  $i^{\text{th}}$  land cover class. Then the total observed spectrum of the mixed pixel with  $m$  land cover classes in band  $k$  ( $Y_k$ ) can be defined as:

$$Y_k = \alpha_1 \mu_{k1} + \alpha_2 \mu_{k2} + \alpha_3 \mu_{k3} + \dots + \alpha_i \mu_{ki} + \dots + \alpha_m \mu_{km} + e_1 + e_2 + e_3 + \dots + e_m \quad 3.2$$

$$Y_k = \sum_{i=1}^m \alpha_i \mu_{ki} + e_k \quad 3.3$$

Where  $e_k$  is the total error from all land cover classes in band  $k$ , the proportions should be positive and the sum of the proportions should be equal to one. This model for decomposing the spectrum of mixed pixel is known as the linear spectral unmixing. This model leads to a system of linear equations which can be solved by singular value decomposition (SVD) to avoid the difficulty in matrix inversion. This model has been used for the soft classification in this study as it is a potential solution for the sub pixel classification (Lucas et al., 2002).

### 3.3. Supper Resolution Mapping

The soft classification produces a number of proportion images which is equal to the number of land cover classes used in the classification. In these images several land cover class labels are assigned to a specific pixel but it does not specify the location of the land cover proportion within the pixel. For the assignment of the location of land cover proportion within the pixel, a technique known as super resolution mapping was suggested by Atkinson et al., (1997). The super resolution mapping technique is also referred to as the sub pixel mapping, super resolution classification and pixel unmixing. This technique is a step beyond the sub pixel classification and it is the estimation of the spatial distribution of land cover proportions produced by sub pixel classification. The SRM is based on the spatial dependency of the land cover classes. This means that the pixel is more likely to have the label of neighbouring pixel than that of far away pixel. On the basis of this fact the task of the SRM is to determine the most probable location for the fraction of the land cover class inside the pixel. This is carried out by dividing the coarser resolution pixel into finer resolution pixels and then assigning the location for sub pixel with the maximization of the spatial dependency. In this way the SRM synthetically generates a finer resolution thematic image from the coarser resolution image. The ratio between the coarser resolution pixel size and the finer resolution pixel size is defined as the scale factor of the sub pixel mapping. The synthesis of the finer resolution thematic map from the coarser resolution remote sensing image is illustrated in Figure 3.3. The sub pixel mapping technique utilizes the useful information within the mixed pixel in the land cover classification but the hard classification algorithms lose this information in image analysis. That is the main advantage of the soft classification over the conversional hard classification.

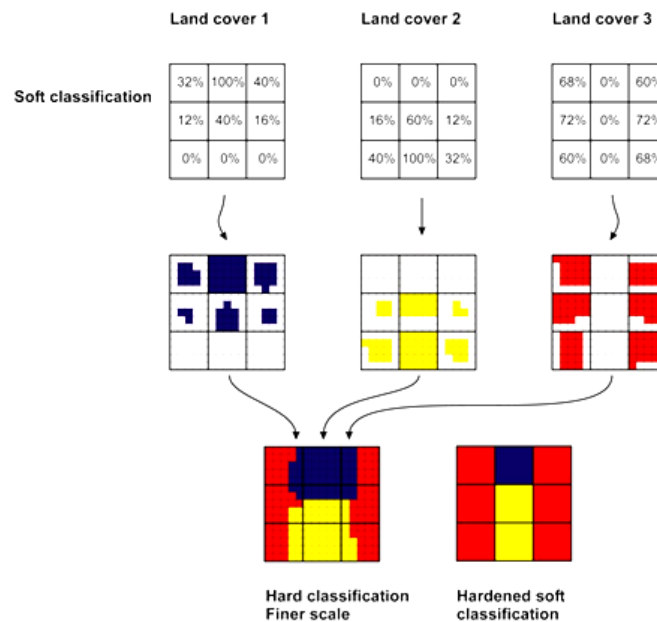


Figure 3.3: Overview Super Resolution Mapping process and harden version of soft classification image (Source: URL-2)

The SRM technique is still on research for the development with different type of methods. There are different type of methods developed for SRM with different techniques such as SRM with two point histogram (Atkinson, 2004), SRM with multiple point geostatistics (Boucher, 2008), SRM with stochastic simulations, SRM with MRF (Kasetkasem et al., 2005), and SRM with a Hopfield Neural Network (Nguyen et al., 2005). Out of these SRM method this study is focused on the SRM based on MRF developed by (Tolpekin et al., 2010) as it facilitates the integration of spatial and spectral data of the MS and panchromatic images. In the MRF based SRM the labelling of a pixel is carried out with the posterior probability of the pixel. The posterior probability of a pixel belonging to a land cover class is the

combination of the prior probability and the conditional probability. It is calculated using the Bayesian theory as shown in Equation 3.4. The posterior probability ( $P(w_j | x_i)$ ) of a pixel  $x_i$  belonging to class  $w_j$  can be defined as:

$$P(w_j | x_i) = \frac{P(x_i | w_j) P(w_j)}{P(x_i)} \quad 3.4$$

Where  $P(x_i | w_j)$  is the conditional probability of  $w_j$  given pixel  $x_i$  and  $P(x_i)$  and  $P(w_j)$  are the prior probability of pixel  $x_i$  and the land cover class  $w_j$ . The pixel is assigned a label with the class for which the posterior probability is at maximum. The criterion is known as the Maximum A Posterior probability solution (MAP) and defined as below assuming that the prior energy of the pixel is uniformly distributed.

$$w_k = \arg \max_w \{P(x_i | w_j) P(w_j)\} \quad 3.5$$

where  $w_k$  is the class of pixel  $k$ .

The prior probability is derived from the prior information of the pixel and conditional probability is calculated using the land cover class statistics. The prior is derived with the context of the pixel of interest. The context is derived from the spatial, spectral or temporal information of the neighbouring pixels. The aim of the contextual information is to obtain a smooth thematic map from the image classification. Therefore this is referred to as the smoothness prior. It is achieved by modelling the image as a Markov Random Field.

### 3.3.1. Markov Random Field (MRF)

The MRF is commonly used in the remote sensing image classification for the integration of contextual information. In practical application MRF is related with Gibbs Random Field (GRF) to model the context in the satellite images. A random field is a set of random variables defined on a set containing number of sites in which each random variable takes a label from a label set. Let  $w$  be a realization from a random field  $W$ . and  $W$  is a set of random variable  $w_1, w_2, w_3, \dots, w_m$  indicating all possible values for  $w$ . A random field is a Markov Random Field with respect to a neighbouring system if the probability density function of the random field  $w$  satisfies the following three conditions (Tso & Mather, 2009).

- a) Positivity for all possible configurations of  $w$ ;  $P(w) > 0$
- b) Markovianity property which indicates that the assigning label to a site(pixel) is only dependent on its neighbouring sites;  $P(w_i | w_{S-i}) = P(w_i | w_{N_i})$
- c) Homogeneity that denotes that the conditional probability for the label of site ( $i$ ) given labels of adjacent pixels is independent of the relative position of the site ( $i$ ) in set ( $S$ );  $P(w_i | w_{N_i})$  is same for all sites  $i$  in  $S$ .

The MRF is defined on the neighbouring system. The neighbouring system has an order with respect to the relative position of the pixels in an image. The order can be defined as first, second, third, fourth, fifth and even more. The first order neighbouring system of a pixel is the four pixels having a common side with the interested pixel. The second order neighbouring system is the surrounding four pixels sharing a corner with the given pixel. Likewise the higher order neighbouring systems can be defined as shown in the diagram bellow. Figure 3.6 shows the neighbouring systems up to the fifth order.

5	4	3	4	5
4	2	1	2	4
3	1	i	1	3
4	2	1	2	4
5	4	3	4	5

Figure 3.4: Fifth order neighbourhood system

The MRF specifies that the labelling of given pixel is dependent on the neighbours of the interested pixel and the Gibbs random field describe as it depends on the global labelling of the pixel in the image (Tso & Mather, 2009).

### 3.3.2. Gibbs Random Field (GRF)

A random field  $w$  is a Gibbs Random Field if its probability density function  $P(w)$  satisfies the following form.

$$P(w) = \frac{1}{Z} e^{-\frac{U(w)}{T}} \quad 3.6$$

Where  $w$  is the random field defined as above,  $U(w)$  is defined as the energy function of the random field  $w$ ,  $T$  is the constant known as temperature and  $Z$  is referred to as partition function. According to the probability density function of GRF the maximization of probability is equivalent to the minimization of energy function of the random field. The energy function  $U(w)$  of the random field can be defined as the summation of the all possible potential with respect to a clique type as shown in equation below.

$$U(w) = \sum_c V_c(w) \quad 3.7$$

Where  $V_c(w)$  is the potential function defined with respect to the clique type  $C$ . Figure 3.5 shows the different type of cliques type in the first and second order neighbouring system.

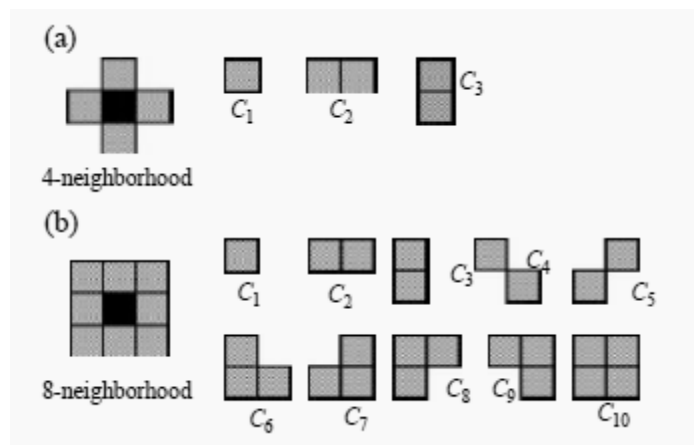


Figure 3.5: Cliques for four neighbourhood (a); eight neighbourhood (b)

The GRF defines the global effects on the pixel labelling of an image and the MRF defines the local effects on assigning the labels to pixel in an image. The Hammersley Clifford theorem specifies that there exists a unique GRF defined in terms clique type on a neighbouring system for every MRF. The posterior probability of a given pixel can be defined in terms energy functions and simplified to the following form

shown in the equation below (Tolpekin & Stein, 2009). Then the MAP solution can be achieved by minimization the posterior energy.

$$U(w|x) = \lambda U(w) + (1 - \lambda)U(x|w) \quad 3.8$$

where  $\lambda$  is the smoothing parameter between the prior and likelihood energy.

### 3.4. Data integration with MRF based SRM

The images of different resolution can be integrated using the SRM based on MRF in the image classification (Tolpekin et al., 2010). The SRM generates a finer resolution thematic image from a coarser resolution image. A SR map is sought from both a MS remote sensing image  $y$  with  $K$  spectral bands and spatial resolution  $R$  and a panchromatic image  $z$  with finer spatial resolution  $r$  ( $r < R$ ) of the same ground area. In addition it is assumed that there is a MS image with spatial resolution  $r$  and  $K$  bands of the same area. The images  $y$  and  $z$  are observed ones and those are spatial and spectral degradation of image  $x$  and  $x$  is not observed. The integration of spectral and spatial data can be carried out with the following relationships between images  $x$ ,  $y$  and  $z$  (Tolpekin et al., 2010) assuming that the spectral values of each land cover class is normally distributed, the point spread function of the pixel is uniform and the spectral response function of panchromatic band is the average of that of the four bands of MS image.

$$y_k(b_i) = \frac{1}{S^2} \sum_{j=1}^{S^2} x_k(a_{j|i}) \quad 3.10$$

Where  $k= 1, \dots, K$ ,  $S$  is the integer scale factor between the spatial resolution of MS and panchromatic images,  $b_i$  is the pixel location of thematic map  $y$  and  $a_{j|i}$  is the corresponding pixel of image  $x$ . And

$$z(a_{j|i}) = \frac{1}{K} \sum_{k=1}^K x_k(a_{j|i}) \quad 3.11$$

Where  $z(a_{j|i})$  is the corresponding pixel location in panchromatic image for that of  $x_k(a_{j|i})$  in assumed MS image. According to this data integration, the posterior probability for the SR map  $c$ ,  $P(c|y,z)$ , given observed image  $y$  and  $z$  can be determined with the prior probability  $P(c)$  and likelihood probabilities of  $P(y|c)$  and  $P(z|c)$  as given below by assuming the images  $y$  and  $z$  are conditionally independent

$$P(c|y, z) \propto P(c)P(y|c)P(z|c) \quad 3.12$$

The corresponding energy function for data integration can be derived from following

$$U(c|y,z) = \lambda U(c) + (1 - \lambda)\{\lambda_p U(z|c) + (1 - \lambda_p)U(y|c)\} \quad 3.13$$

Where  $U(c|y,z)$  is the posterior energy,  $U(c)$  is the prior energy,  $U(z|c)$  is the conditional energy of panchromatic image ( $z$ ) given initial SRM ( $c$ ),  $U(y|c)$  is the conditional energy of MS image ( $y$ ) given initial SRM,  $\lambda$  ( $0 < \lambda < 1$ ) is the parameter balancing the contribution of prior and conditional energy functions. And  $\lambda_p$  ( $0 < \lambda_p < 1$ ) is the parameter balancing the contribution of two conditional energy functions based on panchromatic and multispectral images respectively; these parameters smooth the SR map;  $c$  is the SR map;  $z$  is panchromatic image and  $y$  is multispectral image. Then the MAP solution can be obtained by minimizing the posterior energy function instead of maximizing the posterior probability (Geman & Geman, 1984). This is referred to as energy optimization.

Assuming that the SR map is a MRF the prior energy function can be modelled by Equation 3.14 using the Gibbs Random Field (GRF)-MRF equivalence.

$$U(c) = \sum_{i,j} U(c(a_{j|i})) = \sum_{i,j} \sum_{a_1 \in N(a_{j|i})} w(a_1) I(c(a_{j|i}), c(a_1)) \quad 3.14$$

where  $U(a_{j|i})$  is the local contribution of pixel  $(a_{j|i})$  to the prior energy;  $N(a_{j|i})$  is the neighbourhood system;  $w(a_1)$  is the weight of contribution from neighbour pixel  $a_1$  in neighbourhood system  $N(a_{j|i})$  and  $I(c(a_{j|i}), c(a_1))$  take the value 0 if  $c(a_{j|i}) = c(a_1)$  and 1 otherwise. The weight of the neighbour pixel  $a_1$  is inversely proportional to the distance between the central pixel to the pixel  $a_1$ .

The likelihood energy of the panchromatic and multispectral image is modelled by assuming the pixel values of each land cover class in panchromatic and multispectral image are normally distributed. The likelihood energy of MS image ( $y$ ) can be defined in Equation 3.15.

$$U(y|c) = \sum_i \frac{1}{2} \left[ M(y(b_i), \mu_i, C_i) + \frac{1}{2} |\det C_i| \right] \quad 3.15$$

Where  $M(y(b_i), \mu_i, C_i)$  is the Mahalanobis distance between the pixel value  $y(b_i)$  and mean vector  $\mu_i$ ;  $C_i$  is the covariance matrix of class  $i$ . Similarly the likelihood energy of panchromatic image  $U(p|c)$  can be modelled by Equation 3.16.

$$U(z|c) = \sum_{i,j} \frac{1}{2} \left[ \frac{(z(a_{j|i}) - \mu_a)^2}{\sigma_a^2} + \ln \sigma_a^2 \right] \quad 3.16$$

Where  $z(a_{j|i})$  is the pixel value and  $\mu_a$  is the mean value with standard deviation  $\sigma_a$  of the class  $c(a_{j|i})$  respectively.

### 3.5. Energy optimization

The aim of optimization is to assign a class label to the pixel for which the probability belonging to that class is at maximum with the spatial dependency. This is also equivalent to the minimum energy of the pixel that is more likely to be a member of the land class. The minimum energy function described in the previous section could be reached with the MAP approach. The MAP is a global maximum solution and it is not easy to obtain with the conventional methods such as gradient descent techniques. Therefore the MAP solution is achieved through an energy optimization algorithm. There are different types of such optimization algorithms. Those can be categorized into stochastic and deterministic algorithms (Grava et al., 2007). The widely used stochastic minimization algorithms are Simulated Annealing (SA), Maximizer of Posterior Marginals (MPM) and genetic algorithms. The deterministic algorithms are Iterated Conditional Modes (ICM), Gradual non convexity (GNC) and Mean Field Annealing (MFA). Out of those algorithms this study is only focused on SA (Geman & Geman, 1984) and ICM (Besag, 1986) to compare the quality of the SRM optimized from stochastic algorithm and the deterministic algorithm as both are popular for optimization process.

#### 3.5.1. Energy optimization with SA

The simulated annealing is a stochastic relaxation algorithm (Geman & Geman, 1984) which is used to find the global minimum of the non-converging energy function. It uses random numbers and probability to find the global optimization of the process. It works in the manner of freezing liquids or recrystallizing metals (Selim & Alsultan, 1991). The energy optimization process with SA is controlled by two parameters known as annealing parameters. Those annealing parameters are initial temperature ( $T_0$ ) and temperature updating rate ( $T_{upd}$ ). The initial temperature provides the randomness to the process and the updating rate decreases the temperature of the process in the next iteration until the temperature at the start of the iteration tends to zero. The randomness of the system depends on the initial temperature value. For higher values of temperature the randomness is higher and vice versa. In this manner the MAP solution is achieved for the pixel labelling in the initial SRM with the posterior energy by setting the appropriate initial temperature and the updating schedule.

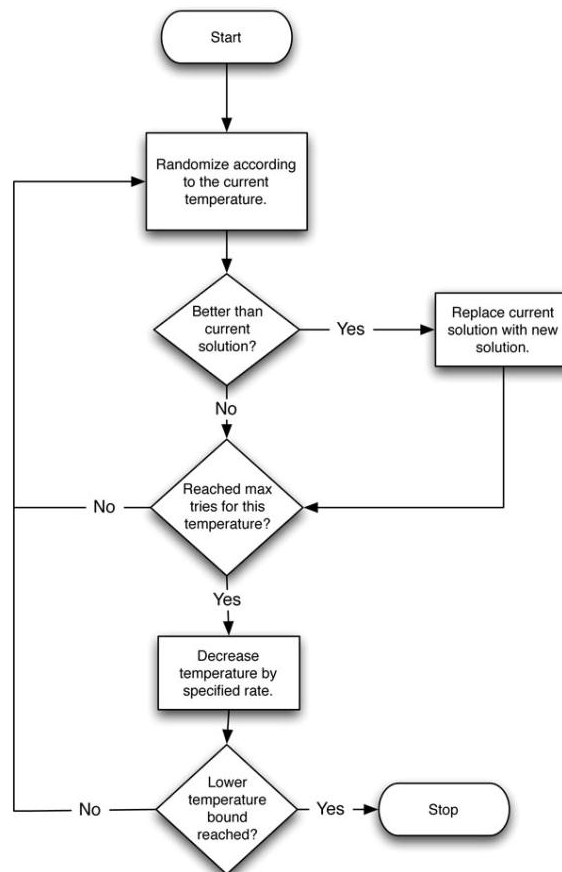


Figure 3.6: Schematic diagram of SA optimization

Figure 3.6 shows the schematic diagram of the simulated annealing algorithm. It illustrates two main process of the SA optimization. First one is that SA runs a predefined number of cycles with the inputs. Then the second one is that the temperature is lowered with the user defined condition. When the temperature reaches the lowest value allowed then the energy function has reached to minimum and SA will terminate and the label of pixel will not be updated further.

### 3.5.2. Energy optimization with ICM

Iterated conditional modes is a deterministic optimization algorithm (Grava et al., 2007). The founder of this algorithm is Besag in 1986. ICM estimates the probability of the pixel having same colour in a neighbouring system (Besag, 1986). It converges to a local minimum of the energy function based on two assumptions. First, the pixels in the observed image are class conditional independent and each component has the same known conditional density function dependent only on the corresponding label. Secondly it is assumed that the class label depends on labels of the local neighbourhood. In other words the image holds the Markovian properties. The main advantage of the ICM is that it is computationally fast when compared to other stochastic optimization algorithm like Simulated annealing and genetic algorithm and the disadvantage is that ICM could remain at a local minimum(Grava et al., 2007).

## 3.6. Summary

This chapter mainly focused on the theoretical background of the super resolution mapping techniques. It has described the mixed pixel generation and its limitation in image classification. Then the details of spectral mixture modelling were illustrated. The super resolution mapping and the energy optimization have also been described in detail.



## 4. STUDY AREA AND DATA PREPARATION

### 4.1. Study area

The study area for this research is selected in the newly build-up area at Lampuuk village in Aceh, Indonesia. The Lampuuk village is around 20 KM to the south west of Banda Aceh which is the provincial capital and the largest city in Aceh at Sumatra island of Indonesia. It is located approximately in 5°33'N latitude and 95°19'E longitude. Lampuuk was severely damaged area due to the tsunami on 26 December 2004. Due to the tsunami disaster many people lost their lives and most of buildings and other infrastructures were destroyed. After the tsunami foreign donors constructed the new buildings for the homeless in Indonesia. Lampuuk is the one of such villages. This area is selected for the study as there are new buildings with different spectral properties and those are small detached buildings. The buildings in this area have simple shape that will lead to improve the quality of the SRM. Most of buildings are separated from each other by a distance around 2 to 3 meters. Most of the buildings are surrounded by grass land. The buildings' roofs are red, blue and white in colour and most roofs are red. The remaining area of the image consists of vegetation, bare soil and roads. Because of those properties Lampuuk village has been selected for the study. According to spectral properties of the features in the image, six classes can be identified to for the classification. They are red roof building, blue roof building, white roof building, vegetation, bare soil and road (see Figure A1 in Appendix A for the photographs of the site). These classes can be visually distinguished in the bottom image of Figure 4.1. Figure 4.1 shows the location of the study area in Sumatra Island in upper image and the study area in Lampuuk village is on the bottom image.

### 4.2. Data for the study

The data selected for the study is the high resolution KOMPSAT-2 satellite images. KOMPSAT-2 is the synonym for the KOrean Multi-Purpose SATellite which was launched on July 28<sup>th</sup> 2006 by Korean Aerospace Research Institute (KARI) (Leea et al., 2008). For this study I have selected the panchromatic image and multispectral image which were acquired on 25<sup>th</sup> May 2007. The details about the spatial and spectral resolution of those two images are given in Table 4.1 and the coordinates of the images are given in Table 4.2. According to the meta data, these images are in level L1R. The radiometric corrections have already been done for the level L1R data (KOMPSAT-2 Image data manual for user, 2008). Therefore the co-registration was carried out for the images.

Table 4.1: Spectral and spatial resolution of the selected images (Source: Leea et al., 2008)

Image	Spatial Resolution	Spectral Bands
Panchromatic	1 m	500nm - 900nm
Multispectral	4 m	Band1 (Green): 450nm ~ 520nm Band 2 (Blue): 520nm ~ 600nm Band 3 (Red): 630nm ~ 690nm Band 4 (NIR): 760nm - 900nm

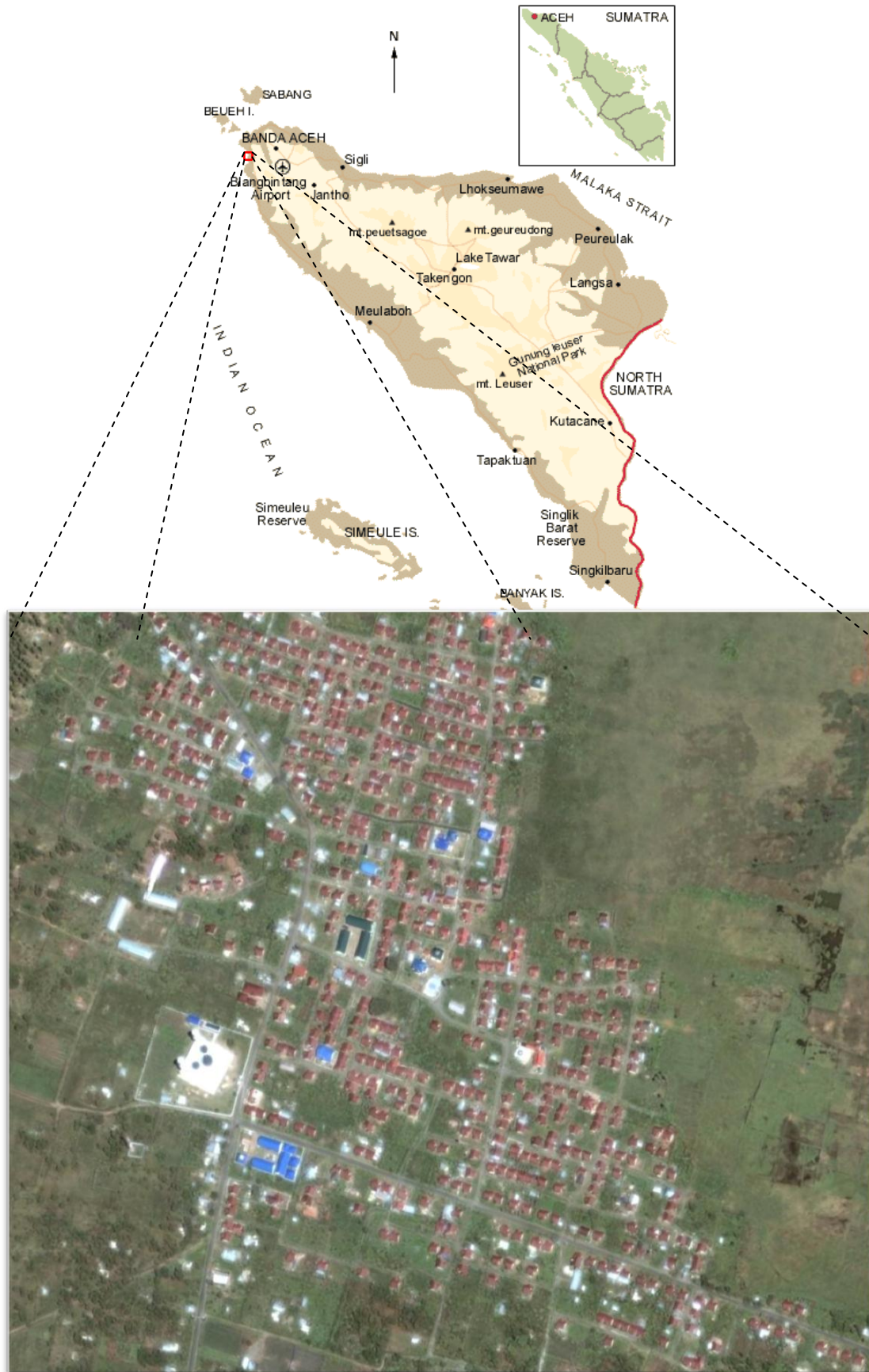


Figure 4.1: Study area – Lampuuk in Aceh, Indonesia (Source: URL-3 and Google Earth on 07/02/2011)

Table 4.2: Coordinates of the area covered by the selected images

Vertex	Geographical coordinates		Image coordinates			
	Latitude (North/Degree)	Longitude (East/Degree)	MS		Panchromatic	
			Row	Column	Row	Column
Upper left	5.57497868	95.16139546	1	1	1	1
Upper right	5.60806394	95.32796834	1	3750	1	15000
Lower left	5.42893723	95.19158988	3750	1	15000	1
Lower right	5.46204132	95.35811909	3750	3750	15000	15000

### 4.3. Image co-registration

The proposed building detection approach is based on the integration of spatial and spectral data of the very high resolution images using the MRF and SRM techniques. For this data integration the accurate geometric registration of the images is very significant (Tolpekin et al., 2010). The geometric registration of images can be achieved with georeferencing or co-registration. As it is important that the images are not resampled for the MRF, the co-registration was selected for the geometric registration of the images. The image co-registration is the process in which the two dimensional positions of all pixels in two or more images of same geographical area are brought to one coordinate system on one to one basis of pixel. In other words this will bring the two images of same area in to same coordinate system. The co-registration of two or more images can be performed in two ways. Those are map based image registration and image to image registration (Richards & Xiuping, 2006). The image to image registration was applied for this study as it is sufficient to bring both images to one coordinate system.

The image to image registration is carried out with MS and panchromatic images. The high resolution panchromatic image is chosen as master image which is assumed to be geometrically corrected and MS image is used as slave that is to register to the master image coordinate system (Richards & Xiuping, 2006). The main task of this method is the selecting of tie points on Master image and corresponding points on the slave image for the coordinate transformation. The tie points are the sharp image points that clearly appear on both images. The tie points selected are building corners and intersection of natural and manmade features such as rivers, roads and ridges. Those are selected to be distributed over the entire image. The number of tie points depends on the selected transformation. In general it is better to have many tie points distributed over the entire image space for accurate co-registration. The first order or second order polynomial transformation is generally used for the coordinate transformation in image to image registration as it corrects the errors in shift and rotation. The image registration is carried out in ERDAS IMAGINE 2010 software with second order polynomial transformation. The RMS error of the co-registration is 0.0289 pixels (see Figure B1 in Appendix B for the result of co-registration). Then the horizontal and vertical distances between the pixel grids is checked with SWIPE operation in ERDAS IMAGINE 2010. The horizontal distance between grid line of panchromatic image and that of MS image is 0.30 pixels and the vertical distance difference is 0.24 pixels. Those are less than a half of the finer resolution pixel. Therefore the co-registration of panchromatic image with MS image is accurate enough for the super resolution mapping. The resampling is not done to avoid the changes of the original reflectance values of the images.

### 4.4. Sub set image preparation

The two type sub set images are prepared from the co registered MS and panchromatic images. One set of subset images is to cover the entire study area. The dimension of the MS subset image is 100 by 100 pixels and that of panchromatic image is 400 by 400 pixels. For the computational convenience in iterative process of smoothing and annealing parameter estimation, a subset of even smaller images is prepared

from both the MS and the panchromatic image separately. The small images is named as “tuning image” and the dimension of MS tuning image is 21 by 21 pixels while that of panchromatic tuning image is 84 by 84 pixels. Both the subset images and tuning images is converted to ASCII format using ENVI software as it is the compatible format for R software. The coordinates and dimension of subset images are shown in Tables 4.3 and 4.4 while the images are shown in Figures 4.2 and 4.3.

Table 4.3: coordinates and the dimensions of the study area

Image	Upper left corner coordinates		Lower right coordinate		Dimension
	Row	Column	Row	Column	
Panchromatic image	4850	-9250	5250	-9650	400 × 400
MS image	4850	-9250	5250	-9650	100 × 100

Table 4.4: coordinates and the dimensions of the tuning image

Image	Upper left corner coordinates		Lower right coordinate		Dimension
	Row	Column	Row	Column	
Panchromatic image	5038	-9558	5122	-9642	84 × 84
MS image	5038	-9558	5122	-9642	21 × 21



Figure 4.2: Sub set images of the study area (MS image at right and panchromatic image at left)

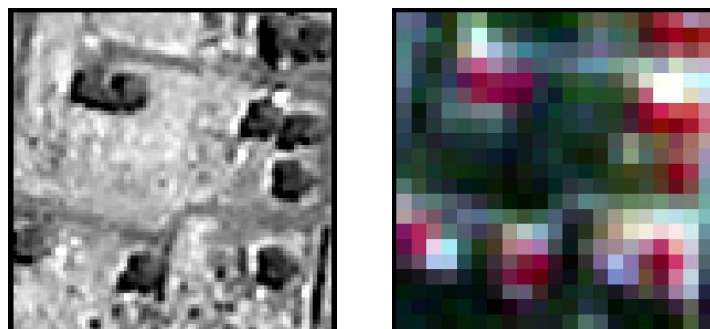


Figure 4.3: MS (right) and panchromatic (left) tuning images

#### 4.5. Class definition

The classes were selected based on the spectral properties of the features in MS image of the study area for the classification as described in Section 4.1. From the visual interpretation of panchromatic image of the study area the shadow class could be identified. Therefore it is also taken as class for the soft classification to avoid the confusion with other classes. The class means and variances for the shadow class in four bands of MS image were assumed to be same as that of the panchromatic image and the covariances of four bands in MS image are also assumed to be zero. That is an assumption made for this study. Then the mean vectors and variances for each class except shadow are calculated using the MS image of the study area in ERDAS IMAGINE 2010. Those statistics for the shadow are calculated using the panchromatic band and they are accepted for the four bands of MS image as it is difficult to identify the shadow of the buildings in MS image. The mean vectors and variances are given in Table C1 to C8 in Appendix C. The mean and the standard deviation of the each land cover class in panchromatic image are given in Table C9 in Appendix C. The class separability is evaluated with the transform divergence. The transform divergences (TD) between the classes are calculated in R software (see Appendix F for R code) to check the level of separability between the classes. The calculated TD values are shown in Table 4.5 and 4.6. According to the TD values all the classes are well separable in MS image as TD values are above the 1.9 (Tolpekin & Stein, 2009). But the classes are poor separable in panchromatic image as one third of the combination between the seven classes has a TD value less than 1.5. These separability measures show that the less contribution of panchromatic image and more contribution of MS image are suitable for the energy model in SRM optimization.

Table 4.5: Transformed divergence of the chosen land cover classes in MS image

Land cover Class	Red roof building	Blue roof building	White roof building	Vegetation	Shadow	Bare soil	Road
Red roof building		2.000	2.000	2.000	2.000	1.999	1.998
Blue roof building	2.000		2.000	2.000	2.000	2.000	2.000
White roof building	2.000	2.000		2.000	2.000	2.000	1.999
Vegetation	2.000	2.000	2.000		2.000	2.000	2.000
Shadow	2.000	2.000	2.000	2.00		2.000	2.000
Bare soil	1.999	2.000	2.000	2.000	2.000		1.929
Road	1.998	2.000	1.999	2.000	2.000	1.929	

Table 4.6: Transform divergence of the chosen land cover classes in panchromatic image

Land cover class	Red roof building	Blue roof building	White roof building	Vegetation	Shadow	Bare soil	Road
Red roof building		1.127	2.000	1.557	1.551	1.905	1.353
Blue roof building	1.127		1.999	1.852	0.120	1.998	1.526
White roof building	2.000	1.999		1.999	2.000	2.000	1.986
Vegetation	1.557	1.852	1.999		1.973	0.257	0.169
Shadow	1.551	0.120	2.000	1.973		1.999	1.881
Bare soil	1.905	1.998	2.000	0.257	1.999		0.945
Road	1.353	1.526	1.986	0.169	1.881	0.945	

#### 4.6. Image fusion

The image fusion was carried out with the co-registered panchromatic and multispectral subset images with pan-sharpen techniques in ERDAS IMAGINE 2010 for the building detection with MLC. Five methods which are available in ERDAS IMAGINE 2010 have been tested for the image fusion. Those are (a) wavelet resolution merge with principle component analysis (PCA), (b) resolution merge with PCA, (c) modified HIS resolution merge, (d) Ehlers fusion and (e) High Pass Filter (HPF). The fused images are shown in Figure 4.4 (a), (b), (c), (d) and (e). According to the visual interpretation the buildings in the fused images from wavelet resolution merge with PCA (a) and Ehlers fusion (d) are geometrically distorted. Therefore they were not selected for the building detection. The fused image from HPF (e) preserves the spectral properties of the buildings and background better than the fused image from modified HIS resolution merge (c) and resolution merge with PCA (d) according to the visual interpretation. Therefore the HPF fused image was selected for the building detection from MLC.



(a)



(b)



(c)



(d)

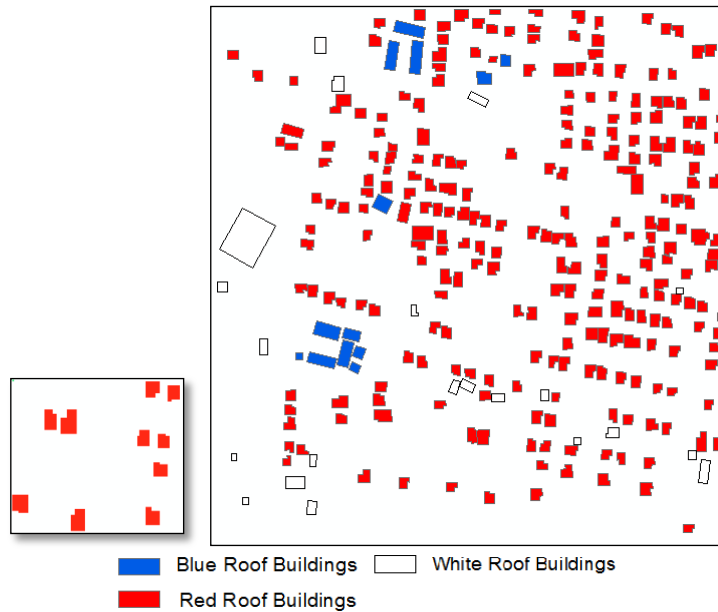


(e)

Figure 4.4: (a) fused images from wavelet resolution merge with PCA, (b) fused image from resolution merge with PCA, (c) fused image from modified HIS resolution merge, (d) fused image from Ehlers fusion and (e) fused image with High Pass Filter (HPF)

**4.7. Reference map preparation for tuning and study area for the SRM**

The reference map was prepared using the screen shot from Google Earth of the study area in Lampuuk, Indonesia. The screen dump of Google Earth was obtained to cover the entire study area. Then it was co-registered with the panchromatic image using image to image registration with first order polynomial transformation keeping the panchromatic image as the master image. The accuracy of the geometric correction is 0.25 pixel (see Figure B2 in Appendix B for the result of co-registration). Then two subsets from the co-registered Google Earth image were prepared in such a way that the dimension and the area of the small subset were similar to the tuning image and those of large subset were similar to subset of panchromatic image. Then each building of both subset images was digitized manually to complete the reference image for tuning image and study area respectively in Arc Map software as shape files. Finally the reference images were converted to the ASCII format to support the R software. The images are shown Figure 4.5 (a) and (b).



(a)

(b)

Figure 4.5: (a) Tuning Reference image, (b) Reference image for study area



## 5. PROPOSED BUILDING DETECTION APPROACH

The building detection methods from high resolution satellite images have been discussed in Chapter 2. Those methods are based on different remote sensing image analysis techniques. However there is still room for the study of building detection for further refinement of building detection accuracy. The new method is also based on the remote sensing image analysis techniques. The proposed approach is based on soft classification followed by super resolution mapping. This method is compared with the conventional MLC method. Then the validation of the method is done in pixel based and object based analysis. The building foot print detection method proposed by this research is based on the SRM and MRF. The main steps of this method are illustrated in Figure 5.1. It consists of three phases which are soft classification, SRM generation and building detection. The co-registered panchromatic and MS images in Section 4.3 are used for the building detection. Each of those phases will be described one by one in proceeding sections.

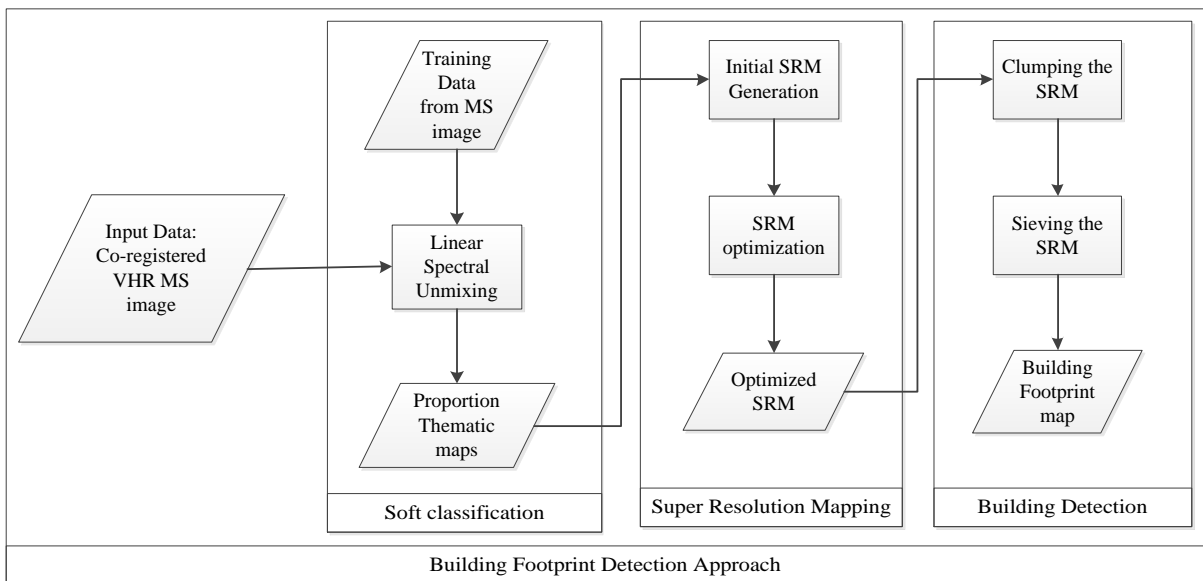


Figure 5.1: The proposed building footprint detection approach

### 5.1. Soft classification

In the proposed building detection approach, first step is the soft classification of multispectral images to obtain the land cover proportion images. The soft classification can be done in several methods as described in Section 3.4. From those methods the linear spectral unmixing is applied for this approach as it has shown satisfactory results in the literature and it is among the more popular techniques (Dobigeon et al., 2009; Foody, 2006; Van Der Meer & De Jong, 2000). The endmembers are the mean spectral value of the land cover class. The mean spectral values of the land cover classes are calculated using the signature editor of each land cover class in ERDAS IMAGINE 2010. The mean and covariance matrix for each class are calculated for each band of the land cover class. The class mean is taken as pure pixel and the class variation used for the determination of spectral variation within the class. After the calculation of means and variances of the each land cover class in both MS and panchromatic image, the linear spectral unmixing is applied to produce the proportion images for the selected classes. By applying the unmixing model the proportion images were produced for each land cover class using the “R, The Language and

Environment for Statistical Computing” software (see Appendix F for R code). Those land cover class proportion images will be used for the SRM generation.

## 5.2. Initial SRM generation

The soft classification provides the proportion or fraction image per land cover class but it does not specify the spatial distribution of the land cover class within the pixel. Then the next step of the new building footprint detection approach is the initial SRM generation. The initial SRM is prepared dividing the coarser pixels in proportion image by the scale factor in R software. In this research the scale factor is 4 as the spatial resolution of input image, KOMPSAT-2 MS images, is 4m and that output thematic map is 1m. The proportion images are 100 by 100 pixels so the initial SRM is 400 by 400 pixels. Each sub pixel is located within the pixel by random labelling the sub pixel with corresponding class from proportion image. The output of this step is a SRM with many isolated sub pixels. These sub pixels will be located with the optimization of spatial dependence in the SR map. The spatial dependence is optimized using the energy model described in Section 3.6. The energy model is developed using MRF and Gibbs energy formulation as described in Section 3.5.1 and 3.5.2. The optimal solution of the energy model is achieved with MAP solution.

## 5.3. Energy modelling

The posterior energy function is modelled with prior and likelihood energy. The prior energy is modelled with MRF and GRF equalization using the contextual information of the pixels in initial SRM. The spatial context is the correlation between spatially adjacent pixels in the neighbourhood (Solberg, 1996). The likelihood energy is modelled with class mean vectors and covariance matrixes derived from the co-registered MS and panchromatic images. After the modelling the posterior energy, the MAP solution is achieved by minimization of the energy function (Geman & Geman, 1984). The Map solution is achieved using the SA. The principle behind the SA has been described in Section 3.7.1. The energy optimization is a tedious task in this process as it is time consuming task to determine the optimal smoothing parameters ( $\lambda$  and  $\lambda_p$ ) in the energy model and the optimal annealing parameters ( $T_0$  and  $T_{upd}$ ). Therefore the estimation of those parameters is carried out with the tuning images. The determination of optimal parameters is done by analysing the kappa values of the SRM. Then the optimized SRM for the study area is obtained by applying the optimal values estimated from the tuning image. The parameter estimation and optimized SRM generation are carried out in R software (see Appendix F).

## 5.4. Optimization of SRM with Simulated Annealing

Initial SRM is a noisy thematic map due to abundance of isolated sub pixels. Next step is the task to place the sub pixel in realistic way to obtain a proper building map by maximizing the spatial dependence in the image. The process of locating the isolated sub pixels in the manner of producing a thematic building map is referred to as the optimization. The optimization of initial SRM is carried out with the MAP solution. This is done by modelling posterior energy with the prior and conditional energy of the co registered sub set images of MS and panchromatic images as proposed by Tolpekin et al., (2010). In other words the optimization of initial SRM is carried out with the integration of spatial and spectral data of the MS and panchromatic images. The integration of panchromatic data is mainly because of the spatial limitation of the MS image.

## 5.5. Energy optimization with Iterated Conditional Modes

The Iterated conditional modes (ICM) is used for the comparison of stochastic optimization algorithm (SA), with deterministic optimization algorithm. The principle of the ICM is described in Section 3.7.2. For the ICM only the smoothing parameters are applied on the basis of the class conditional

independence and the dependence of the class labelling on the label of neighbouring pixels. This is also done in R software.

### 5.6. Building detection

The optimized SRM is a thematic map of individual sub pixel with class label. There are some small patches and isolated pixels in the optimized SRM. The pixels in the SRM is grouped with the operator named “clump” in ENVI and then the small patches and the isolated pixels are cleaned with the filter named “sieve” operator in ENVI with minimum size of seven pixels as the smallest building in the study area is approximately 8 by 8 meters in ground. The clumping and sieving are done in ENVI software. The building footprints are identified using the visual variable colour in the optimized SRM as the building classes are defined on the basis of roof colour. Then the building map is visualized in Arc Map software for the validation and comparison.

### 5.7. Building detection with MLC

The building detection using maximum likelihood classification (MLC) is carried out for the comparison of the result of proposed building detection approach. This is done with fused image enabling the comparison of data integration techniques too. The fused image is classified with MLC in ERDAS IMAGINE 2010. This classification is carried out with the same classes defined for the soft classification. The classes are red roof building, blue roof building, white roof building, vegetation shadow, bare soil and road. The training data for each class is selected from the fused image by visual interpretation for each class. The classified image is filtered with sieve filter with 7 pixels as the smallest building in the study area is approximately 8 by 8 meters. Then the building footprints are identified the visual variable colour. Then the building map is used for the validation and comparison

### 5.8. Validation and comparison

The validation is done in two ways namely pixel based validation and object based validation. The pixel based validation of the result is carried out using the conventional confusion matrix of the classification. The omission, commission errors and kappa coefficient are used for the accuracy assessment and comparison. This pixel based accuracy assessment is done for both SRM classification and MLC classification. This is carried out with the reference map prepared from screen print of Google Earth for the SRM. The pixel based accuracy assessment is done with stratified random point sampling procedure for the MLC classification as it is difficult to collect the ground truth as a point file and stratified random sampling generates the equal number of samples for all classes. The number of properly detected buildings is also counted in each building map for the object based validation.

The object based validation is carried out in the manner of topological and geometric accuracy quantities described in Clinton et al., (2008) and Tolpekin et al., (2010). The under identification and over identification given in the equation 5.1 and 5.2 (Tolpekin et al., 2010) are used to measure the topological accuracy of the building map with respect to the reference map while the total area index given in equation 5.3 is applied to determine the geometrical accuracy of the buildings. These accuracy measures are applied to three results obtained from SRM and MLC building detection.

$$O_{id} = 1 - \frac{\sum_{i=1}^n \text{area}(O_i \cap R_i)}{\sum \text{area}(O_i)} \quad (5.1)$$

$$U_{id} = 1 - \frac{\sum_{i=1}^n \text{area}(O_i \cap R_i)}{\sum \text{area}(R_i)} \quad (5.2)$$

$$TE = \sqrt{O_{id}^2 + U_{id}^2} \quad (5.3)$$

Where  $O_{id}$  is the over identification,  $U_{id}$  is the under identification and  $TE$  is the total error.  $O_{id}$  is the  $i^{\text{th}}$  classified building and  $R_i$  is the  $i^{\text{th}}$  reference building. The possible value for over identification and under identification is in the range of zero to one. The value closer to zero means that there is a good match between the identified buildings and reference buildings. The value closer to one means a large difference in area between reference buildings and the identified buildings. The value range for the total error is between 0 and  $\sqrt{2}$ . The total error should be closer to zero for better topological match between the identified buildings and the reference buildings.

After the calculation of both accuracy measures, the comparison of methods is carried out to answer the research questions. The SRM based building detection method is compared with the MLC method to determine the most suitable technique for building footprint detection. The suitability of the method is determined on the basis of values of those accuracy measures and the building detection with the SA optimization and ICM optimization is compared to determine the accurate optimization for building detection from high resolution satellite images. Finally the result from the MS image is compared with that of fused image to identify suitable data integration for image classification in building footprint detection.

## 5.9. Summary

This chapter mainly focused on the proposed building detection approach. First it described the overall procedure in the building detection approach. Then the each step in the new approach has described. It included soft classification of MS image, initial SRM generation, optimization of SRM with SA and ICM, building detection. Then the building detection with MLC and the validation and comparison of the results obtained with proposed method with MLC method were described. The result of these steps will be described in Chapter 6.

## 6. RESULTS

### 6.1. Parameter estimation of the Super Resolution Mapping

The parameter estimation is the crucial step in the super resolution mapping as it is tedious and time consuming task. Therefore the parameter estimation is carried out using the tuning image. The ASCII format of the tuning image is used as it is compatible with R software. Then the parameter estimation is carried out in R software based on the minimum energy and the maximum kappa value of the SRM as atrial and error procedure. The results of the estimation of annealing parameters and smoothing parameters are given in the proceeding sections.

### 6.2. Simulated Annealing parameters estimation

The SA parameters  $T_0$  and  $T_{upd}$  are first estimated using the kappa and energy values and their standard deviations of the optimized SRM obtained from different values of initial temperature and updating rate. The estimation is carried out by varying one parameter at a time while keeping the other parameters constant. Each experiment is repeated 10 times. Then the kappa and the total energy were averaged over 10 observations and plotted against the initial temperature values for the estimation of optimum values of two parameters. The standard deviation of kappa and energy is also calculated and plotted identify the optimum value with smaller standard deviation. The optimum initial temperature determination is done by fixing  $T_{upd} = 0.1$ , window size = 3,  $\lambda = 0.8$ , and  $\lambda_p = 0.3$ . The statistics of the kappa values are given in Table 6.1 and the graphs in Figure 6.1 and those of the total energy are given in the Table 6.2 and Figure 6.2.

Table 6.1: Statistics of kappa values with initial temperature ( $T_0$ ) for window size 3

$T_0$	$T_{upd}$	$\lambda$	$\lambda_p$	Minimum Kappa	Maximum Kappa	Mean kappa	Standard deviation
1	0.1	0.8	0.3	0.601	0.623	0.611	0.006
2	0.1	0.8	0.3	0.608	0.630	0.618	0.007
3	0.1	0.8	0.3	0.613	0.627	0.620	0.005
4	0.1	0.8	0.3	0.605	0.636	0.618	0.012
5	0.1	0.8	0.3	0.612	0.638	0.625	0.008
6	0.1	0.8	0.3	0.600	0.640	0.621	0.011
7	0.1	0.8	0.3	0.598	0.628	0.616	0.009
8	0.1	0.8	0.3	0.595	0.629	0.615	0.012
9	0.1	0.8	0.3	0.604	0.629	0.618	0.009

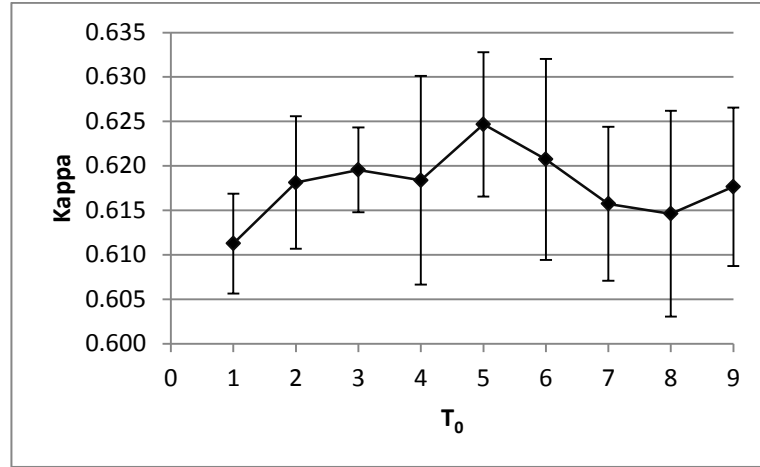
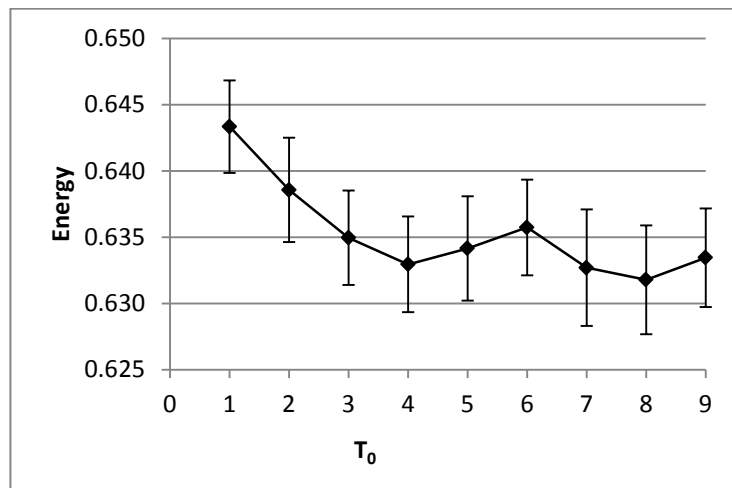

 Figure 6.1: Mean kappa of SRM versus initial temperature ( $T_0$ ) with standard deviation in error bars

 Table 6.2: Statistics of energy values versus initial temperature ( $T_0$ )

$T_0$	$T_{\text{upd}}$	$\lambda$	$\lambda\rho$	Minimum Energy	Maximum energy	Mean Energy	Standard deviation
1	0.1	0.8	0.3	0.636	0.648	0.643	0.003
2	0.1	0.8	0.3	0.633	0.645	0.639	0.004
3	0.1	0.8	0.3	0.629	0.640	0.635	0.004
4	0.1	0.8	0.3	0.628	0.640	0.633	0.004
5	0.1	0.8	0.3	0.627	0.640	0.634	0.004
6	0.1	0.8	0.3	0.631	0.643	0.636	0.004
7	0.1	0.8	0.3	0.628	0.641	0.633	0.004
8	0.1	0.8	0.3	0.623	0.638	0.632	0.004
9	0.1	0.8	0.3	0.628	0.639	0.633	0.004


 Figure 6.2: Mean energy versus initial temperature ( $T_0$ ) with standard deviation in error bars

According to the graphs above the kappa of the SRM is optimal at initial temperature values 5 and the energy is minimal at the initial temperature values 4 and 8. The minimum standard deviation of the energy is at initial temperature 1 compared to other values. As the initial temperature is directly related to the energy optimization the more consideration is paid on the energy distribution. The mean energy is minimum at 4 but the standard deviation is high and standard deviation is minimum at 1. Therefore the initial temperature is taken as 1 because the standard deviation is less and it will help to produce a less noisy SRM. The optimal initial temperature of this experiment is also agreed with the previous work done by Tolpekin et al., (2010). Tolpekin et al., (2010) applied the initial temperature value 1 for the urban tree crown extraction. Therefore the value 1 is reliable to be set as initial temperature value for this experiment based on the experimental results.

### 6.3. Determination of temperature updating rate

The experiment is carried out 10 times for each updating value keeping the smoothing parameters and initial temperature constant ( $T_0 = 1$ ,  $w_s = 3$ ,  $\lambda = 0.8$  and  $\lambda_p = 0.3$ ). The mean kappa and the mean energy are plotted against the temperature updating rate values ranging from 0.1 to 0.9. The mean kappa of the experiment is shown in Table 6.3 and graphs 6.3.

Table 6.3: Statistics of kappa values versus temperature updating rate

$T_0$	$T_{upd}$	$\lambda$	$\lambda_p$	Minimum Kappa	Maximum Kappa	Mean kappa	Standard deviation
1	0.1	0.8	0.3	0.602	0.618	0.609	0.006
1	0.2	0.8	0.3	0.605	0.623	0.614	0.005
1	0.3	0.8	0.3	0.607	0.628	0.617	0.007
1	0.4	0.8	0.3	0.603	0.629	0.615	0.010
1	0.5	0.8	0.3	0.612	0.633	0.621	0.008
1	0.6	0.8	0.3	0.611	0.632	0.620	0.007
1	0.7	0.8	0.3	0.603	0.625	0.615	0.008
1	0.8	0.8	0.3	0.590	0.627	0.609	0.011
1	0.9	0.8	0.3	0.605	0.628	0.612	0.007

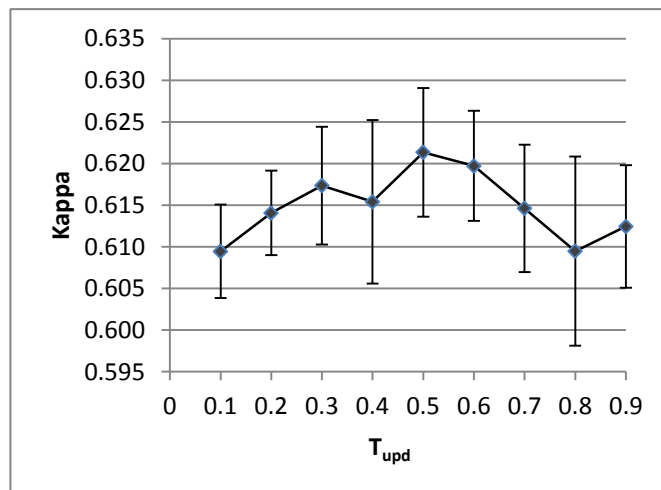


Figure 6.3: Mean kappa versus Temperature updating rate ( $T_{upd}$ ) with standard deviation in error bars

According to the kappa values of the SRM shown in Table 6.3 and Figure 6.3 above the temperature updating rate is optimum at 0.2 with smaller standard deviation compared to other values. Therefore the temperature updating rate was selected as 0.2 to obtain less noisy SRM.

#### 6.4. Determination of smoothing parameters ( $\lambda$ and $\lambda_p$ )

By fixing the initial temperature, the temperature updating rate and window size ( $T_0 = 1$  and  $T_{upd} = 0.2$  and  $ws = 3$ ) the experiment is carried out ten times with different smoothing parameters ranging from 0.6 to 0.9 for panchromatic smoothing parameter range 0 to 0.8. The results of the experiment are given in Table D1 in Appendix D and the graphs 6.4 and 6.5.

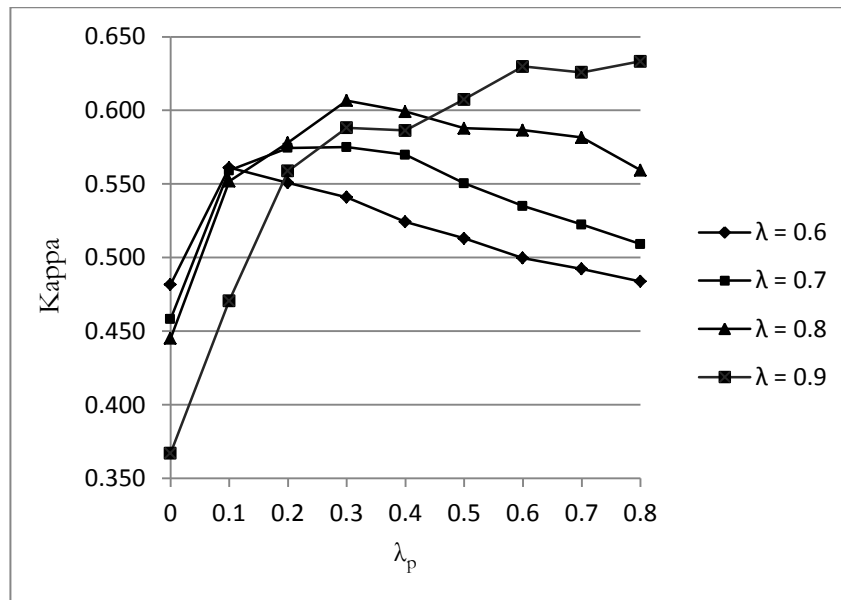


Figure 6.4: The mean kappa of the optimized SRM versus panchromatic smoothing parameters ( $\lambda_p$ ) for different smoothing parameters ( $\lambda$ )

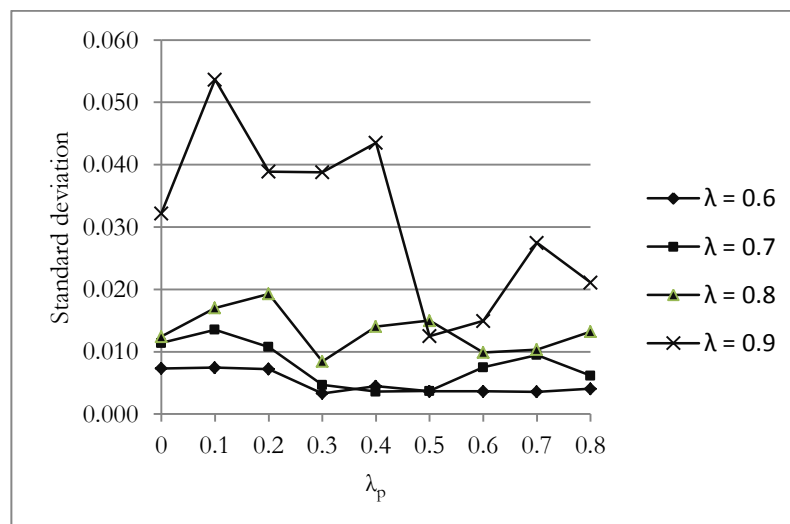


Figure 6.5: The standard deviation of the optimized SRM versus panchromatic smoothing parameters ( $\lambda_p$ ) for different smoothing parameters ( $\lambda$ )

According to Figure 6.4 of the smoothing parameters ( $\lambda$  and  $\lambda_p$ ) the optimal values for the smoothing parameter between prior and likelihood energy is 0.8 and the smoothing parameter between likelihood energy of panchromatic image and MS image is 0.3. At those values the kappa of the optimized SRM is high with smaller standard deviation compared to other values (see Figure 6.5). The kappa of the SRM increase with  $\lambda = 0.9$  and  $\lambda_p = 0.6$  but the standard deviation is high. Therefore the smoothing parameters are selected as  $\lambda = 0.8$  and  $\lambda_p = 0.3$  for less noisy optimized SR map. These parameters of the energy model also agree with the class separability values calculated in Section 4.5. The class separability (ID) values shows that the classes are poor separable in panchromatic image and well separable in MS image. This agrees with the less likelihood energy contribution from the panchromatic image.

### 6.5. Estimation of window size

Then the experiment was carried out for the determination of optimum window size fixing the annealing and smoothing parameters ( $T_0 = 1$ ,  $T_{\text{upd}} = 0.2$ ,  $\lambda = 0.8$  and  $\lambda_p = 0.3$ ). The obtained results are shown in Table 6.4 and Figure 6.6.

Table 6.4: Statistics of kappa values for different window sizes

Window size (ws)	Minimum Kappa	Maximum Kappa	Mean Kappa	SD
1	0.510	0.554	0.529	0.01
2	0.520	0.586	0.544	0.02
3	0.521	0.573	0.552	0.02
4	0.528	0.552	0.538	0.008
5	0.499	0.552	0.526	0.02
7	0.491	0.529	0.517	0.01

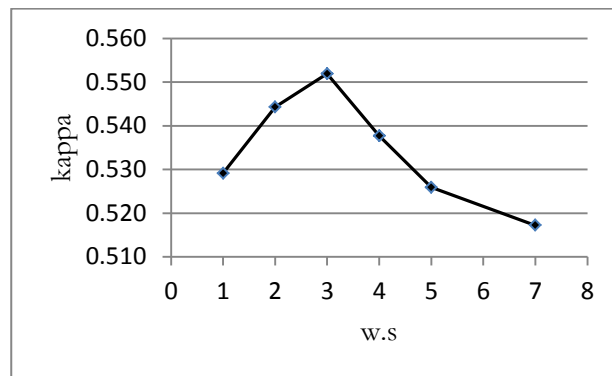


Figure 6.6: Mean kappa versus window size (w.s)

The experiment results show that kappa value is higher at the window size 3 ( $ws = 3$ ) (see Figure 6.6). The neighbouring system is defined with the window size in the software as twice the window size plus one ( $2ws + 1$ ). The window size 3 defines a 7 by 7 neighbouring system in the image. This neighbourhood size is almost similar to the size of the small buildings in the study area. The window size 3 results maximum kappa value of the optimized SRM. Therefore the window size 3 was selected as it results the optimum SRM. Now all the parameters of the energy model have been determined. Those are shown in Table 6.5.

Table 6.5: Parameters of the energy model and SA

Parameter	Value
Prior and likelihood energy smoothing parameter ( $\lambda$ )	0.8
Likelihood energy smoothing parameter ( $\lambda_p$ )	0.3
Initial temperature ( $T_0$ )	1.0
Temperature updating rate ( $T_{upd}$ )	0.2
Window size	3

The smoothing parameter estimation was cross checked with the automated parameter estimation algorithm developed by Eshete, (2011). This was carried out using the scale factor and the transform divergence values of all classes selected for this study. This algorithm has two adjustment factors for the smoothing parameter  $\lambda$  and  $\lambda_p$ . The automatic estimated parameter values are  $\lambda = 0.998$  and  $\lambda_p = 0.302$ . The parameter  $\lambda_p$  well agreed with that value of this study.

### 6.6. Effect of the SA and annealing parameters on the colour of the roof and the size of the buildings

The effect of the parameters on the roof colour and the size of the building were studied by selecting a subset image with three type of buildings class and three sizes namely smaller medium and large. The results are given in Table 6.6 and the optimized SR maps are shown in Appendix E.

Table 6.6: Number of building detected according to the roof colour and size

Map	Red	Blue	White	Total	Small	Medium	Large	Total	
Reference	18	8	5	31	26	4	1	31	
Parameters		Number of building detected				Number of building detected			
$T_0$	$T_{upd}$	Red	Blue	White	Total	Small	Medium	Large	Total
1	0.1	18	8	4	30	25	4	1	30
2	0.1	18	8	3	29	24	4	1	29
3	0.1	18	8	3	29	24	4	1	29
4	0.1	18	8	2	28	23	4	1	28
5	0.1	18	8	3	29	24	4	1	29
6	0.1	18	8	3	29	24	4	1	29
7	0.1	18	8	3	29	24	4	1	29
8	0.1	18	8	3	29	24	4	1	29
9	0.1	18	8	3	29	24	4	1	29
1	0.1	18	8	3	29	24	4	1	29
1	0.2	18	8	3	29	24	4	1	29
1	0.3	18	8	3	29	24	4	1	29
1	0.4	18	8	3	29	24	4	1	29
1	0.5	18	8	3	29	24	4	1	29
1	0.6	18	8	3	29	24	4	1	29
1	0.7	18	8	3	29	24	4	1	29
1	0.8	18	8	3	29	24	4	1	29
1	0.9	18	8	3	29	24	4	1	29
$\lambda$	$\lambda_p$	Red	Blue	White	Total	Small	Medium	Large	Total
0.8	0	18	8	5	31	26	4	1	31
	0.1	18	8	4	30	25	4	1	30

	0.2	18	8	4	30	25	4	1	30
	0.3	18	8	3	29	24	4	1	29
	0.4	18	8	3	29	24	4	1	29
	0.5	18	8	3	29	24	4	1	29
	0.6	18	8	3	29	24	4	1	29
	0.7	18	8	3	29	24	4	1	29
	0.8	18	8	2	28	23	4	1	28
	0.9	18	8	0	26	22	4	0	26
0.9	0	17	7	4	28	23	4	1	28
	0.1	17	7	3	27	23	4	1	28
	0.2	17	7	3	27	22	4	1	27
	0.3	17	7	3	27	22	4	1	27
	0.4	17	8	3	28	23	4	1	28
	0.5	17	8	3	28	23	4	1	28
	0.6	17	8	3	28	23	4	1	28
	0.7	18	8	3	29	24	4	1	29
	0.8	18	8	3	29	24	4	1	29
	0.9	18	8	3	29	24	4	1	29

### 6.7. Optimized SRM

Using the smoothing and the annealing parameters determined previous section the initial SRM is optimized with the SA and ICM algorithms in R software. Then the clumping is applied to the optimized SR maps to group the pixels and they are cleaned with sieve filter to remove isolated pixels and patches. Then those are visualized in the Arc Map software to obtain the building footprint map. The visualized building footprint maps are shown in Figure 6.7. According to the visual interpretation of optimized SR maps the shape and size of the buildings are preserved quite well. The building objects can be identified. The buildings which are very closer to each other have been detected as a group of buildings. The buildings which are separated with a distance around 4m have identified as individual buildings. The false identification is less. The blue roof buildings are confused with the shadow class. This is because of the poor separability of these two classes in panchromatic image.

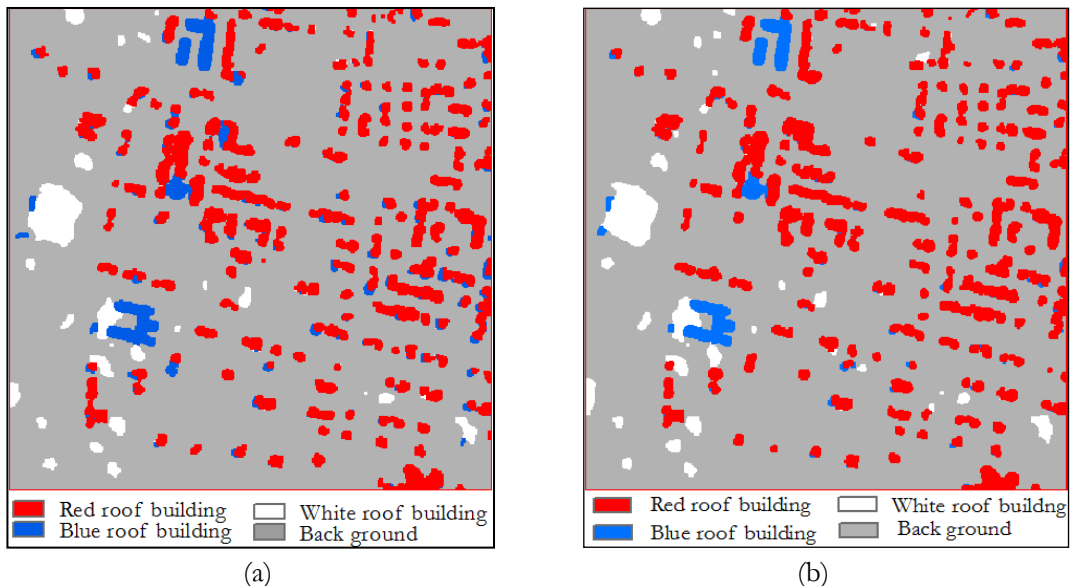


Figure 6.7: Building footprint map from MRF based SRM optimized with SA (a) and ICM (b)

### 6.8. Building footprint detection with MLC

The HPF fused image and MS image are classified with MLC to detect the building footprints. The classified thematic maps are clumped and then cleaned with sieve filter to obtain the building footprint map. The visualized building maps are shown in Figure 6.8. According to the visual interpretation of these maps it is very difficult to identify the building in MLC classified map and in the fused image map the ability to identify the building is less than the SR maps. The false detection in fused and MS image maps is more than that in the SR building maps. The shape and size of the buildings are not preserved less than the SR maps.

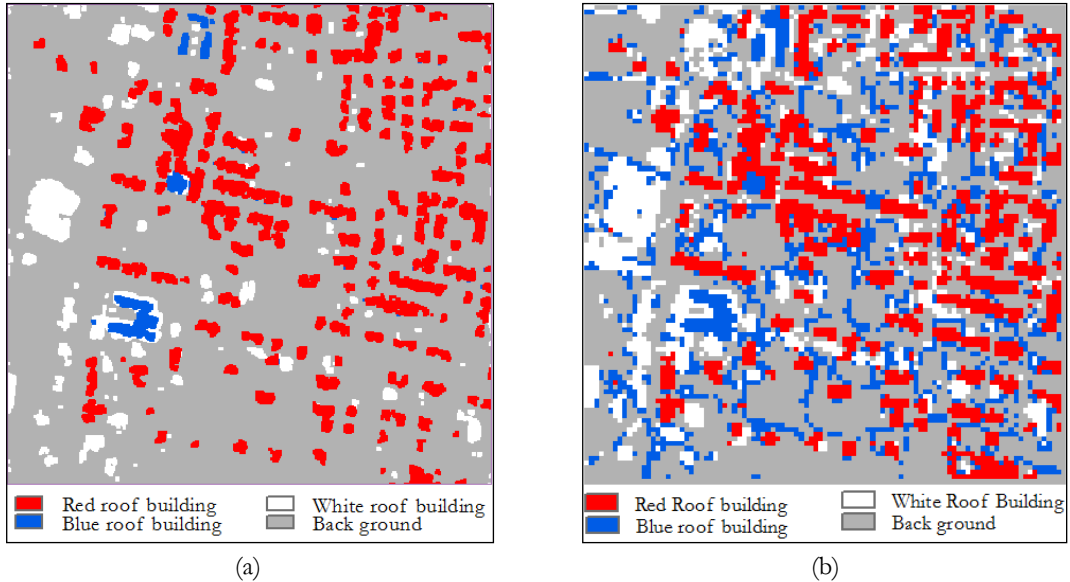


Figure 6.8: Building footprint map from (a) MLC with fused image (b) MLC with MS image

### 6.9. Validation and comparison

The pixel based accuracy of the building footprint map is carried out with confusion matrix and kappa coefficient. The confusion matrix for SRM building maps are calculated for building class and back ground class in R software and for the other two maps kappa is calculated for all classes used for the classification in ERDAS IMAGINE 2010 software. The confusion matrix for each building footprint map is given in Table 6.7, 6.8, 6.9 and 6.10. The kappa coefficient of each map is given in Table 6.11. According to the confusion matrixes the overall accuracies of SR maps are 87% and that of fused and MS image maps are 62% and 53% respectively.

Table 6.7: The confusion matrix of building footprint map from SRM optimized with SA

Thematic map classes	Reference classes				
	Building	Back ground	Total pixel	commission	User accuracy
Building	20988	9770	30758	0.3176	68%
Back ground	11308	117934	129242	0.0875	91%
Total pixel	32296	127704	160000		
Error of omission	0.3501	0.0765			
Producer accuracy	65%	92%	Over all classification accuracy = 87%		

Table 6.8: The confusion matrix of building footprint map from SRM optimized with ICM

Thematic map Classes	Reference class				
	Building	Back ground	Total pixel	commission	User accuracy
Building	20635	9237	29872	0.3092	69%
Back ground	11661	118467	130128	0.0896	91%
Total pixel	32296	127704	160000		
Error of omission	0.3611	0.0723			
Producer accuracy	64%	93%	Over all classification accuracy = 87%		

Table 6.9: The confusion matrix of building footprint map from HPF fused image

Class Name	Reference Total	Classified Totals	Number Correct	Producers Accuracy	Users Accuracy
Red roof building	26	41	20	76.92%	48.78%
Blue roof building	12	10	8	66.67%	80.00%
White roof building	8	21	5	62.50%	23.81%
Vegetation	58	54	46	79.31%	85.19%
Shadow	16	39	5	31.25%	12.82%
Other	136	91	75	55.15%	82.42%
Total	256	256	159		
Over all classification accuracy					62.11%

Table 6.10: The confusion matrix of building footprint map from MS image

Class Name	Reference Total	Classified Totals	Number Correct	Producers Accuracy	Users Accuracy
Red roof building	33	50	27	81.82%	54.00%
Blue roof building	2	40	2	100.00%	5.00%
White roof building	9	35	5	55.56%	14.29%
Vegetation	70	74	50	71.43%	67.57%
Other	142	57	51	35.92%	89.47%
Total	256	256	135		
Over all classification accuracy					52.73%

Table 6.11: Kappa coefficient of each building footprint map

Building footprint map	Kappa
Building footprint map from SRM with SA	0.584
Building footprint map from SRM with ICM	0.581
Building footprint map from MLC with fused image	0.483
Building footprint map from MLC with MS image	0.383

The visual comparison of the building footprint maps was done by overlaying the reference map on each building footprint map. The overlay maps are shown in Figure 6.10 and 6.11. The overall number of detected buildings is also visually assessed with reference to the number of buildings in the reference. The

result of that assessment is given in Table 6.12. As the shape and size of the objects in building maps from fused image and MS image are not preserved compared to SR maps and the false detection is more in those map the building counting was not done. The shape and size of the detected buildings are visually compared and shown in Figure 6.9.

)

Table 6.12: Percentage of building detection in SR maps

Method	No of building detected	Total buildings in reference	Percentage
SRM from SA	276	292	95%
SRM from ICM	278	292	95%

Table 6.13: Results of object based accuracy assessment for each building footprint map

SRM from SA	Total area of the buildings in reference image ( R )	21877.60
	Total area of the buildings in optimized SRM with SA (O)	29832.00
	Intersected area ( $R \cap O$ )	16834.51
	Over identification	0.436
	Under identification	0.230
	Total error	0.493
SRM from ICM	Total area of the buildings in reference image ( R )	21877.60
	Total area of the buildings in optimized SRM with ICM (O)	28640.30
	Intersected area ( $R \cap O$ )	16626.10
	Over identification	0.419
	Under identification	0.240
	Total error	0.483
MLC Fused	Total area of the buildings in reference image ( R )	21877.60
	Total area of the buildings in MLC (O)	36347.30
	Intersected area ( $R \cap O$ )	16362.98
	Over identification	0.550
	Under identification	0.252
	Total error	0.605
MLC MS	Total area of the buildings in reference image ( R )	21877.6
	Total area of the buildings in MLC (O)	76934.23
	Intersected area ( $R \cap O$ )	19288.83
	Over identification	0.749
	Under identification	0.118
	Total error	0.759

The object based accuracy assessment of the building footprint maps is done according to the method described in Section 5.3. The results are given in Table 6.13 for each building footprint map separately. According to the result of object area based accuracy measures total error of SR maps from SA and ICM are 0.493 and 0.483 respectively and those for building maps from fused image and MS image are 0.605

and 0.759 respectively. This implies that more false detections are in the building maps from fused image and MS image.

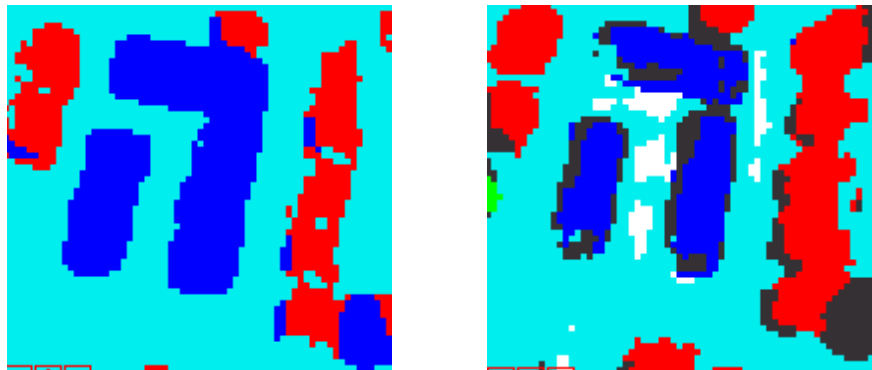


Figure 6.9: Shape and size of detected buildings from SRM (left) and MLC with fused image (right)

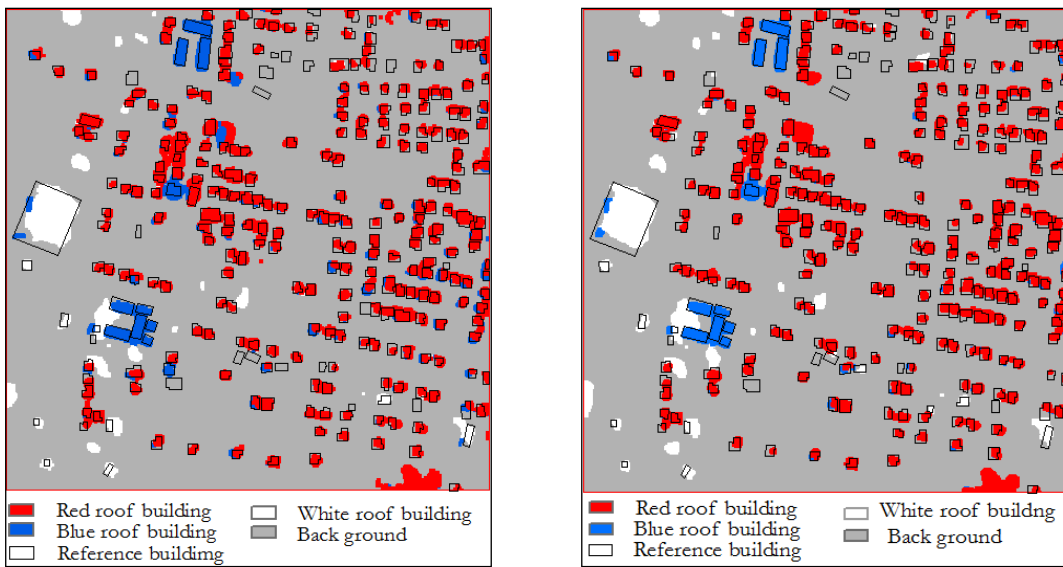


Figure 6.10: Overlay of reference map on SRM building footprint map

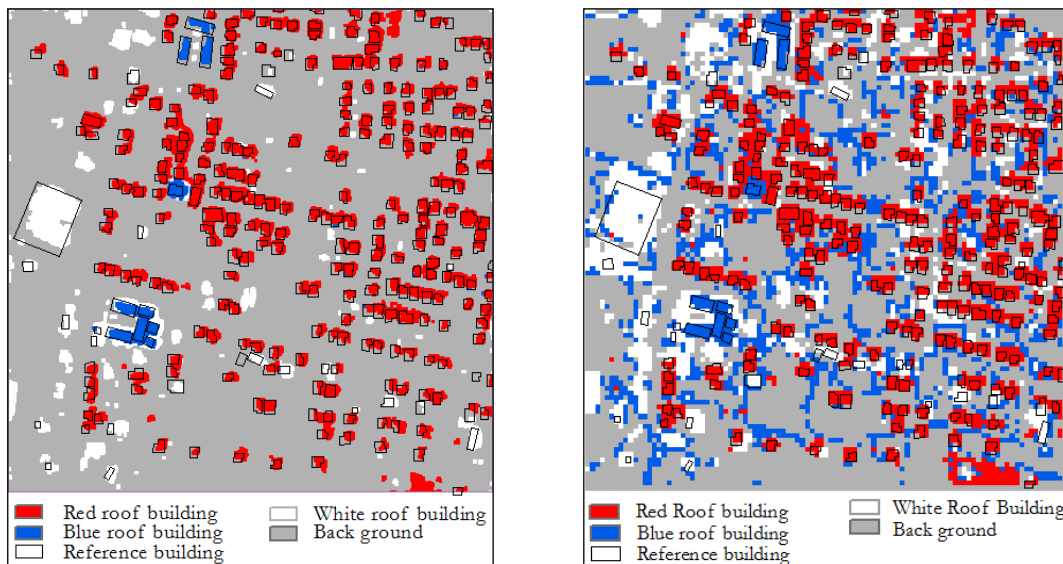


Figure 6.11: Overlay of reference map on building footprint map from MLC



## 7. DISCUSSION

In this study the building footprint detection is based on the integration of spatial and spectral data of remote sensing images with relatively high spatial resolution. The strengths, weaknesses, opportunities and threats in the proposed building footprint detection approach are discussed in detail in the following sections.

### 7.1. Strength of the proposed building detection approach

The proposed approach detects the building footprint more accurately than the MLC hard classification method; it identified most of the buildings. The shape of the buildings is preserved better than with the MLC method. The total number of buildings in the study area is 292. Out of 292 buildings 276 buildings or 95% are identified in both SA and ICM optimized SR maps. MRF based SRM shows less false identification of the buildings compared to the conventional MLC building identification. According to the result in Table 6.6, the detection of large and medium buildings size is more accurate than the smaller buildings using the developed method while the red roof buildings are more sensitive to this method compared to blue and white roof buildings. Another strength this that this method identified the building object automatically. The operator involvement is only for the parameter estimation. Even that can also be done automatically using an automatic parameter estimation algorithm. As this method is implemented in R which is an open source software even the developing countries can apply the method for their application.

### 7.2. Weakness of the approach

Though the developed method detects the buildings better than the conventional MLC building detection it also has some limitations. The parameter estimation of this method is crucial for the success of the building objects identification. That is tedious and time consuming task as it involves the iterative process and use of simulated annealing algorithm. The implementation of the developed method is carried out in R software in MS Windows operating system and it needs the higher performance computer. Another weakness of this method is that the method is computationally time intensive as MRF based SRM involves many mathematical computation such as neighbouring system generation, energy calculation and energy optimization. The spectral confusion between the blue roof building and the shade is also a weakness of this method as the shade of the building has detected as the blue roof buildings. That affects the accuracy of the building identification. However this depends on the area of the building footprint detection. It would not be a problem in an area without blue buildings. The few smaller buildings of the study area were not detected by this method and it is agreed with our expectation as SRM is sensitive to the size of the building object. That is because of the poor prior energy of the pixels of the smaller building as they have fewer building pixels in the neighbouring system. As the larger buildings provide more pixels for the energy calculation the larger and medium buildings are more sensitive to the developed method.

The developed method is based on few assumptions which might have limited the accuracy in the pixel based and object based accuracy assessment. The first assumption is that the spectral properties of the specific building class are same for the all building in that class. But it is not like that in reality as the spectral properties of the individual buildings are slightly different from each other according to the intensity of the reflectance of the object. The intensity of the reflectance varies with the material of the roof and the surface roughness of the building roof. So the same roof colour buildings can have different spectral property. We also assume that the sensitivity of the panchromatic band is the average of the four

bands of the MS image in energy modelling. The panchromatic band is sensitive to the wave length range from 500 nm to 900 nm and the sensitivity is maximum at the middle of the range according to the sensor spectral response function, but the four bands of the MS image do not cover the entire range of the panchromatic band. This has a negative effect on the energy calculation as it assume that the radiation received to the sensor at pixel location in panchromatic image corresponds to that in the assumed MS image (see Equation 3.11). Then we assume that the spatial distribution of the received energy within the pixel is uniform in the entire pixel (see Equation 3.10) and calculated energy by averaging four finer resolution pixels on one coarser resolution pixel. That is also not true in reality as energy is distributed according to the point spread function. In this approach the spectral classes were limited to few classes for computational convenience. It is not like that in reality as there are many classes spectrally different from each other for example we assume that the spectral property of the shadow class is same for all shadows but the shadow from different part of the image varies according to the darkness of the shade. Those factors are the weakness of the developed building detection approach and that leads to the less accuracy of the obtained results. As the MRF based SRM is directly related to the spatial dependency this approach would not be success for the dense city areas and the urban areas. As this method is sensitive to the finer resolution images this approach is not recommended for the courser resolution images like ASTER and SPOT.

### **7.3. Opportunities for improvement**

As discussed in the previous this method has some weaknesses but there are some opportunities to overcome those and to refine the output for more convenience and efficiency. The parameter estimation of the method is tedious and time consuming. That can be overcome with automated parameter estimation. The automated parameter estimation developed by Eshete, (2011) can be applied to determine the smoothing parameters for this method too. That will solve half of the parameter estimation as additional simulated annealing parameter estimation is also needed. Next, the computationally intensive procedure is a disadvantage due to the speed of the present computer system. Faster computer systems are introducing with the daily development of the computer technology so the computational time will not be a problem for the implementation of this method. The software for this method is implemented in R which is also the reason for the time consumption. This can be overcome using code in C++ programming language which is 20 times faster than R. The spectral property of the blue roof building is confused with that of the shade in this implementation. So it is better to think of spectrally sensitive methods to extract the training data for each building class. As the blue roof buildings are not very common in every where it is not a big problem for the implementation of this method. With the above suggestion the limitations of the developed building detection methods can be minimized.

### **7.4. Threats to the proposed building detection approach**

The detection of the smaller building is one of the threats for this method as the MRF based SRM is less sensitive to the smaller buildings. This method was tested with relatively coarser resolution satellite image (4m). The MRF based SRM tool was applied to the detection of urban tree crown by Tolpekin et al., (2010) with 2.4m finer resolution Quickbird image. That is why the testing of building footprint detection method showed high over identification and high total error in object based accuracy assessment. Another threat of this study is that the accuracy of this method is directly related to the class definition. The classes should be defined with better spectral separation. In reality that is very difficult task as the reflectance of surface materials of different objects has some overlap with others. This is a main threat for the implementation of this method.

## 8. CONCLUSIONS AND RECOMMENDATIONS

The building footprint detection from high resolution image is an important aspect in the remote sensing application. The building footprints have been identified from different techniques with integration of various data sources. In this study the integration of spectral and spatial data of high resolution satellite images has been applied for the detection of building footprint. The integration is done with the SRM based MRF technique. This method has been compared with the conventional pan-sharpening data integration techniques. The validation of the new building footprint detection methods has been done in two ways namely pixel based accuracy assessment and object based accuracy assessment. The object based accuracy assessment was selected for validation as it compares the topological and geometrical accuracy of the detected buildings with the reference buildings. In other words, it allows user to understand how well the detected building footprint map fits topologically and geometrically with the reference buildings. To achieve the objective of the research five research questions posed and those are answered in the following section.

### 8.1. Conclusions

The conclusions of this study are drawn by answering the each research questions posed to achieve the research objectives.

1. Which energy optimization method is more suitable to obtain the most accurate result from MRF based SRM: Simulated Annealing (SA) or Iterated Conditional Modes (ICM)?

The initial SRM was optimized with SA and ICM separately. The results of both are shown in Table 6.10. The kappa coefficients of both optimization methods are almost equal. The kappa of SRM optimized from SA is 0.584 while that from ICM is 0.581. The object based accuracy measures shows that total error of SA optimization is 0.493 and that of ICM optimization is 0.483. So the pixel based accuracy shows that SA optimization is better than the ICM optimization while the object based accuracy shows that the ICM optimization is better than the SA optimization. However there is no significant difference in the values of those measures. The confusion matrix shows 87% overall accuracy for both SRM from SA and ICM and also other measures like user accuracy, producer accuracy, omission and commission error are almost the same for both optimizations. Therefore according to the results obtained from this research both optimization techniques result in almost similar SRM as there is no significant difference in accuracy measures. It can be concluded that both optimization techniques; SA and ICM; are equally suitable for the energy optimization in MRF based SRM to obtain the SR map.

2. How do the simulated annealing parameters affect the accuracy of MRF based SRM result in building footprint detection?

The accuracy of the SRM was measured with the kappa coefficient. The variation of kappa value with the initial temperature is shown in Figure 6.1. According to the figure, the kappa value increases with the increase of initial temperature up to 1 and then it decreases. The kappa value is at maximum at initial temperature value 5. However there is no direct relation between the accuracy of the optimized SRM and the initial temperature in building footprint detection. The change of the kappa coefficient with the temperature updating rate is shown in the Figure 6.3. The kappa value of the optimized SRM increases up

to the updating rate 0.5 then it decreases. The kappa value is at maximum at the temperature updating rate 0.5. The shape of the change in kappa value with initial temperature and the updating rate is similar. From both graphs it is clear that the simulated annealing parameters affect the accuracy of the optimized SRM but there is no direct relation between the accuracy of the SRM and the annealing parameters.

3. Which accuracy measure is more suitable for the accuracy assessment of building footprint detection from VHR MS and panchromatic images: object based or pixel based accuracy measure?

The accuracy assessment of this study is carried out in pixel based and an object based way. The pixel based accuracy shows the ratio between the correctly identified pixels and total pixels. It does not give any idea about geometrical accuracy of the identified building footprints or how the detected building footprints match with the building footprint in reference map. The object based accuracy measures show the topological and geometrical accuracy measures. The topological accuracy measures gives the over identification and under identification of the detected building footprints with respect to the reference building footprint map and the total error shows the geometrical correctness of the identified building footprint. The geometrical accuracy measure gives how the detected buildings fit with the reference buildings. If the total error is very close to zero the detected buildings fit properly with the reference buildings on a one to one basis. The results of this study shows that the buildings detected from MRF based SRM fit with the buildings in reference map better than MLC method. So the object based accuracy measures are more meaningful than the pixel based accuracy measures for the user's aspect as users need to know how the detected building footprint map fit with the reality.

4. Is SRM based building footprint detection technique with MS and panchromatic image more accurate than the MLC based building footprint detection technique from fused image?

The building footprint detection from SRM with MS and panchromatic image was carried out. The pixel based accuracy showed 0.584 kappa values for the SA optimized SRM building detection and 0.581 kappa values for ICM optimized SRM based building detection. The kappa value is 0.483 for the MLC based building detection from fused image. So the SRM based building footprint detection shows higher accuracy than the MLC based building footprint detection. The object based accuracy measures also show higher values for the SRM based building detection. According to Table 6.12 the over identification, under identification and total error show that the SRM based building detection is more accurate than the MLC based building detection. The visual comparison of the buildings detected from SRM and MLC verify that the SRM preserve the shape of the buildings better than the MLC. Therefore it can be conclude that the SRM based building footprint detection techniques with integration of VHR MS and panchromatic image is more accurate than the MLC based building footprint detection from fused image.

## **8.2. Recommendations**

MRF based SRM is a potential tool for the object extraction from the high resolution satellite image. Based on the experiences from this study followings can be recommend for further research to carry out the object extraction from VHR images efficiently.

- a) The parameter estimation is the crucial and time consuming task in the MRF based SRM data integration. Those parameters vary from the data set to data set. And it is the main task in the SRM process. In this study the parameters were determined on the statistical basis and it was really time consuming. Therefore it is recommended to do the research for the automation of parameter estimation.

- b) The buildings in this study area are separated by around two to three meters distance and the finer resolution image and the SR map have 1m spatial resolution. As a result the individual buildings which are closer to each other have been identified as one building object in this study. Therefore further research is recommended for the identification of individual buildings using MRF based SRM data integration. The individual building detection from VHR images was not successful from this study as the separations between the buildings are about two to three meters. That separation is almost equal to the finer resolution pixel size which is the result of the scale factor. Therefore further research is recommended to find the appropriate scale factor that would result the finer resolution pixel.
  
- c) The reflectance property of the blue roof building is confused with that of the shade and it affect to the accuracy of the building detection. Therefore further research is recommended to study the separation of spectral properties from the building classes.

The reference map for this study was prepared from the Google Earth image. That is not the most optimal way for the preparation of a reference map as new buildings and extensions of the buildings have been constructed after the area has been imaged. It is better to use a high resolution digital areal or very high resolution satellite image with the same date of the Ms and panchromatic images to prepare the reference map to be consistent the number of buildings and the shape of the buildings in the study area.



---

## LIST OF REFERENCES

---

- Ahadzadeh, S., Valadanzouj, M., Sadeghian, S., & Ahmadi, S. (2008). Detection of damaged buildings after an earthquake using Artificial Neural Network Algorithm. *The International Archives of the Photogrammetry, Remote Sensing and Spatial Information Sciences XXXVII*.(369-372).
- Atkinson, P. M. (2004). Super-Resolution Land Cover Classification Using the Two-Point Histogram. In X. Sanchez-Vila, J. Carrera & J. Gómez-Hernández (Eds.), *geoENV IV — Geostatistics for Environmental Applications* (Vol. 13, pp. 15-28): Springer Netherlands.
- Atkinson, P. M., Cutler, M. E. J., & Lewis, H. (1997). Mapping sub-pixel proportional land cover with AVHRR imagery. *International journal of Remote Sensing*, 18(4), 917-935.
- Besag, J. (1986). On the Statistical Analysis of Dirty Pictures. *Journal of the Royal Statistical Society. Series B (Methodological)*, 48(3), 259-302.
- Bijker, W., & Sanjaya, H. (2008). Use of geographical information system for audit of disaster related aid : training report of the SAADRA program. Enschede, ITC, 2008, 74.
- Boucher, A. (2008). Super Resolution Mapping with Multiple Point Geostatistics. In A. Soares, M. J. Pereira & R. Dimitrakopoulos (Eds.), *geoENV VI – Geostatistics for Environmental Applications* (Vol. 15, pp. 297-305): Springer Netherlands.
- Chen, L. C., Teo, T. A., Shao, Y. C., Lai, Y. C., & Rau, J. Y. (2004). Fusion of LIDAR Data and Optical Imagery for Building Modeling. *International Archives of Photogrammetry and Remote Sensing*, 35, 732-737.
- Clinton, N., Holt, A., Gong, P., & Yan, L. (2008). An accuracy assessment measure for object based image segmentation. In: ISPRS (ed.), *ISPRS Congress Beijing 2008*, , XXXVII.
- Cracknell, A. P. (1998). Synergy in remote sensing - what's in a pixel? *International Journal of Remote Sensing*, 19(11), 2025 - 2047.
- Dobigeon, N., Moussaoui, S., Coulon, M., Tourneret, J. Y., & Hero, A. O. (2009). Joint Bayesian Endmember Extraction and Linear Unmixing for Hyperspectral Imagery. *Signal Processing, IEEE Transactions on*, 57(11), 4355-4368.
- Du, Y., Bijker, W., & Wang, C. (2009). Verification of post-tsunami housing reconstruction projects by object - oriented building extraction from from high resolution satellite imagery : abstract + poster. In: *ACRS 2009 : proceedings of the 30th Asian conference on remote sensing : geo - referenced images of capitals in Asia*. (18-23 October 2009, Beijing, China. - Wuhan: Wuhan University Press, 2009. ISBN 978-7-900673-48-0. 5p).
- Durieux, L., Lagabrielle, E., & Nelson, A. (2008). A method for monitoring building construction in urban sprawl areas using object-based analysis of Spot 5 images and existing GIS data. *ISPRS Journal of Photogrammetry and Remote Sensing*, 63(4), 399-408.
- Elshehaby, A., & Taha, L. (2009). A new expert system module for building detection in urban areas using spectral information and LIDAR data. *Applied Geomatics*, 1(4), 97-110.
- Eshete, A. L. (2011). Automatic parameter estimation in MRF based super resolution mapping. ITC, Enschede.
- Foody, G. M. (2006). Sub-Pixel Methods in Remote Sensing. In S. M. De Jong & F. D. Der Meer (Eds.), *Remote Sensing image analysis including the spatial domain* (pp. 37-49).
- Foody, G. M., & Mathur, A. (2006). The use of small training sets containing mixed pixels for accurate hard image classification: Training on mixed spectral responses for classification by a SVM. *Remote Sensing of Environment*, 103(2), 179-189.
- Gamba, P., Houshmand, B., & Sacconi, M. (2000). Detection and extraction of buildings from interferometric SAR data. *IEEE Transaction on geoscience and remote sensing* 38(1), 611-618.
- Geman, S., & Geman, D. (1984). Stochastic relaxation, Gibbs distributions, and the Bayesian restoration of images. *IEEE Transactions on pattern analysis and machine intelligence*, 6, 721-741.
- Genderen, J. L. V., & Pohl, C. (1994). Image fusion: Issues, techniques and applications. *Intelligent Image Fusion, Proceedings EARSeL Workshop, Strasbourg, France, 11 September 1994*, edited by J. L. van Genderen and V. Cappellini (Enschede: ITC), 18- 26.
- Genderen, J. L. V., & Pohl, C. (1998). Multisensor image fusion in remote sensing: concepts, methods and applications. *International journal of Remote Sensing*, 19(5), 823-854.
- Grava, C., Gacsadi, A., Gordan, C., Grava, A. M., & Gavrilut, I. (2007, 13-14 July 2007). Applications of the Iterated Conditional Modes Algorithm for Motion Estimation in Medical Image Sequences.

- Paper presented at the Signals, Circuits and Systems, 2007. ISSCS 2007. International Symposium on.
- GuGuo, T., & Yasuoka, Y. (2003). Snake-based approach for building extraction from high-resolution satellite images and height data in urban areas.
- Hajime, M., Yamazaki, F., & Matsuoka, M. (2001). Development of automated extraction method for building damage area based on maximum likelihood classifier. 8th International Conference on Structural Safety and Reliability.
- Hamid, E., & Lari, Z. (2007). Automatic extraction of building features from high resolution satellite images using artificial neural networks. ISPRS Commission VII, WG VII/2 & VII/7.
- Haris, K., Efstratiadis, S. N., Maglaveras, N., & Katsaggelos, A. K. (1998). Hybrid image segmentation using watersheds and fast region merging. *Image Processing, IEEE Transactions on*, 7(12), 1684-1699.
- Hay, G. J., & Castilla, G. (2008). Geographic Object-Based Image Analysis (GEOBIA): A new name for a new discipline. In T. Blaschke, S. Lang & G. J. Hay (Eds.), *Object-Based Image Analysis* (pp. 75-89): Springer Berlin Heidelberg.
- Huber, M., Schickler, W., Hinz, S., & Baumgartner, A. (2003, 22-23 May 2003). Fusion of LIDAR data and aerial imagery for automatic reconstruction of building surfaces. Paper presented at the Remote Sensing and Data Fusion over Urban Areas, 2003. 2nd GRSS/ISPRS Joint Workshop on.
- Jin, X., & Davis, C. H. (2005). Automated Building Extraction from High-Resolution Satellite Imagery in Urban Areas Using Structural, Contextual, and Spectral information. *EURASIP Journal on Applied Signal Processing*, 14, 2196-2206.
- Jixian Zhang. (2010). Multi-source remote sensing data fusion: status and trends. *International Journal of Image and Data Fusion*, 1(1), 5 - 24.
- Kasetkasem, T., Arora, M. K., & Varshney, P. K. (2005). Super-resolution land cover mapping using a Markov random field based approach. *Remote Sensing of Environment*, 96(3-4), 302-314.
- Kassaye, R. H. (2006). Suitability of Markov random field based method for super resolution land cover mapping. ITC, Enschede.
- Keshava, N. (2003). A Survey of Spectral Unmixing Algorithms. *Lincoln laboratory journal*, 14(1)(November 1, 2003), 55-78.
- Kim, T., & Muller, J. P. (1994). Automated building height extraction and building detection from high resolution aerial and space imagery. *IAPR Workshop on Machine Vision Applications*.
- Lau, B. T. (2006). Automatic Building Extraction from Satellite Imagery. *Engineering Letters*, 13(3).
- Leea, D. H., Seo, D. C., Song, J. H., Choi, M. J., & Lim, H. S. (2008). Summary of calibration and validation for KOMPSAT-2. *The International Archives of the Photogrammetry, Remote Sensing and Spatial Information Sciences*, XXXVII, 53-56.
- Liu, X. P., Li, X., & Zhang, X. H. (2010). Determining Class Proportions Within a Pixel Using a New Mixed-Label Analysis Method. [Article]. *Ieee Transactions on Geoscience and Remote Sensing*, 48(4), 1882-1891.
- Lucas, N. S., Shanmugam, S., & Barnsley, M. (2002). Sub-pixel habitat mapping of a costal dune ecosystem. *Applied Geography*, 22(3), 253-270.
- Mayunga, S. D., Zhanga, Y., & Colemana, D. J. (2005). Semi Automatic building extraction utilizing QuickBird imagery. *IAPRS*, XXXVI, 131-136.
- Nguyen, M. Q., Atkinson, P. M., & Lewis, H. G. (2005). Superresolution mapping using a Hopfield neural network with lidar data. *Geoscience and Remote Sensing Letters, IEEE*, 2(3), 366-370.
- Ortner, M., Descombes, X., & Zerubia, J. (2007). Building outline extraction from digital elevation models using marked point processes. *International Journal of Computer Vision*, 72(2), 107-132.
- Richards, J. A., & Xiuping, J. (2006). Remote sensing digital image analysis : an introduction Available from <http://books.google.com/books?hl=en&lr=&id=4PB5vhPBdJ4C&oi=fnd&pg=PA1>
- Rutzinger, M., Höfle, B., & Pfeifer, N. (2008). Object detection in airborne laser scanning data - an integrative approach on object-based image and point cloud analysis. In T. Blaschke, S. Lang & G. J. Hay (Eds.), *Object-Based Image Analysis* (pp. 645-662): Springer Berlin Heidelberg.
- San, K. D., & Turker, M. (2005). Automated building detection from high resolution satellite images. *IEEE Transaction on geoscience and remote sensing*, 617-622.
- San, K. D., & Turker, M. (2010). Building extraction from high resolution satellite images using Hough transform. *International Archives of the Photogrammetry, Remote Sensing and Spatial Information Science*, XXXVIII, 1063-1067.

- Scott, L. D., Jie Shan, & Bethel, J. S. (2003). Class-Guided Building Extraction from Ikonos Imagery. *Photogrammetric Engineering & Remote Sensing*, 69(February 2003), 143–150.
- Selim, S. Z., & Alsultan, K. (1991). A simulated annealing algorithm for the clustering problem. *Pattern Recognition*, 24(10), 1003-1008.
- Selvarajan, S., & Tat, C. W. (2001). Extraction of man made features from Remote sensing images by data fusion techniques. Paper presented at the 22 nd Asian Conference on Remote Sensing.
- Sohn, G., & Dowman, I. (2007). Data fusion of high-resolution satellite imagery and LiDAR data for automatic building extraction. *ISPRS Journal of Photogrammetry and Remote Sensing*, 62(1), 43-63.
- Solberg, A. H. S., Taxt, T., & Jain, A. K. (1996). A Markov random field model for classification of multisource satellite imagery. *Geoscience and Remote Sensing, IEEE Transactions on*, 34(1), 100-113.
- Thurmond, A. K., Abdelsalam, M. G., & Thurmond, J. B. (2006). Optical-radar-DEM remote sensing data integration for geological mapping in the Afar Depression, Ethiopia. *Journal of African Earth Sciences*, 44(2), 119-134.
- Tolpekin, V. A., Ardila J. P., & Bijker W. (2010). Super-resolution mapping for extraction of urban tree crown objects from VHR satellite images.
- Tolpekin, V. A., & Stein, A. (2009). Quantification of the Effects of Land-Cover-Class Spectral Separability on the Accuracy of Markov-Random-Field-Based Superresolution Mapping. *IEEE Transactions on geoscience and remote sensing*, 47(SEPTEMBER 2009).
- Tso, B., & Mather, M. (2009). Modeling context using Markov Random Fields. In: *Classification methods for remotely sensed data* (2 ed., pp. 255-281).
- Van Der Meer, F., & De Jong, S. M. (2000). Improving the results of spectral unmixing of Landsat Thematic Mapper imagery by enhancing the orthogonality of end-members. *International Journal of Remote Sensing*, 21(15), 2781 - 2797.
- Wang, Z., Hu, G., & Yao, S. (2007). Decomposition Mixed Pixel of Remote Sensing Image Based on Tray Neural Network Model. In L. Kang, Y. Liu & S. Zeng (Eds.), *Advances in Computation and Intelligence* (Vol. 4683, pp. 305-309): Springer Berlin / Heidelberg.
- Yang, J., Zhang, J., Li Haitao, Sun, Y., & Pu Pengxian. (2010). Pixel level fusion methods for remote sensing images: A current review. *ISPRS TC VII Symposium – 100 Years ISPRS, Vienna, Austria, July 5–7, 2010, IAPRS XXXVIII(7B)*, 680-686.
- Zhang, K., Yan, J. H., & Chen, S. C. (2006). Automatic construction of building footprint's from airborne LIDAR data. [Article]. *IEEE Transactions on Geoscience and Remote Sensing*, 44(9), 2523-2533.
- Zhang, Y. (1999). Optimisation of building detection in satellite images by combining multispectral classification and texture filtering. *Isprs Journal of Photogrammetry and Remote Sensing*, 54(1), 50-60.
- URL-1 : Geospatial Data Analysis Corporation  
<http://www.gdacorp.com/satellite-image-processing/>- Access date: 08-09- 2010.
- URL-2: MAp of Aceh  
<http://baliwww.com/aceh/map.htm> - Accessed on 2011-01-07
- URL-3: Sub pixel mapping  
[http://www.vub.ac.be/spider/research\\_subpixelmapping.html](http://www.vub.ac.be/spider/research_subpixelmapping.html) -Accessed on 2011-02-11



## Appendix A

The photograph of the red roof building, blue roof buildings and white roof building



Red roof buildings



Blue roof buildings



White roof buildings

Figure A1: Photographs of the study area (Source: Bijker & Sanjaya, 2008)

# Appendix B

GCP Tool : (Input : msc\_070525043440\_04395\_07681041pp25\_1r.tif) (Reference : test27re.gcc)

Control Point Error: (X) 0.0208 (Y) 0.0200 (Total) 0.0289

Point #	Point ID	Color	X Input	Y Input	X Ref.	Y Ref.	Type	X Residual	Y Residual	RMS Error	Contrib	Match
1	GCP #1		85.906	-379.908	346.451	-1520.395	Control	0.003	0.002	0.004	0.142	
2	GCP #2		3676.933	-383.817	14708.125	-1534.125	Control	0.000	0.006	0.006	0.209	
3	GCP #3		3675.248	-3727.485	14700.875	-14911.875	Control	-0.005	0.029	0.030	1.023	
4	GCP #4		1051.107	-3721.467	4205.334	-14880.247	Control	0.004	0.031	0.031	1.085	
5	GCP #5		1233.517	-2534.554	4934.125	-10137.625	Control	-0.003	0.022	0.023	0.787	
6	GCP #6		1225.151	-2482.216	4900.625	-9928.375	Control	-0.013	0.027	0.029	1.016	
7	GCP #7		3545.544	-2456.437	14181.625	-9829.625	Control	0.007	-0.020	0.021	0.716	
8	GCP #8		3544.294	-2422.035	14177.125	-9692.625	Check					
9	GCP #9		3398.214	-2079.724	13432.125	-8322.125	Control	-0.003	0.003	0.004	0.127	
10	GCP #10		3367.120	-2126.665	13467.875	-8509.875	Control	0.028	0.018	0.033	1.144	
11	GCP #11		3241.462	-2098.982	12965.125	-8398.875	Control	0.020	0.009	0.022	0.749	
12	GCP #12		2400.874	-1274.024	9602.625	-5096.875	Control	-0.023	0.010	0.025	0.861	
13	GCP #13		2391.463	-1280.758	9564.375	-5125.625	Check					
14	GCP #14		2435.389	-1267.174	9740.875	-5069.625	Control	0.026	-0.025	0.036	1.244	
15	GCP #15		2927.387	-1041.259	11708.875	-4165.875	Control	-0.010	-0.025	0.027	0.943	
16	GCP #16		3563.793	-1048.459	14254.875	-4195.375	Control	-0.026	0.010	0.027	0.949	
17	GCP #17		3578.174	-1008.547	14312.625	-4035.625	Control	0.021	0.006	0.022	0.757	
18	GCP #18		3552.964	-1340.755	14212.375	-5366.125	Check					
19	GCP #19		3545.016	-1344.791	14181.125	-5384.125	Check					
20	GCP #20		3417.477	-670.462	13670.125	-2684.125	Check					
21	GCP #21		3366.296	-684.161	13466.625	-2738.625	Check					
22	GCP #22		3156.727	-1340.939	12622.125	-5360.375	Check					
23	GCP #23		3669.952	-1539.778	14679.375	-6162.375	Control	-0.033	-0.025	0.041	1.436	
24	GCP #24		2669.820	-1795.282	10678.375	-7182.875	Control	0.012	0.003	0.012	0.412	
25	GCP #25		2628.979	-1841.214	10514.875	-7366.625	Control	-0.020	-0.010	0.023	0.784	
26	GCP #26		2603.766	-1865.002	10414.125	-7461.625	Control	0.007	0.023	0.024	0.814	
27	GCP #27		2471.865	-1550.851	9886.625	-6204.625	Control	0.013	0.017	0.021	0.738	
28	GCP #28		2271.341	-1604.774	9084.375	-6421.375	Check					
29	GCP #29		2220.143	-1704.434	8879.125	-6819.625	Check					
30	GCP #30		2021.709	-2294.691	8085.875	-9179.625	Check					
31	GCP #31		2080.446	-1665.918	8319.375	-6666.375	Check					
32	GCP #32		1733.321	-1657.252	6934.125	-6629.875	Check					
33	GCP #33		1499.818	-660.169	5999.375	-2640.125	Control	0.003	-0.001	0.003	0.108	
34	GCP #34		1083.845	-2247.028	4333.875	-8998.875	Check					
35	GCP #35		1176.043	-2205.864	4704.251	-8823.696	Control	-0.008	-0.026	0.027	0.946	
36	GCP #36		1239.024	-2293.881	4956.125	-9175.625	Control	0.001	-0.021	0.021	0.715	
37	GCP #37		1198.267	-2324.708	4793.125	-9298.875	Control	-0.008	-0.026	0.028	0.962	
38	GCP #38		1228.521	-2368.834	4914.125	-9475.125	Control	-0.002	0.020	0.020	0.688	
39	GCP #39		1224.669	-2418.664	4898.625	-9674.375	Control	-0.029	0.011	0.031	1.060	
40	GCP #40		1404.527	-2420.697	5618.125	-9682.625	Control	0.050	0.015	0.052	1.811	
41	GCP #41		1287.948	-3177.501	5151.875	-12707.625	Control	-0.029	-0.034	0.045	1.566	
42	GCP #42		1295.202	-3131.691	5183.375	-12524.375	Check					
43	GCP #43		1273.081	-3450.467	5092.625	-13798.125	Control	-0.016	0.004	0.016	0.565	
44	GCP #44		1096.107	-3672.292	4385.375	-14684.125	Control	0.042	-0.027	0.050	1.735	
45	GCP #45		3257.457	-3639.948	13029.125	-14160.875	Control	-0.047	-0.004	0.047	1.638	
46	GCP #46		3634.566	-3675.347	14544.429	-14303.623	Check					
47	GCP #47		3606.401	-3493.742	14425.375	-13977.625	Control	0.012	-0.044	0.046	1.586	
48	GCP #48		3626.862	-3113.156	14505.037	-12454.694	Check					
49	GCP #49		3598.524	-2117.330	14393.625	-8473.125	Control	0.011	0.012	0.016	0.540	
50	GCP #50		3676.124	-1942.206	14705.375	-7771.125	Check					
51	GCP #51		3002.812	-1616.018	12009.590	-6465.389	Check					
52	GCP #52		2816.993	-2766.083	11268.125	-11065.625	Check					

Figure B1: The final result of co-registration of MS image with panchromatic image

GCP Tool : (Input : google.img) (Reference : referrenfor\_google.gcc)

Control Point Error: (X) 0.2203 (Y) 0.1277 (Total) 0.2546

Point #	Point ID	Color	X Input	Y Input	X Ref.	Y Ref.	Type	X Residual	Y Residual	RMS Errc	Contrib	Match
1	GCP #1		473.659	-669.683	4911.625	-9473.125	Control	0.102	-0.142	0.175	0.685	
2	GCP #2		1434.714	-900.315	5619.707	-9668.949	Control	-0.034	0.002	0.034	0.133	
3	GCP #3		713.918	-344.593	5096.377	-9192.569	Control	0.308	-0.061	0.314	1.232	
4	GCP #4		512.266	-323.982	4938.125	-9170.875	Control	0.098	0.129	0.162	0.638	
5	GCP #5		535.662	-330.110	4956.088	-9177.032	Control	-0.441	-0.158	0.468	1.839	
6	GCP #6		511.442	-492.364	4939.125	-9321.125	Control	0.115	0.263	0.287	1.129	
7	GCP #7		588.505	-465.055	4998.125	-9298.375	Control	0.056	-0.118	0.130	0.512	
8	GCP #8		789.120	-579.112	5150.300	-9399.119	Control	-0.162	0.185	0.246	0.966	
9	GCP #9		775.176	-743.004	5135.875	-9536.625	Control	-0.339	-0.149	0.370	1.454	
10	GCP #10		682.167	-962.363	5063.125	-9712.625	Control	0.085	0.021	0.087	0.343	
11	GCP #11		883.819	-867.665	5213.375	-9638.625	Control	0.310	-0.008	0.310	1.218	
12	GCP #12		457.675	-916.128	4900.338	-9674.671	Control	-0.215	0.070	0.226	0.888	
13	GCP #13		263.264	-679.381	4755.022	-9479.546	Control	0.116	-0.036	0.122	0.478	
14	GCP #14						Control					

Figure B2: The result of co-registration of Google earth image with panchromatic image

## Appendix C

### The training data set

Table C1: Mean vector of the each class in each band of MS image

Spectral band	Red roof buildings	Blue roof buildings	White roof buildings	vegetation	Shadow	Bare soil	Road
Band 1(Blue)	591.890	747.975	917.150	577.365	310.364	686.704	690.511
Band 2(Green)	478.912	504.185	855.760	482.382	310.364	639.379	624.211
Band 3(Red)	685.965	478.481	1033.345	430.952	310.364	863.2960	768.672
Band 4 (NIR)	423.991	419.642	657.650	729.918	310.364	532.3310	510.239

Table C2: Covariance matrix of the red roof building class

Band	Band 1	Band 2	Band 3	Band 4
Band 1	363.243	366.078	843.494	394.647
Band 2	366.078	502.653	970.116	522.286
Band 3	843.494	970.116	4401.206	1714.731
Band 4	394.647	522.286	1714.731	2669.366

Table C3: Covariance matrix of the blue roof building class

Band	Band 1	Band 2	Band 3	Band 4
Band 1	8699.974	1446.205	1279.525	6587.041
Band 2	1446.205	901.178	1582.360	1887.942
Band 3	1279.525	1582.360	3978.878	2645.825
Band 4	6587.041	1887.942	2645.825	8755.158

Table C4: Covariance matrix of the white roof building class

Band	Band 1	Band 2	Band 3	Band 4
Band 1	13846.410	14388.986	9063.581	15602.445
Band 2	14388.986	15838.163	10217.927	17488.137
Band 3	9063.581	10217.927	9204.549	10698.905
Band 4	15602.445	17488.137	10698.905	31079.013

Table C5: Covariance matrix of the vegetation class

Band	Band 1	Band 2	Band 3	Band 4
Band 1	72.438	53.589	142.720	8.003
Band 2	53.589	144.497	140.440	171.764
Band 3	142.720	140.440	542.443	-377.161
Band 4	8.003	171.764	-377.161	2322.240

Table C6: Covariance matrix of the shadow class

Band	Band 1	Band 2	Band 3	Band 4
Band 1	1458.093	0.000	0.000	0.000
Band 2	0.000	1458.093	0.0000	0.000
Band 3	0.000	0.000	1458.093	0.000
Band 4	0.000	0.000	0.000	1458.093

Table C7: Covariance matrix of bare soil class

Band	Band 1	Band 2	Band 3	Band 4
Band 1	249.112	287.271	683.965	84.169
Band 2	287.271	424.720	850.565	199.861
Band 3	683.965	850.565	2348.551	70.392
Band 4	84.169	199.861	70.3920	681.138

Table C8: Covariance matrix of road class

Band	Band 1	Band 2	Band 3	Band 4
Band 1	1080.296	1231.780	2277.370	-453.318
Band 2	1231.780	1664.033	2946.980	1.190
Band 3	2277.370	2946.980	5935.004	-351.391
Band 4	-453.318	1.190	-351.391	3418.328

Table C9: Mean and standard deviation of each class in panchromatic band

Statistics	Red roof buildings	Blue roof buildings	White roof buildings	Vegetation	shadow	Bare soil	Road
Mean	427.139	335.264	1050.595	549.909	310.364	552.814	533.650
SD	30.798	50.518	433.697	44.27	38.185	22.330	75.232

## Appendix D

Table D1: Statistics of kappa values for estimation of smoothing parameters ( $\lambda$  and  $\lambda_p$ )

$\lambda$	$\lambda_p$	Minimum kappa	Maximum Kappa	Mean Kappa	Standard deviation
0.6	0	0.467	0.488	0.482	0.007
	0.1	0.549	0.574	0.561	0.007
	0.2	0.542	0.565	0.551	0.007
	0.3	0.536	0.547	0.541	0.003
	0.4	0.519	0.531	0.524	0.004
	0.5	0.509	0.518	0.513	0.004
	0.6	0.494	0.505	0.500	0.004
	0.7	0.484	0.496	0.492	0.004
	0.8	0.477	0.490	0.484	0.004
0.7	0	0.440	0.474	0.458	0.011
	0.1	0.542	0.579	0.559	0.014
	0.2	0.555	0.587	0.574	0.011
	0.3	0.569	0.582	0.575	0.005
	0.4	0.565	0.576	0.570	0.004
	0.5	0.547	0.559	0.550	0.004
	0.6	0.521	0.542	0.535	0.008
	0.7	0.503	0.534	0.522	0.009
	0.8	0.499	0.522	0.509	0.006
0.8	0	0.433	0.474	0.445	0.012
	0.1	0.521	0.573	0.552	0.017
	0.2	0.543	0.600	0.578	0.019
	0.3	0.590	0.618	0.607	0.008
	0.4	0.578	0.626	0.599	0.014
	0.5	0.559	0.611	0.588	0.015
	0.6	0.573	0.602	0.587	0.010
	0.7	0.557	0.593	0.582	0.010
	0.8	0.543	0.581	0.559	0.013
	0.9	0.497	0.559	0.531	0.019
	1	0.507	0.541	0.518	0.013
0.9	0	0.320	0.434	0.367	0.032
	0.1	0.379	0.553	0.471	0.054
	0.2	0.480	0.612	0.559	0.039
	0.3	0.532	0.659	0.588	0.039
	0.4	0.516	0.650	0.586	0.044
	0.5	0.583	0.625	0.607	0.013
	0.6	0.610	0.647	0.630	0.015
	0.7	0.560	0.651	0.626	0.027
	0.8	0.606	0.687	0.642	0.021



## Appendix E

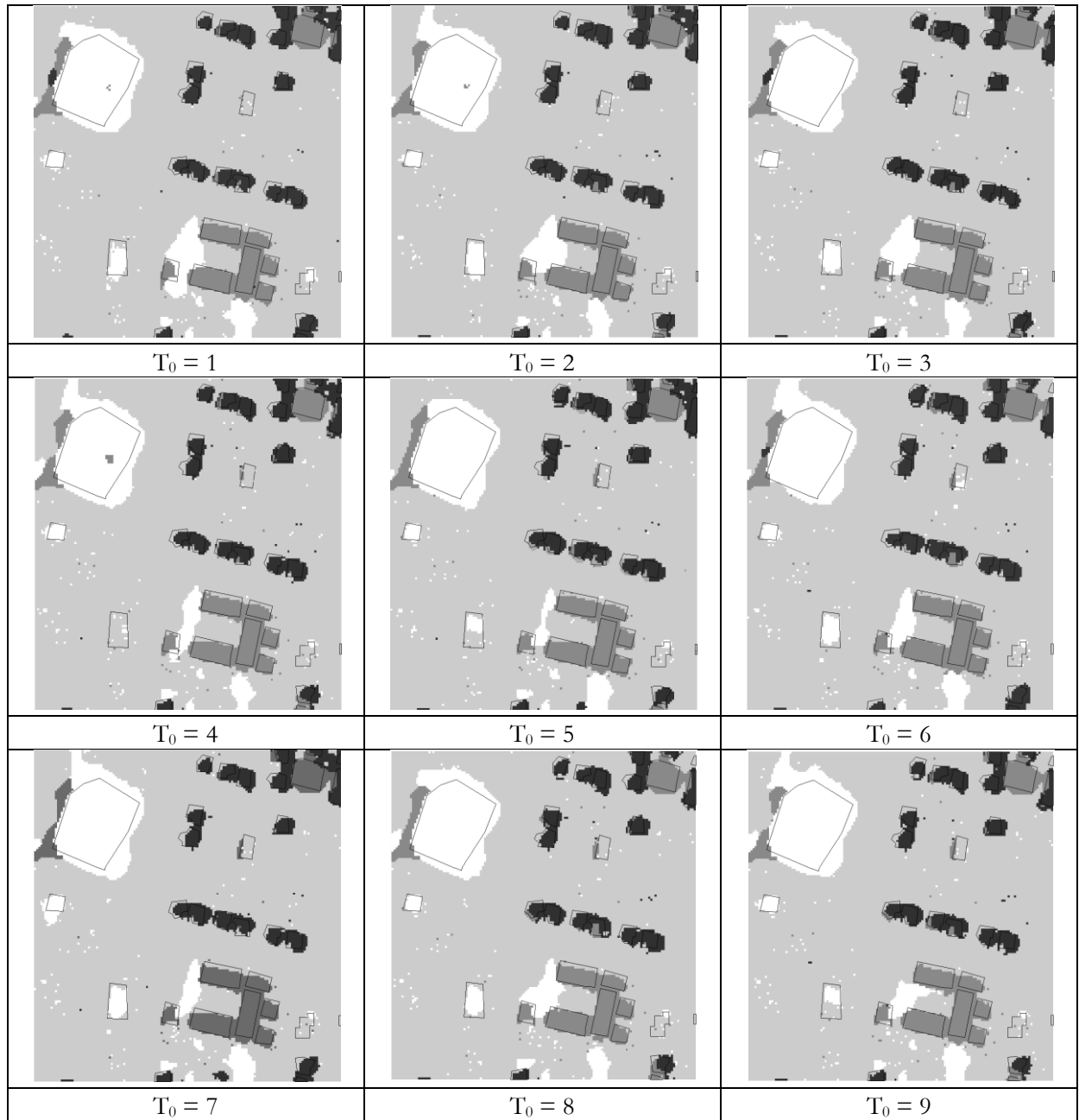


Figure E1: Detection of different type of buildings with different initial temperature

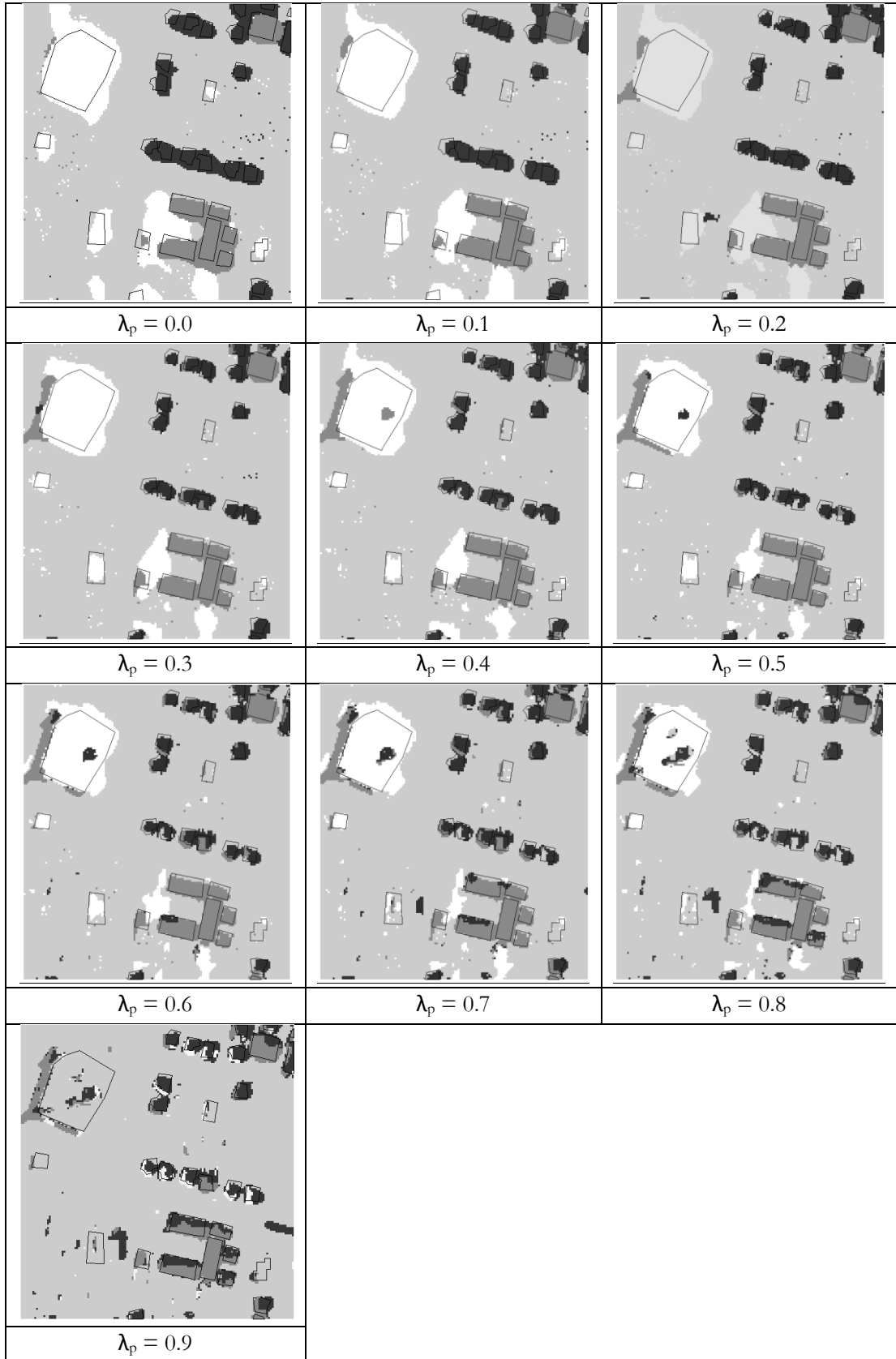


Figure E2: Detection of different type of buildings with  $\lambda = 0.8$  and different initial temperature

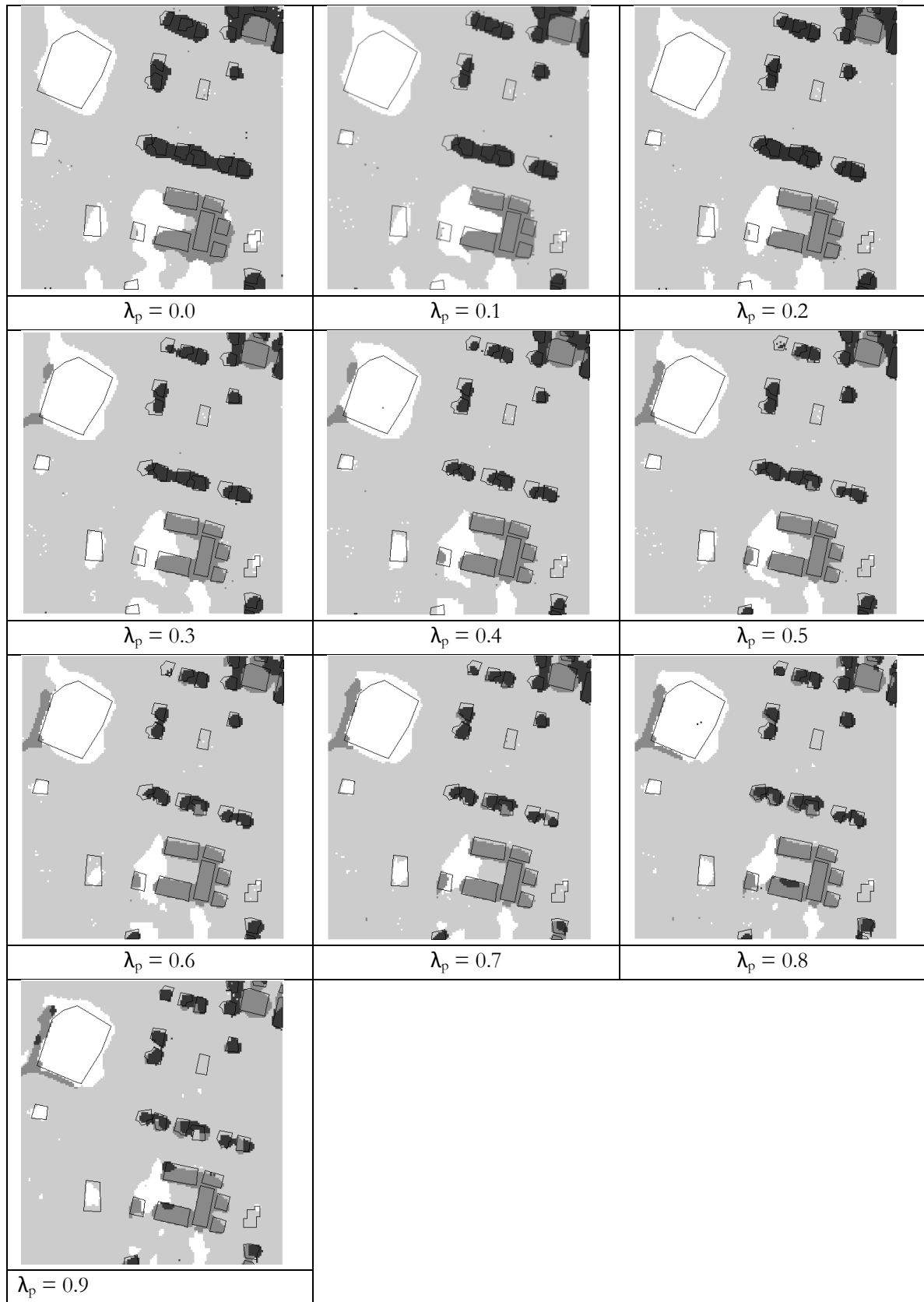


Figure E3: Detection of different type of buildings with  $\lambda = 0.9$  and different initial temperature

## Appendix F

The programme used for this research in R software is given bellow.

```

library(MASS)
library(mvtnorm)
library(pixmap)
library(scatterplot3d)

Root <- 'M:\\New_code\\'
#Root <- 'D:\\programming\\nanthamuni\\Ref_TS\\'

#####
# Read training set
#
#####

T0 <- 3.0
Tupd <- 0.9
Path_ts <- paste(Root, 'Training_set\\', sep='')
Inputfile <- paste(Path_ts, 'mean.txt', sep='')
temp <- read.table(Inputfile, skip = 1)
d <- dim(temp)
# File dimensions
# Number of bands
Nb <- d[1]
# Number of classes
Ncl <- d[2]
mu <- array(rep(0,Ncl*Nb),c(Ncl,Nb))
mut <- array(rep(0,Ncl*Nb),c(Nb,Ncl))
Cov <- array(rep(0,Ncl*Nb*Nb),c(Ncl,Nb,Nb))
Cinv <- array(rep(0,Ncl*Nb*Nb),c(Ncl,Nb,Nb))
mu_pan <- array(0,Ncl)
var_pan <- array(0,Ncl)
mu_pan_est <- array(0,Ncl)
var_pan_est <- array(0,Ncl)
mut <- data.matrix(temp)
mu <- t(mut)
for(k in 1:Ncl)
{
  Inputfile <- paste(Path_ts, 'Cov_',k, '.txt', sep='')
  temp <- read.table(Inputfile, skip = 0)
  Cov[k,,] <- as.matrix(temp)
  for(i in 1:(Nb-1))
  {
    for(j in (i+1):Nb)
      Cov[k,i,j] <- Cov[k,j,i]
  }
}
Inputfile <- paste(Path_ts, 'mean_pan.txt', sep='')
temp <- read.table(Inputfile, skip = 1)
mu_pan <- as.vector(temp[1,],mode="numeric")
var_pan <- as.vector(temp[2,],mode="numeric")
var_pan <- var_pan^2
for(k in 1:Ncl)
{

```

```

mu_pan_est[k] <- mean(mu[k,])
var_pan_est[k] <- sum(Cov[k,,]) / (Nb^2)
}
for(l in 1:Ncl) Cinv[l,] <- solve(Cov[l,])
ldet <- array(0,Ncl)
lpand <- array(0,Ncl)
for(k in 1:Ncl)
{
  lpand[k] <- log(var_pan[k])
  ldet[k] <- log(abs(det(Cov[k,,])))
}
logd0 <- min(ldet)
logpan0 <- min(lpand)
Div <- array(rep(0,Ncl^2),c(Ncl,Ncl))
TD <- array(rep(0,Ncl^2),c(Ncl,Ncl))
Div_pan <- array(rep(0,Ncl^2),c(Ncl,Ncl))
TD_pan <- array(rep(0,Ncl^2),c(Ncl,Ncl))
I0 <- array(0,c(Nb,Nb))
diag(I0) <- 1
for(k in 1:Ncl)
for(l in 1:Ncl)
{
  if(k==l)
  {
    Div[k,l] <- 0
    TD[k,l] <- 0
    TD_pan[k,l] <- 0
  }
  else
  {
    Div[k,l] <- sum(diag((Cinv[k,,]%*%Cov[l,]+Cinv[l,]%*%Cov[k,]-2*I0))) + sum(diag(t(mu[k,]-
mu[l,])%*%(Cinv[k,,]+Cinv[l,])%*%(mu[k,]-mu[l,])))
    Div[k,l] <- Div[k,l] / 2
    TD[k,l] <- 2*(1-exp(-Div[k,l]/8))
    Div_pan[k,l] <- 0.5*((mu_pan[k]-mu_pan[l])^2)*(1/var_pan[k]+1/var_pan[l]) + 0.5*(var_pan[k]-
var_pan[l]) * (1/var_pan[l]-1/var_pan[k])
    TD_pan[k,l] <- 2*(1-exp(-Div_pan[k,l]/8))
  }
}
}

TD
TD_pan

#####
# End read training set
#####

#####
#
# Import images
#
#####

WithRef <- TRUE
Path_in <- paste(Root,'Input\\Subset1\\',sep='')

```

```

Inputfile <- paste(Path_in, 'subset1_pan.txt', sep='')
temp <- read.table(Inputfile, skip = 5)
d <- dim(temp)
# Fine resolution image dimensions (determined from dim of the panchromatic band)
M <- d[1]
N <- d[2]
x <- 1:M
y <- 1:N
# Scale factor
S <- 4
# Degraded image dimensions
Mdeg <- M/S
Ndeg <- N/S
# Here real window size is 2*WSize+1
WSize <- S+3
#WSize <- 1
# Number (maximal) of pixel neighbours
Nn <- (WSize*2+1)^2-1
xdeg <- 1:Mdeg
ydeg <- 1:Ndeg
F <- array(rep(0, M*N), c(M,N))
Dpan <- array(rep(0, M*N), c(M,N))
Ddeg <- array(rep(0, Mdeg*Ndeg*Nb), c(Mdeg,Ndeg,Nb))
Dpan <- as.matrix(temp)
image(x,y, Dpan, col=gray((0:255)/255), main = 'Panchromatic band', xlab="",ylab="")
Ref_hard <- array(0,c(Mdeg,Ndeg))
if(WithRef)
{
  Inputfile <- paste(Path_in, 'reference.txt', sep='')
  temp <- read.table(Inputfile, skip = 5)
  Ref <- as.matrix(temp)
  Ref[Ref==255] <- 2
  Nclref <- 2
  x11()
  image(x,y,Ref, main = "Reference image", col=terrain.colors(Nclref), xlab="",ylab="")
}
for(k in 1:Nb)
{
  Inputfile <- paste(Path_in, 'subset1_band',k,'.txt', sep='')
  temp <- read.table(Inputfile, skip = 5)
  Ddeg[,k] <- as.matrix(temp)
}
x11()
par(mfrow=c(2,2))
for(k in 1:Nb)
image(xdeg,ydeg, Ddeg[,k], col=gray((0:255)/255), main = paste('Band',k, sep=""), xlab="",ylab="")
Dr <- Ddeg[,1:3]
Dr[,1] <- (Ddeg[,4])
Dr[,2] <- (Ddeg[,3])
Dr[,3] <- (Ddeg[,2])
x11()
par(mai=c(0,0,0,0))
A <- pixmapRGB(Dr,nrow=Mdeg,ncol=Ndeg)
plot(A)

Test <- FALSE

```

```

if(Test)
{
  Dpdeg <- Ddeg[,1]
  Dmsdeg <- Ddeg[,1]
  Dmsdeg[,] <- 0
  for(i in 1:Mdeg)
  for(j in 1:Ndeg)
  Dpdeg[i,j] <- mean(Dpan[((i-1)*S+1):(i*S),((j-1)*S+1):(j*S)])
  for(k in 1:Nb)Dmsdeg[,]<-Dmsdeg[,] + Ddeg[,k]
  Dmsdeg <- Dmsdeg/Nb
  x11()
  par(mfrow=c(1,2))
  image(xdeg,ydeg, Dpdeg, col=gray((0:255)/255), main = 'Degraded pan', xlab="",ylab="")
  image(xdeg,ydeg, Dmsdeg, col=gray((0:255)/255), main = 'Degraded MS', xlab="",ylab="")
}
#####
#
# End Import images
#
#####

#####
#
# Maximum Likelihood classification of the panchromatic image Dpan (fine resolution)
#
#####

Upan <- function(i,j,cl){
  val <- 0.5 * ((Dpan[i,j]-mu_pan[cl])^2) / (var_pan[cl]) + 0.5*log(var_pan[cl])
  return(val)
}
Refpan <- array(0,c(M,N))
for(i in 1:M)
for(j in 1:N)
{
  cl_opt <- 1
  U_opt <- Upan(i,j,cl_opt)

  for(cl in 2:Ncl)
  {
    Ut <- Upan(i,j,cl)
    if(Ut < U_opt)
    {
      cl_opt <- cl
      U_opt <- Ut
    }
  }
  Refpan[i,j] <- cl_opt
}
x11()
par(mfrow=c(1,2))
image(x,y,Refpan, main = "MLC of pan band", col=terrain.colors(Ncl), xlab="",ylab="")
plot(c(1,10),c(1,10))
legend("right",c('Red building', 'Blue building', 'White building', 'Vegetation', 'Shadow', 'Bare soil','Road'),
fill=terrain.colors(Ncl),cex=1.2)
Confpan <- array(0,c(2,2))

```

```

F <- Refpan
for(i in 1:Nclref)
for(j in 1:Nclref)
{
  F1 <-F
  F1[F1<=3] <-1
  F1[F1!=1] <-2

  Confpan[i,j] <- sum((F1==i)&(Ref==j))
}
Confpan
s1<-0
for(i in 1:Nclref)
{
  s1 <- s1 + sum(Confpan[i,])*sum(Confpan[,i])
}
kappapan <- (M*N*sum(diag(Confpan)) - s1) / ((M*N)^2 - s1)
kappapan

#####
#
# End of MLC of D
#
#####

#####
#
# Maximum Likelihood classification of the QB MS image Ddeg (coarse resolution multispectral image)
#
#####
Uxl_deg <- function(i,j,cl){
  y0 <- Ddeg[i,j,]
  logdet <- 0.5 * log(abs(det(Cov[cl,,])))
  val <- 0.5 * mahalnobis(y0, mu[cl,], Cinv[cl,,], inverted=TRUE) + logdet
  return(val)
}
Hard_ml <- array(0,c(Mdeg,Ndeg))
for(i in 1:Mdeg)
for(j in 1:Ndeg)
{
  cl_opt <- 1
  U_opt <- Uxl_deg(i,j,cl_opt)
  for(cl in 2:Ncl)
  {
    Ut <- Uxl_deg(i,j,cl)
    if(Ut < U_opt)
    {
      cl_opt <- cl
      U_opt <- Ut
    }
  }
  Hard_ml[i,j] <- cl_opt
}
}
x11()
par(mfrow=c(1,2))
image(xdeg,ydeg,Hard_ml, main = "MLC of image y", col=terrain.colors(Ncl), xlab="",ylab="")

```

```

plot(c(1,10),c(1,10))
legend("right",c('Red Buildings','Blue Buildings','White Buildings','Vegetation','shadow','Bare
soil','Road'),fill=terrain.colors(Ncl),cex=1.2)
for(i in 1:Mdeg)
for(j in 1:Ndeg)
{
  F[(i-1)*S+(1:S),(j-1)*S+(1:S)] <- Hard_ml[i,j]
}
Ref_hard <- F
ConfML <- array(0,c(Nclref,Nclref))
for(i in 1:Nclref)
for(j in 1:Nclref)
{
  F1 <-F
  F1[F1<=3] <- 1
  F1[F1!=1] <- 2
  ConfML[i,j] <- sum((F1==i)&(Ref==j))
}
ConfML
s1<-0
for(i in 1:Nclref)
{
  s1 <- s1 + sum(ConfML[i,])*sum(ConfML[,i])
}
kappaML <- (M*N*sum(diag(ConfML)) - s1) / ((M*N)^2 - s1)
kappaML
x11()
image(x,y,F1, main = "MLC Recoded", col=terrain.colors(Nclref), xlab="",ylab="")

#*****
#*****

#*****
#*****
#
#   Generate neighbourhood list
#
#*****
#*****

Neigh_Coord <- array(rep(0, M*N*4), c(M, N, 4))
Weight <- array(0, c(2*WSize+1, 2*WSize+1))
# Function assigning weights in the neighbourhood
# Function assigning weights in the neighbourhood
Fw <- function(a,b){
  val <- a^2 + b^2
  val <- 1 / val
  val <- val^(0.5)
#   val<-1
  if(a^2+b^2==0) val<-0
  return(val)
}
for(k in 1:(2*WSize+1))
for(l in 1:(2*WSize+1))
  Weight[k, l] <- Fw(k-(WSize+1),l-(WSize+1))
Weight <- Weight/ sum(Weight)

```

```

for(i in 1:M)
for(j in 1:N)
{
  imin <- i - WSize
  imax <- i + WSize
  jmin <- j - WSize
  jmax <- j + WSize
  if(imin<1) imin <-1
  if(imax>M) imax <-M
  if(jmin<1) jmin <-1
  if(jmax>N) jmax <-N
  Neigh_Coord[i, j, ] <- c(imin,imax,jmin,jmax)
}

#####
#####

#####
#
# Loop for lambda starts here
#
#####

lambda <- 0.8
#lamarr <- c(0.1*(0:10))
#lamarr <- 0.5

for(plam in 1:length(lamarr))
{
lam_pan <-0.3
#lam_pan <- lamarr[plam]
INSRM <- array(rep(0, M*N), c(M,N))
frac <- array(rep(0, Mdeg*Ndeg*Ncl), c(Mdeg,Ndeg,Ncl))
frac_in <- array(rep(0, Mdeg*Ndeg*Ncl), c(Mdeg,Ndeg,Ncl))
frac_ref <- array(rep(0, Mdeg*Ndeg*Ncl), c(Mdeg,Ndeg,Ncl))
Experimentname <-
paste("T0=',T0,'\ Tupd=',Tupd,'\ WS=',WSize,'\ Lambda=',lambda,'\ lam_pan',lam_pan,'\ '\,sep=")
Path_out <- paste(Root,'Output'\ Subset1,'\ '\, Experimentname,sep=")
dir.create(Path_out, recursive = TRUE)
Outputfile<- 'Stat_'

#####
#
# Identify pure vs mixed pixels in the Reference image
#
#####

if(WithRef)
{
  for(i in 1:Mdeg)
  for(j in 1:Ndeg)
  {
    val <- array(0,Ncl)
    for(ki in 1:S)
    for(kj in 1:S)
    {

```

```

        cln <- Ref[(i-1)*S+ki,(j-1)*S+kj]
        val[cln] <- val[cln] + 1
    }
    val <- val / (S^2)
    frac_ref[i,j] <- val
}
# x11()
# par(mfrow=c(2,Ncl/2+1))
# for(l in 1:Ncl) image(xdeg, ydeg, frac_ref[,l], main = "Class proportion",
col=gray((0:255)/255),xlab="",ylab="")
}
#
# End of pixel purity module

####
#### Linear spectral unmixing with SVD
####

epsilon <- 1e-6
N0 <- min(Ncl,Nb)
u0 <- array(0,c(Ncl,Ncl))
v0 <- array(0,c(Nb,Nb))
d0 <- array(0,c(N0,N0))
musvd<-svd(mu)
u0 <- musvd$u
v0 <- musvd$v
d1 <- musvd$d
for(i in 1:N0)
{
    if(d1[i]>=epsilon) d0[i,i]<-1.0/d1[i]
}
d0<-t(d0)
d0 <- t(v0%*%d0%*%t(u0))
for(i in 1:Mdeg)
for(j in 1:Ndeg)
{
    frac[i,j] <- d0%*%Ddeg[i,j]
}

#residual
res<-array(0,c(Mdeg,Ndeg,Nb))
sumfr<-array(0,c(Mdeg,Ndeg))
for(i in 1:Mdeg)
for(j in 1:Ndeg)
{
    res[i,j] <-frac[i,j]%*%mu-Ddeg[i,j]
    sumfr[i,j]<-sum(frac[i,j])
}

frac_in <- frac
x11()
par(mfrow=c(2,3))
for(l in 1:Ncl) image(xdeg, ydeg, frac[,l], main = "Class proportion",
col=gray((0:255)/255),xlab="",ylab="")
frac[frac<0] <- 0
frac[frac>1] <- 1

```

```

####
#### End of Unmixing module
####

# Number of independent runs with fixed parameters
Nr_rep <- 1
rep_start <- 1
for(zrep in rep_start:Nr_rep)
{
#zrep<-1

#####
#
# Initial SRM generation
#
#####

#for(i in 1:Mdeg)
#for(j in 1:Ndeg)
#{
#   Nsr <- array(rep(0,Ncl),Ncl)
#   count <- array(rep(0,Ncl),Ncl)
#   S1 <- sum(frac[i,j,])
#   Nsr <- round(frac[i,j,] * (S^2) / S1)
#   Nsr[Nsr<0] <- 0
#   Nsr[Nsr>(S^2)] <- S^2
#   F[((i-1)*S+1):(i*S),((j-1)*S+1):(j*S)] <- Ncl
#   for(l in 1:(Ncl-1))
#   {
#       while((count[l]<Nsr[l])&(sum(count)<S^2))
#       {
#           rown <- round(0.5+runif(1, min=0, max=S))
#           coln <- round(0.5+runif(1, min=0, max=S))
#
#           if(F[(i-1)*S+rown, (j-1)*S+coln]==Ncl)
#           {
#               F[(i-1)*S+rown, (j-1)*S+coln] <- 1
#               count[l] <- count[l] + 1
#           }
#       }
#   }
# }
# }
#}

#INSRM <- Refpan
#INSRM[,] <- round(0.5 + runif(M*N, min=0, max=Ncl))
#INSRM <- F
INSRM <- Ref_hard
x11()
image(x, y, INSIRM, main = "Initial SRM",col=terrain.colors(Ncl),xlab="",ylab="")
write.table(INSIRM, file =
paste(Path_out,'InitialSRM', '_trial=',zrep,'.txt',sep=""),append=FALSE,quote=TRUE,sep =
",eol="\n",na="NA",dec=".",row.names=FALSE,col.names=FALSE,qmethod=c("escape","double"))

```

```
#####
#
# End of Initial SRM generation module
#
#####

#####
#
# MRF and MCMC functions definition module
#
#####

I <- function(x,y){
  val <- 1
  if(x==y) val <- 0
  return(val)
}

xS <- function(x){
  val <- ceiling(x/S)
  return(val)
}

Frac_update <- function(i,j)
{
  val <- array(rep(0,Ncl),Ncl)

  for(ki in 1:S)
  for(kj in 1:S)
  {
    cln <- F[(i-1)*S+ki,(j-1)*S+kj]
    val[cln] <- val[cln] + 1
  }

  val <- val / (S^2)
  return(val)
}

Uprior <- function(i,j) {
  W1 <- Weight[(Neigh_Coord[i,j,1]-i+1+WSize):(Neigh_Coord[i,j,2]-i+1+WSize),(Neigh_Coord[i,j,3]-
j+1+WSize):(Neigh_Coord[i,j,4]-j+1+WSize)]
  F2 <- F[(Neigh_Coord[i,j,1]):(Neigh_Coord[i,j,2]),(Neigh_Coord[i,j,3]):(Neigh_Coord[i,j,4])]
  l <- F[i,j]

  F0 <- F2 - 1
  F0[F0!=0] <- 1
  val <- sum(W1 * F0)
  return(val)
}

Ulikelihood <- function(i,j) {
  i1 <- ceiling(i/S)
  j1 <- ceiling(j/S)
  y0 <- Ddeg[i1,j1]
  mm <- array(rep(0, Nb), Nb)
  Cm <- array(rep(0, Nb*Nb), c(Nb,Nb))

```

```

# Update class fractions in the coarse pixel y
F0 <- F[(S*(i1-1)+1):(i1*S),(S*(j1-1)+1):(j1*S)]

frac1 <- array(0,Ncl)
# mixing pixels
for(l in 1:Ncl)
{
  frac1[l]<-sum(F0==l)/(S^2)
#   mm <- mm + mu[l]*frac1[l]
  Cm <- Cm + Cov[l,]*frac1[l]
}

mm <- frac1%*%mu

Cinv <- solve(Cm)
logdet <- 0.5 * (log(abs(det(Cm))) - logd0)

val <- 0.5 * mahalanobis(y0, mm, Cinv, inverted=TRUE) + logdet

# Include the panchromatic term here!

l <- F[i,j]

val <- (1-lam_pan)*val + lam_pan*(0.5*(((Dpan[i,j]-mu_pan[l])^2)/(var_pan[l]) + log(var_pan[l])-
logpan0))

  return(val)
}

U <- function(i,j) {
  val <- lambda * Uprior(i,j) + (1.0-lambda) * Ulikelihood(i,j)
  return(val)
}
TotalEnergy<-function(F)
{
  val <- 0

  for(i in 1:M)
  for(j in 1:N)
    val <- val + U(i,j)

  return(val/(M*N))
}

#####
#
# End of the module MRF and MCMC functions definition
#
#####

```

```
#####
#
# MCMC Energy optimisation
#
#####

# Test:
#F <- Finit

Niter <- 10000

# Ntries<-1
# Converg <- array(rep(0,Ntries*Niter),c(Niter,Ntries))
min_acc_thr <- 0.1*10^(-2)
# min_acc_thr <- 0
MSE <- array(rep(0, Niter), 1)
Etotal <- array(rep(0, Niter), 1)
Thist <- array(rep(0, Niter), 1)
T<-T0

# F <- Ref
# F <- matrix(round(runif(M*N, min=1, max=Ncl)), nrow = M, ncol = N)

F <- INSRM

stop_crit <- 0

if(WithRef)
{
# Confusion matrix
Conf <- array(0,c(Nclref,Nclref))

F1 <-F
F1[F1<=3] <-1
F1[F1!=1] <-2

for(i in 1:Nclref)
for(j in 1:Nclref)
{
Conf[i,j] <- sum((F1==i)&(Ref==j))
}
Conf
s1<-0
for(i in 1:Nclref)
{
s1 <- s1 + sum(Conf[i,])*sum(Conf[,i])
}
kappaI <- (M*N*sum(diag(Conf)) - s1) / ((M*N)^2 - s1)
kappaI
# End of Confusion matrix module
}

#x11()
#par(mfrow=c(1,1))
```

```

for(iter in 1:Niter)
{
  upd_count <- 0

  for(i in 1:M)
  for(j in 1:N)
  {

    F_update <- round(0.5 + runif(1, min=0, max=Ncl))

    Ft <- F[i,j]

    if(F_update!=Ft)
    {
      u1 <- U(i,j)
      F[i,j] <- F_update

      u2 <- U(i,j)

      u1 = u2-u1

      if(T!=0)
      {
        u1 = exp(-u1/T)

        xi = runif(1, min=0, max=1)

        if(xi>u1)
        {
          F[i,j] <- Ft
        }
        else upd_count<-upd_count+1
      }
      else
      {
        if(u1>0)
        {
          F[i,j] <- Ft
        }
        else upd_count<-upd_count+1
      }
    }

  }

  # Converg[iter,l] <- upd_count / (M*N)
  # if(upd_count>=min_acc_thr*M*N) break

}

Thist[iter] <- T
F1 <-F
F1[F1<=3] <- 1
F1[F1!=1] <- 2

if(WithRef) MSE[iter] <-sum((Ref-F1)^2)/(M*N)
Etotal[iter] <- TotalEnergy(F)

```

```

#   if(upd_count<=0)
#   if(upd_count<=min_acc_thr*M*N)
#   {
#       stop_crit <- stop_crit +1
#   }
#   else stop_crit <- 0
#
#   if(stop_crit >=3) break
#
#   T <- T * Tupd
#   T <- T0/log(2+iter)
#   image(x,y, F, main = paste('Iter=',iter,sep=' '), col=terrain.colors(Ncl), xlab="",ylab="")
#
#   }
if(WithRef)
{
par(mfrow=c(2,3))

F1 <-F
F1[F1<=3] <- 1
F1[F1!=1] <- 2

image(x,y,INSRM, main = "Initial SRM", col=terrain.colors(Ncl), xlab="",ylab="")
image(x,y, F1, main = "Optimized SRM", col=terrain.colors(Nclref), xlab="",ylab="")
image(x,y,Ref, main = "Reference image", col=terrain.colors(Nclref), xlab="",ylab="")

plot(1:iter, Thist[1:iter], type = 'l', main = 'Temperature', xlab = 'Iteration', ylab = 'T')
plot(1:iter, MSE[1:iter], type = 'l', main = 'Error evolution', xlab = 'Iteration', ylab = 'MSE')
plot(1:iter, Etotal[1:iter], type = 'l', main = 'Energy minimisation', xlab = 'Iteration', ylab = 'Etotal')

x11()
par(mfrow=c(1,2))
image(x,y,F, main = "SRM (not recoded)", col=terrain.colors(Ncl), xlab="",ylab="")

plot(c(1,10),c(1,10))
legend("right",c("Red Buildings",'Blue Buildings','White
Buildings','Vegetation','shadow','Other'),fill=terrain.colors(Ncl),cex=1.2)

}else
{
# par(mfrow=c(2,2))
# image(x,y,INSRM, main = "Initial SRM", col=terrain.colors(Ncl), xlab="",ylab="")
# image(x,y, F, main = "Optimized SRM", col=terrain.colors(Ncl), xlab="",ylab="")

# plot(1:iter, Thist[1:iter], type = 'l', main = 'Temperature', xlab = 'Iteration', ylab = 'T')
# plot(1:iter, Etotal[1:iter], type = 'l', main = 'Energy minimisation', xlab = 'Iteration', ylab = 'Etotal')
# }

if(WithRef)
{
# Confusion matrix
Conf <- array(0,c(Nclref,Nclref))

for(i in 1:Nclref)

```

```

for(j in 1:Nclref)
{
  Conf[i,j] <- sum((F1==i)&(Ref==j))
}
Conf
s1<-0
for(i in 1:Nclref)
{
  s1 <- s1 + sum(Conf[i,])*sum(Conf[,i])
}
kappa <- (M*N*sum(diag(Conf)) - s1) / ((M*N)^2 - s1)
kappa

Etotal[iter]

# End of Confusion matrix module
}

c(iter, Etotal[iter], kappaI, kappa)

if(WithRef)
{
  write.table(c('iter',iter,'E',Etotal[iter],'kappa_I',kappaI,'kappa',kappa), file =
paste(Path_out,Outputfile,'_trial=',zrep,'.txt',sep=''),append=FALSE,quote=FALSE,sep = "
",eol="\n",na="NA",dec=".",row.names=FALSE,col.names=FALSE,qmethod=c("escape","double"))
  write.table(F, file =
paste(Path_out,'ResultSRM','_trial=',zrep,'.txt',sep=''),append=FALSE,quote=TRUE,sep = "
",eol="\n",na="NA",dec=".",row.names=FALSE,col.names=FALSE,qmethod=c("escape","double"))
  write.table(F1, file =
paste(Path_out,'ResultSRM_recoded','_trial=',zrep,'.txt',sep=''),append=FALSE,quote=TRUE,sep = "
",eol="\n",na="NA",dec=".",row.names=FALSE,col.names=FALSE,qmethod=c("escape","double"))
}

#####
#
# End of fractions module
#
#####

#####
#
# End of MCMC Energy optimisation
#
#####

# Close loop for zrep - number of trial
}

# close loop for lambda (panchromatic)
}

```